Single-molecule junctions – polarization effects and electronic structure

Ph.D Thesis
Nano-Science Center, Niels Bohr Institute
University of Copenhagen

Kristen Kaasbjerg
October 2009

Preface

This thesis is submitted in candidacy for the Ph.D. degree from University of Copenhagen (KU). It presents work carried out at the Nano-Science Center, Niels Bohr Institute at KU from July 2005 to October 2009 under supervision of Associate Professor Kurt Stokbro and Associate Professor Karsten Flensberg.

In the first year of my PhD studies Kurt was my principal supervisor. During this time I worked closely together with people in the company Atomistix (now QuantumWise) of which Kurt was co-founder. In August 2006 Kurt decided to leave for California where he was going to work for Atomistix local branch. With Kurt leaving I was fortunate to have Karsten taking over the supervision of my project. During the final year I carried out my PhD studies parallel to a full-time position at the Danish Maritime Safety Administration.

I would like to thank both Kurt and Karsten for their support and numerous inspiring discussions during the past years. Working with them has been a pleasure and I have benefited much from their individual skills. This has provided me with a broad knowledge on advanced numerical methods and a good physical insight.

Part of the work presented here was carried out in collaboration with Kristian S. Thygesen from Center for Atomic-scale Materials Design (CAMd) at the Technical University of Denmark. I am thankful to him for his assistance and his never failing enthusiasm.

Also thanks to the people in the theory group at the Nano-Science Center. I have enjoyed much working with them and will miss the nice atmosphere and exciting subjects discussed at the weekly group meetings. In particular, I would like to thank Hector Mera and Stephan Weiss for their useful help during the last phase of writing this thesis. Last but not least, I wish to thank my girl friend and daughter for their support and understanding. I am looking forward to share some more time with them in the future.

Kristen Kaasbjerg
Copenhagen, October, 2009

Abstract

This thesis addresses the electronic structure of single-molecule nanojunctions. Over the past decade the experimental field of single-molecule electronics has progressed tremendously. This has led to the realization of the single-molecule version of the field effect transistor. Due to a weak coupling between the molecule and the metal electrodes, these single-molecule transistor function similarly to single-electron transistors. The theoretical understanding of single-molecule junctions is, however, far from complete. Due to their small size, Coulomb interactions between the charge carriers on the molecule and polarization charges in the neighboring junction environment plays an important role for their fundamental properties.

A theoretical framework taking into account this effect is developed. It is based on an continuum electrostatic description of the junction combined with a quantum mechanical description of the molecule. The main result is an effective Hamiltonian for the molecule in which the junction is represented by its electrostatic potential. Hence, the solution to Poisson's equation for a given junction geometry is an important part of this approach. The framework is readily integrated into existing implementations of standard electronic structure methods.

In the present work a semi-empirical implementation of the approach has been applied to study polarization effects in a realistic single-molecule transistor. The Coulomb interaction between the molecule and the environment is demonstrated to alter the molecular electronic structure significantly. This is in agreement with experimental observations on single-molecule transistors. Furthermore, some general properties related to the electrostatic potential in single-molecule junctions are addressed.

Similar polarization effects can be expected to play a role for the electronic structure of metal-molecule interfaces where the molecule is chemically bonded to the surface. Theoretical descriptions of such interfaces are however complicated by the bonding between the surface and the molecule. A many-body description which treats the molecule and the surface on equal footing is one possible approach. The Green's function based GW method

belongs to this type of methods. Recent theoretical first-principles studies of molecules on surfaces have demonstrated that GW gives a qualitative correct description of the molecular levels when physisorbed on metallic and dielectric surfaces. It is therefore important to know how well GW describes the electronic structure of isolated molecules. A benchmark study comparing GW with exact results for semi-empirical model descriptions of molecules is here given. It shows that GW gives a consistent and good description of molecular levels. In conjunction with the fact that surface polarization effects are included in GW, this makes the GW method well suited for the study of metal-molecule interfaces.

Resumé

Denne afhandling omhandler elektron strukturen af nanoskala kontakter bestående af enkelte molekyler placeret mellem metalliske elektroder. Gennem det sidste årti er der sket et stort fremskridt indenfor eksperimentelt en-molekyle elektronik. Det har resulteret i realiseringen af en-molekyle versionen af felt-effekt transistoren som er den fundamentale komponent i en stor del af moderne forbrugerelektronik. På grund af en svag kemisk binding mellem molekylet og metal-elektroderne fungerer disse en-molekyle transistorer som en-elektron transistoren. Det vil sige at strømmen gennem en dem er karakteriseret ved at elektronerne passerer enkeltvis fra den ene elektrode til den anden via molekylet. Denne sekventielle transport mekanisme, som betegnes Coulomb blokade, er en konsekvens af den frastødende Coulomb vekselvirkning mellem elektronerne. Derudover spiller molekylets frihedsgrader også en vigtig rolle. For eksempel har adskillige eksperimenter demonstreret at molekylets vibrationelle tilstande påvirker elektron transporten mellem elektroderne. Den teoretiske forståelse af en-molekyle transistorer er dog stadig langtfra komplet. Ud over molekylets frihedsgrader spiller polarisering i selve nanokontakten også en vigtig rolle. På grund af kontaktens lille størrelse er Coulomb vekselvirkningen mellem de elektroniske ladningsbærerne og den polarisationsladning de inducerer i kontakten signifikant. Konsekvensen af denne vekselvirkning vil blive belyst i denne afhandling.

Til dette formål præsenteres en teoretisk metode til beskrivelse af en-molekyle kontakten. Den er baseret på en elektrostatisk kontinuum beskrivelse af kontakt delene, dvs elektroderne og dielektrikaet der separerer molekylet fra gate elektroden, kombineret med en kvantemekanisk beskrivelse af molekylet. Denne tilgang resulterer i en effektiv Hamilton for molekylet hvori kontakt delene er repræsenteret ved det elektrostatiske potentiale. Løsningen af Poisson's ligning for det elektrostatiske potentiale er derfor en vigtig del af denne tilgang. I praktisk kan metoden relativt nemt integreres i eksisterende implementeringer af elektron struktur metoder.

Beregninger baseret på en realistisk en-molekyle transistor demonstrerer at polarisations effekter fra kontakten ændrer molekylets elektron struktur

betydeligt. Det er i overensstemmelse med eksperimentelle observationer på en-molekyle transistorer. Derudover studeres generelle egenskaber af en-molekyle transistorer som er relateret til det elektrostatiske potentiale i kontakten.

Tilsvarende polarisations effekter kan forventes at have indflydelse på elektron strukturen af metal-molekyle kontakter hvor molekylet er kemisk bundet til metal overfladen. Teoretiske beskrivelser af disse systemer kompliceres imidlertid af den kemiske binding mellem molekylet og overfladen. En atomar mange-partikel beskrivelse som behandler molekylet og overfladen på lige fod er en mulig tilgang. Den Green's funktion baserede GW metode hører til denne type. Teoretiske studier af enkelte molekyler på overflader har demonstreret at GW metoden giver en kvalitativ korrekt beskrivelse af de molekylære niveauer når molekylet er physisorberet på en metal overflade. Det er derfor relevant at vide hvor godt GW metoden beskriver elektron strukturen af isolerede molekyler.

Til dette formål præsenteres et benchmark studie der sammenligner GW med eksakte resultater for en semi-empirisk beskrivelse af en række konjugerede molekyler. Studiet viser at GW metoden giver en konsistent og god beskrivelse af de molekylære niveauer. Eftersom GW metoden giver en god beskrivelse af både polarisations effekter fra metal overflader og niveauerne i molekyler, kan den bidrage til en bedre forståelse af metal-molekyle kontakter.

List of included papers

Paper I

Strong polarization-induced reduction of addition energies in single-molecule nanojunctions

K. Kaasbjerg and K. Flensberg

Nano Letters, **8**, 3809 (2008)

Paper II

Fully selfconsistent GW calculations for semi-empirical models and comparison to exact diagonalization

K. Kaasbjerg and K. S. Thygesen

Submitted to Physical Review B

Table of contents

Chapter 1

Introduction

The fundamental unit behind the functionality of modern computers is the MOSFET (metal-oxide-semiconductor field-effect transistor) illustrated in Fig. 1.1. In computer processors (CPUs) hundreds of millions of these transistors form the logic gates that perform the commands issued by a program. Since its invention at Bell Labs in 1960, the MOSFET has undergone an enormous miniaturization, which has resulted in smaller and faster computer processors. This development has followed the empirical Moore's law which states that the transistor density in integrated circuits doubles roughly every two years. The mainstream CPUs of today have a 45 nm channel length, corresponding to the distance between the source and drain electrodes. As the microelectronics industry is approaching fundamental physical limits the downscaling of conventional MOSFETs is unlikely to continue at unchanged pace [1].

The operational principle of the MOSFET is based on the so-called field effect which allows to control the density of mobile charge carriers in the channel between the source and drain electrodes by simple electrostatic means. The situation is illustrated for a positive gate voltage in Fig. 1.1(b). In this way the source-drain current can be modulated turning the MOSFET into a valve that can be switched on and off. In order to control the number of mobile charge carriers in the channel, a good capacitive coupling between the gate electrode and channel is required. However, due to the downscaling of the device dimensions, this becomes increasingly difficult due to screening effects in the nearby source and drain electrodes. One way to increase the capacitive coupling is to use a thinner gate dielectric which places the gate electrode closer to the channel. This, however, has the drawback that it leads to increasing leakage currents to the gate electrode resulting in power dissipation and heating. A lot of research is being invested in finding an alternative to SiO_2 as the gate dielectric material. High-κ dielectrics, i.e.

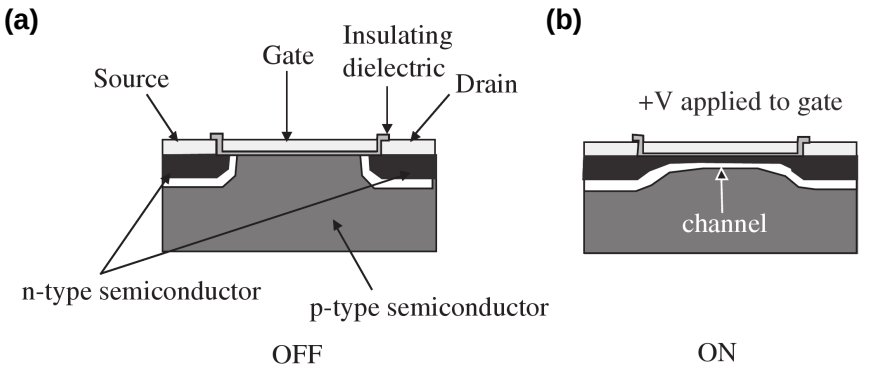

Figure 1.1: The MOSFET. (a) Cross sectional view of a MOSFET. The gate electrode is separated from the transistor channel between the source and drain electrodes by an insulating layer of dielectric material. (b) With a positive voltage applied to the gate electrode a conducting channel is formed between the source and drain electrodes. Taken from Ref. [4].

oxides with a higher dielectric constant than SiO_2 ($\varepsilon_r = 3.9$), allow for an increased capacitive coupling to the channel without the need of decreasing the thickness of the gate dielectric. However, the requirements for such a replacement are not few and research is still ongoing [2, 3].

While conventional silicon-based electronics has progressed, FETs based on other materials have gained increasing interest. These include examples such as organic FETs (OFETs) and organic thin film transistors (OTFT) in which an organic semiconductor is used as channel [5], self-assembled-monolayer FETs (SAMFETs) where a molecular monolayer constitute the channel [6], carbon nanotube FETs [7], and semiconductor nanowire FETs [8]. Apart from conventional FET applications, these types of transistors open up for interesting applications such as flexible displays and various sensing devices [9].

1.1 Single-molecule electronics

The idea of using single molecules as the functional unit in electronic devices originates from the theoretical work by Aviram and Ratner in 1974 [10]. Their idea was that a rectifying behavior of a molecular device could be tailored into the molecule with functional donor and acceptor groups. However, only within the past two decades have experimental techniques that allow for single-molecule studies been developed. These include different microscopy methods such as scanning tunneling microscopy (STM) and atomic force

microscopy (AFM) where the molecule is studied on a conducting substrate. More recently, the single-molecule version of the field effect transistor has been realized [11]. Such three-terminal junctions have the advantage that they allow to tune the molecular levels independently of an applied bias. This is in contrast to e.g. STM measurements which lacks potential control over the molecule. Here, the substrate and the tip function as source and drain electrodes.

The progress within the field of single-molecule experiments has led to many interesting observations. STM experiments probing a single organic molecule on a silicon surface has shown negative differential resistance (NDR) [12]. A theoretical explanation ascribes this effect to a bias induced shift of the current carrying molecular level which moves it inside the band-gap of the silicon substrate [13]. Other studies have demonstrated current-induced switching behavior due to molecular bistabilities [14, 15]. Impressive STM and AFM measurements on single pentacene molecules have demonstrated that images of the molecular orbitals [16] and the molecular atomic structure [17] can be obtained with very high resolution.

On the theoretical side a lot of work has been invested in understanding the experimental observations. Furthermore, single-molecule devices exploiting the molecular electronic structure have been suggested. These include exotic proposals as the quantum interference effect transistor (QuIET) [18] and the interference single-electron transistor (I-SET) [19]. The functionality of these devices is based on interference effects that arises from the symmetry of the molecule combined with the coupling to the metallic electrodes.

With focus on factors that determine the electronic structure of single-molecule nanojunctions, the scope of the present work is more general. Part of this work is motivated by experimental observations on three-terminal single-molecule transistors [20]. Since their functionality is similar to that of a single-electron transistor, a brief introduction to single-electron transistor theory is given in the following section. Subsequent sections present some introductory considerations on single-molecule transistors and an overview of relevant experimental results.

1.2 The single-electron transistor

The single-electron transistor (SET) schematically illustrated in Fig. 1.2(a) can be viewed as a FET where the channel has been replaced by a small conducting island with tunnel couplings to the source and drain electrodes. Due to the small size of the island the flow of electrons between the source and drain electrodes is dominated by the Coulomb repulsion between electrons on

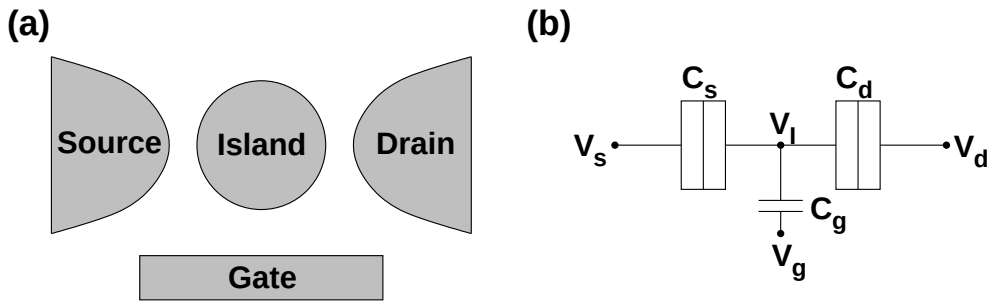

Figure 1.2: Schematic illustration of a single-electron transistor. (a) The island is connected to the source and drain electrodes with tunnel couplings. The energy of the island can be shifted with the gate electrode which couples capacitively to the island. (b) Capacitor description of the single-electron transistor. The potential of the island V_{I} is determined by the voltages applied to the electrodes and the charge Q on the island.

the island. For a given charge $Q = -eN$ on the island, the Coulomb charging energy associated with the addition of another electron is considerable. In order to have a current flowing extra energy must therefore be provided by the source-drain voltage. The resulting current is characterized by sequential tunneling events, where single electrons one by one traverse the island. This classical transport mechanism corresponds to the current to lowest order in the tunnel couplings. Every time an electron tunnels to and off the island the number of electrons N on the island fluctuates by one. Due to the blocking of the current at low biases, this phenomenon is referred to as Coulomb blockade.

Instead of increasing the source-drain voltage, the blockade can also be lifted by applying a voltage V_{g} to the gate electrode. This results in a series of peaks in the differential conductance as a function of the gate voltage V_{g}. This is illustrated in Fig. 1.3(a). The position of the peaks corresponds to gate voltages where a chemical potential μ of the island aligns with the Fermi energy of the source and drain electrodes. The situation is sketched in Fig. 1.3(b) for an arbitrary gate voltage. Consequently, at zero-bias conditions, only at these so-called charge degeneracy points will the island be able to change its charge and conduct a current between the source-drain electrodes. In between the degeneracy points current is blocked and the number of electrons N on the island remains fixed. The distance between consecutive peaks is termed the addition energy because it corresponds to the energy needed to add another electron to the island.

A common approximation is to characterize the island with a capacitance C. Within this approximation the Coulomb charging energy E_c becomes that

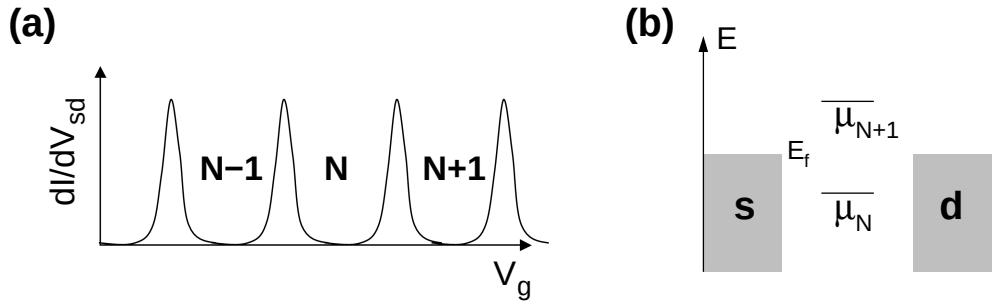

Figure 1.3: Differential conductance and level alignment of a single-electron transistor. (a) Differential conductance $dI/dV_{\rm sd}$ as a function of the gate voltage $V_{\rm g}$. Between the charge degeneracy points which are characterized by a peak in the differential conductance, the Coulomb blockade suppresses the current and leaves the island with a constant number of electrons. (b) Alignment between the Fermi energies of the electrodes and the chemical potentials of the island. The chemical potentials of the island can be shifted with a gate voltage.

of a classical capacitor

$$E_c = \frac{e^2}{2C}. \tag{1.1}$$

This is the essence of the constant-interaction model which will be introduced in more detail in the following section. Depending on the nature of the island quantum mechanical size quantization may become significant resulting in a level spacing Δ between the island states. This leads to the following expression for the addition energy

$$E_{\rm add} = \Delta + 2E_c. \tag{1.2}$$

Notice that only when Δ small compared to E_c will the charge degeneracy peaks be equally spaced as illustrated in Fig. 1.3.

In order to be in the Coulomb blockade regime a necessary condition is that the charging energy or the level spacing must be considerably higher than the temperature,

$$E_c, \Delta \gg k_{\rm B}T, \Gamma. \tag{1.3}$$

If this condition is not fulfilled thermal fluctuation will smear out the peaked structure in the differential conductance with the result that N becomes undefined for all values of the gate voltage. Also the tunnel couplings to the electrodes, which are here represented by a broadening Γ of the electronic levels, must be small compared to the charging energy and level spacing. In the opposite limit, i.e. $\Gamma \gg E_c, \Delta$, where quantum mechanical charge fluctuations dominate, the sequential tunneling picture no longer applies.

In this regime the electrons travel phase-coherently between the source and drain contacts. This is the situation in e.g. gate-defined quantum point contacts, where the conductance jumps in units of the conductance quantum $G_0 = e^2/h$ every time a new electron channel in the contact enters the bias window.

SETs have so far been realized in a wide range of different nanostructures. This includes metal nanoparticles, gate defined quantum dots in semiconductor structures, carbon nanotubes [21, 22], semiconducting nanowires [23, 24] and more recently single graphene sheets [25]. As the source-drain current is highly sensitive to overall changes in the island potential, SETs can be operated as ultra sensitive electrometers and have been used for e.g. real-time detection of individual electron tunneling events [26].

1.2.1 Constant-interaction model

The basic features in the IV-characteristics of different types of SETs can all be understood from the constant-interaction model. This model is analogous to the capacitance model illustrated in Fig. 1.2(b) where the island is coupled capacitively to the source, drain and gate electrodes with capacitances C_s, C_d and C_g. The potential V_I of the island is left floating. The integer charge on the island is represented by the sum of the charges Q_i on the individual capacitor electrodes, i.e. $-eN = \sum_i Q_i$. Each of the charges Q_i follows from the usual relation between charge and voltage on a capacitor, $Q_i = C_i(V_i - V_\mathrm{I})$, where V_i denotes the voltage applied to the i'th electrode. With N electrons on the island the energy of the system is given by the sum of the electrostatic energy and the single-particle energies [27]

$$E(N) = \frac{\left[e(N - N_0) - C_\mathrm{g}V_\mathrm{g}\right]^2}{2C} + \sum_{n=1}^{N} \varepsilon_n, \tag{1.4}$$

where N_0 is the number of electrons on the neutral island at $V_\mathrm{g} = 0$, $C = C_\mathrm{s}+C_\mathrm{d}+C_\mathrm{g}$ is the total capacitance and ε_n are the discrete energy levels of the island arising due to size quantization. The term $C_\mathrm{g}V_\mathrm{g}$ is a continuous variable that represents the gate induced charge on the island. The name constant-interaction model stems from the fact that the capacitances which account for the Coulomb repulsion on the island are considered to be independent of the applied voltages and the number of electrons N on the island. This is only a good approximation when the quantum states in which electrons are inserted have similar spatial distributions on the island and do not change with the applied voltages. As the present work will demonstrate, this is questionable when the island is a single molecule.

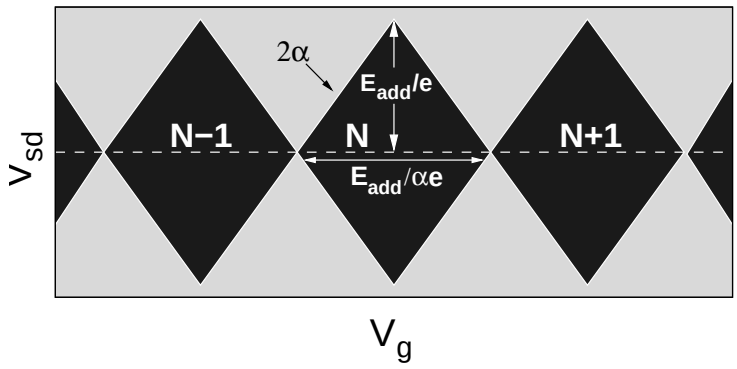

Figure 1.4: Charge stability diagram for a single-electron transistor showing schematically the current as a function of bias and gate voltage. Inside the black diamonds the current is blocked. The diamond edges corresponds to a situation where a chemical potential of the island passes through the Fermi energy of one of the electrodes. As indicated, values for the addition energy E_{add} and gate coupling α can be extracted from the diamonds.

At the charge degeneracy points discussed in the previous section the chemical potential of the island $\mu_N = E(N) - E(N-1)$ is aligned with the Fermi energies of the source and drain electrodes. With the energy given by Eq. (1.4) the chemical potential of the island can be written

$$\mu_N = (2N-1)E_c - e\alpha V_{\mathrm{g}} + \varepsilon_N \tag{1.5}$$

The change of the chemical potential with an applied gate voltage carries a prefactor $\alpha = C_{\mathrm{g}}/C$. This is the gate coupling which depends on the geometry of the sample. Due to the screening from the source and drain electrodes the gate coupling will always be less than unity, i.e. $\alpha < 1$. As the addition energy corresponds to the difference between adjacent chemical potentials,

$$E_{\mathrm{add}} = \mu_{N+1} - \mu_N, \tag{1.6}$$

the expression in Eq. (1.2) readily follows with $\Delta = \varepsilon_{N+1} - \varepsilon_N$. It is important to note that the distance between the charge degeneracy peaks on the gate voltage axis in Fig. 1.3 does not correspond to the actual addition energy. Due to the screening of the gate potential it is instead given by the addition energy scaled with the inverse of the gate coupling, $E_{\mathrm{add}}/(e\alpha)$.

As a function of both gate and source-drain voltage the regions in which the current is blocked forms a diamond-shaped structure as illustrated in Fig. 1.4. These so-called diamond plots, or charge stability diagrams, are very useful when studying the properties of a given device. As indicated in the figure, quantitative information about the gate coupling and addition energy

	GaAs quantum dot	10 nm metallic island	500 nm carbon nanotube	single molecule
Δ	~ 0.1 meV	1 meV	3 meV	> 0.1 eV
E_c	~ 1 meV	25 meV	3 meV	> 0.1 eV

Table 1.1: Typical level spacing and charging energies for different types of single-electron transistors [28].

can be inferred from these plots. When the bias is applied symmetrically to the source and drain electrodes, the slopes of the diamond edges are given by $\pm 2\alpha$. The addition energy can be obtained both from the width and the height of the diamonds. For the latter, this relies on the assumption that the applied source-drain voltage does not change the energy of the island – i.e. only the Fermi energies of the electrodes are shifted by the applied bias. In order for this to hold, the source and drain electrodes must have equal capacitive couplings to the island.

1.3 Single-molecule SETs

During the past decade there has been a significant progress in the experimental techniques for the fabrication of three-terminal single-molecule devices. This has allowed for the realization of the molecular version of the single-electron transistor. A major difference between single-molecule SETs and conventional SETs based on gate defined quantum dots in semiconductors structures and metallic nanoparticles is the size of the level spacing and charging energy. In Tab. 1.1 typical level spacing and charging energies for various SETs are summarized. Due to the relative small sizes of molecules both their levels spacings and charging energies of single-molecule SETS are considerably higher than those of other SET types. This, in principle, allows for room temperature operation since $E_c, \Delta > k_{\mathrm{B}}T \sim 26$ meV. At present, however, the stability of single-molecule SETs at non-cryogenic temperatures is still an open issue [4].

In the following sections a brief overview of fabrication techniques and experimental results for single-molecule SETs will be given. Moreover, some consideration relevant for the present work are presented. Further insight into the field is provided by the numerous review papers which have appeared over the recent years [4, 28, 29, 30, 31, 32].

1.3.1 Fabrication techniques

The experimental realization of a single-molecule SET relies on the fabrication of a three-terminal junction with a molecule bridging a nanoscale gap between the source and drain electrodes and a gate electrode placed close enough to the gap that it couples capacitively to the molecule. In Fig. 1.5 various techniques for this purpose are illustrated schematically. They mainly differ in the way the electrodes and the nanogap between them are created. In single-molecule SETs it is important that the gap is neither too long for the molecule to connect to both electrodes, or too small in which case a good gate coupling to the molecule becomes difficult to obtain. The three standard methods are (i) electromigration, (ii) angle evaporation, and (iii) mechanical break junction techniques.

In electromigrated nanogap fabrication the electrodes are constructed by passing a high current density through predefined metallic electrode structures [11, 33]. The scattering of the conduction electron results in a significant momentum transfer to the atomic lattice which eventually leads to a collapse of the metallic structure and the formation of a nanogap. One drawback of this method is that the geometry and size of the resulting nanogap is uncontrollable. In order to obtain gate control, the electrode structure is defined on top of a insulating oxide layer that separates the electrodes from a gate electrode. The resulting nanojunction is depicted in Fig. 1.5(a). Often, the high-κ dielectric Al_2O_3 is used as gate dielectric. This ensures a reasonable gate coupling to the molecule.

In angle evaporation illustrated in Fig. 1.5(b), the electrodes are fabricated by deposition of gold vapor on a $\sim$ 5 nm thick layer of insulating substrate through a shadow mask [20]. The deposition is performed at low temperatures ($\sim$ 4.2 K). The size of the generated nanogap can be adjusted by varying the deposition angle. By monitoring the source-drain conductance during the gold deposition high control of the created nanogap is obtained.

The fabrication of three-terminal nanojunctions using mechanical controllable break junctions has recently been reported [34]. So far, this technique has been restricted to two-terminal junctions (see e.g. [35]). The gap between the electrodes is generated by bending a metallic wire until it breaks into two pieces. The situation is illustrated in Fig. 1.5(c). The break junction technique has the major advantage that is allows for a very high control over the electrode spacing which can be tuned with picometer resolution. However, the large thickness ($\sim$ 40 nm) of the insulating gate dielectric required for this fabrication technique, results in a very low gate coupling as compared to the other techniques.

The introduction of the molecule into the fabricated nanogaps can be

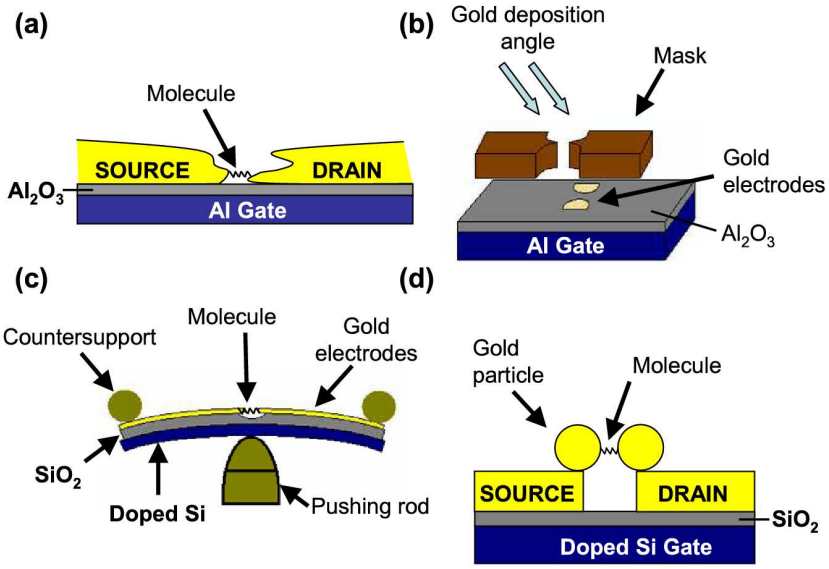

Figure 1.5: Illustration of different single-molecule junction fabrication techniques. (a) Electromigrated thin metal wire on top of a Al/Al_2O_3 gate electrode. (b) Angle evaporation technique to fabricate planar electrodes with nanometer separation on top of a Al/Al_2O_3 gate electrode. (c) Gated mechanical break junction. (d) The dimer contacting scheme in which the molecule is attached to gold particles. Figure taken from Ref. [31].

accomplished in different ways. One option is to subject the junction to a solution containing the molecule either prior to gap formation or afterward and then hope that a molecule will be caught in the gap between the electrodes. Alternatively, the molecules can be deposited on the electrodes by quench condensation [20]. By subsequent annealing the sample at low temperature (below 70 K), the molecules are allowed to diffuse. The presence of a molecule in the nanogap is detected by monitoring the source-drain conductance. When it changes markedly, the sample is cooled to cryogenic temperatures and IV-characteristics on the single molecule can be carried out.

In order to control the chemical coupling between the source and drain electrodes, the molecules are often prepared with chemical groups that either facilitates or prevents bonding to the metallic electrodes. It has recently been demonstrated that this approach allows to obtain a high control of the electrode-molecule coupling [36] which is essential for the device characteristics. With a large metal-molecule coupling Γ the Coulomb blockade requirements in Eq. (1.3) are not necessarily fulfilled. Indeed, it was demonstrated

that in this strong coupling regime the conductance showed no significant dependence on the gate voltage, and consequently, no Coulomb blockade characteristics were observed. On the other hand, when molecules are prepared with for example passivated thiol groups [20] or no chemical groups at all, only the weak van der Waals force binds the molecule to the electrodes. As a result, the device acquires SET functionality. This is the observed behavior of the majority of single-molecule junctions fabricated as described in the present section.

Another approach for controlling the electrode-molecule coupling is the dimer contacting scheme illustrated in Fig. 1.5(d) [37]. Here, the molecule is prepared with two gold particles which are connected to the molecule with thiol bonds. The gold particles allows to trap the dimer structure between the electrodes electrostatically. This approach has the inherent disadvantage that the gate coupling is low due to efficient screening in the gold particles.

From the present section it is clear that the techniques for fabrication of single-molecule SETs are highly statistical in nature. Therefore, no two devices will show exactly the same results and technological applications of single-molecule transistors should not be expected within the foreseeable future. Nevertheless, single-molecule SETs give the opportunity to study exciting physics and chemistry at the single-molecule level. Compared to single-molecule experiments using electrochemical gating at room temperature [38, 39, 40], the cryogenic solid-state environment of a single-molecule SET seems to be better suited for studying the fundamental role of the molecular degrees of freedoms on the charge transport through the molecule. For example, recent developments doing simultaneous conduction measurements and Raman spectroscopy on a single-molecule junction provides detailed information about the vibrational modes that play an active role in the electron transport [41, 42].

1.3.2 Addition energy

In single-molecule SETs the chemical potentials associated with the removal and addition of an electron from the neutral molecule are given by the molecular ionization potential (IP) and electron affinity (EA). They are defined by the total energy difference between the two charge states involved in the electron transfer, i.e. $\mathrm{IP} = E^{N-1} - E^N$ and $\mathrm{EA} = E^N - E^{N+1}$, where N denotes the number of electrons in the neutral molecule. The difference between the IP and EA defines the fundamental gap E_{gap} of a molecule

$$E_{\mathrm{gap}} = \mathrm{IP} - \mathrm{EA} = E^{N+1} + E^{N-1} - 2E^N. \tag{1.7}$$

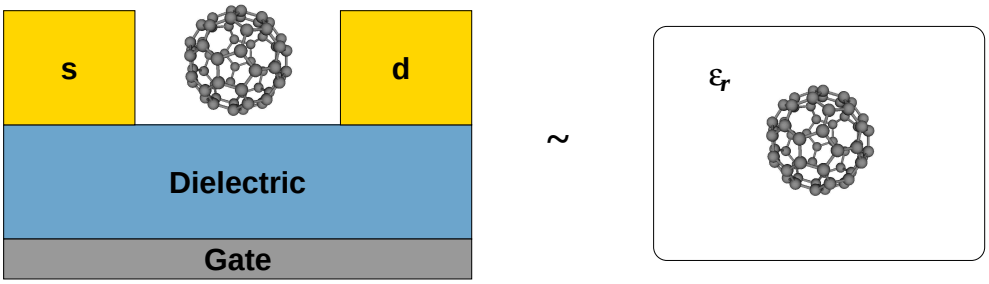

Figure 1.6: Schematic illustration of a nanojunction with a C_{60} molecule placed between the source and drain electrodes. In a simple approximation the effect of the junction environment can be described by a dielectric material with $\varepsilon_r \sim 10$ enclosing the molecule. In a capacitor description of the C_{60} molecule (see text) the capacitance is given by $C = 4\pi\epsilon_0 R\varepsilon_r$. Hence, the charging energy $E_c = e^2/2c$ of the molecule is strongly reduced in the junction.

In the SET framework the molecular gap corresponds to the addition energy in Eq. (1.6) of the neutral molecule. In a simplified single-particle description of the electronic structure of the molecule, the addition energy of a single-molecule SET takes a form equivalent to that of the constant interaction model in Eq. (1.2). The level spacing Δ is replaced by the HOMO-LUMO gap Δ_{HL} of the molecule, where HOMO and LUMO refers to the highest occupied and lowest unoccupied molecular orbital, respectively, and the charging energy E_c is the Coulomb energy it costs to remove (add) an electron to the HOMO (LUMO). Typical values for Δ_{HL} and E_c for isolated molecules are on the order of several electron-volts.

The following example consider the addition energy of the C_{60} molecule in terms of a simple capacitor model for the charging energy. The C_{60} molecule has an ionization potential and electron affinity of IP = 7.6 eV and EA = 2.65 eV [43], respectively. This results in a gap of $E_{\mathrm{gap}} = 4.95$. In a simplified description of the C_{60} molecule the charging energy can be approximated by that of a metal sphere with capacitance

$$C = 4\pi\epsilon_0 R, \tag{1.8}$$

where ϵ_0 is the vacuum permittivity and R is the radius of the sphere. Setting $R = 4$ Å, corresponding to the radius of the C_{60} molecule, the charging energy in Eq. (1.1) amounts to $E_c \sim 1.8$ eV, leaving 1.35 eV for the HOMO-LUMO gap. It should be noted that these consideration are only valid for the isolated molecule. When placed in a three-terminal nanojunction as illustrated in Fig. 1.6, the molecule is surrounded by metallic electrodes and gate dielectric which increases the capacitance and leads to a smaller charging

energy. A rough estimate of the effect can be obtained by approximating the junction environment with a dielectric material enclosing the C_{60} molecule as illustrated in Fig. 1.6. The presence of the dielectric increases the capacitance of the metallic sphere by a factor of ε_r, $C = 4\pi\epsilon_0 R\varepsilon_r$. Taking the average dielectric constant of the junction constituents to be $\varepsilon_r \sim 10$, the charging energy of the molecule is reduced to 180 meV. The addition energies of single-molecule SETs must therefore be expected to differ markedly from the molecular gap in gas phase.

1.3.3 The junction polaron

To give a clear physical picture of the underlying physics, the role of the junction environment is here discussed in further detail. In single-molecule SETs a current can run when for example the electron affinity aligns with the chemical potentials of the electrodes. In this situation an additional electron can tunnel onto the molecule resulting in a net negative charge. The electric field from the additional electron will tend to polarize the junction environment before it tunnels off the molecule again. Lending the quasi-particle picture from Fermi liquid theory, this results in charge carriers that are no longer bare electrons, but rather electrons dressed with a polarization cloud located in the junction environment. To complete quasi-particle analogy, the resulting quasi-particle could be called a junction polaron similar to the ordinary polaron (an electron surrounded by a cloud of phonons). For metals and dielectrics the main polarization effect, i.e. the polaron cloud, comes from electronic and ionic polarization. In order to have a well-defined junction polaron, the time τ_{mol} an electron spends on the molecule must be significantly larger than the time τ_{pol} it takes to polarize the junction environment. The latter is given by the plasmon ($\sim$ 10 eV) and phonon energy ($\sim$ 0.1 eV) corresponding to a polarization time of $10^{-16} - 10^{-14}$ s. The residence time on the molecule can be inferred from typical current values in single-molecule SETs which range from $I \sim$ pA $-$ nA. This results in a residence time of $\tau_{\mathrm{mol}} = I/e \sim 10^{-10}$ s. Hence, the criteria for well-defined junction polarons is met.

As demonstrated with the C_{60} example above, the effect of the junction polarization is to lower the energy of the charged $N \pm 1$ states of the molecule. This is a consequence of the attractive interaction between the electron and its oppositely charged polarization cloud. From Eq. (1.7) this is seen to result in a smaller gap compared to the case of the isolated molecule (gas phase). The corresponding shifts of the ionization potential and electron affinity will be referred to as the polarization energies P_+/P_- in the present work. The situation is summarized in Fig. 1.7 which shows the level alignment of a

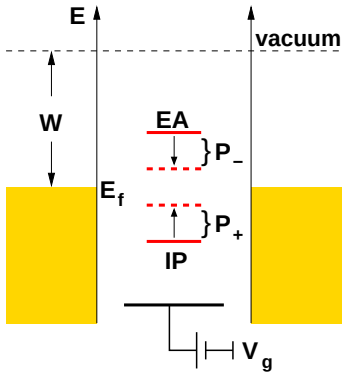

Figure 1.7: Energy level alignment in a single-molecule transistor. The polarization of the junction renormalizes the molecular ionization energy (IP) and electron affinity (EA) by the polarization energies $P_{+/-}$, respectively. The alignment between the Fermi energy of the source and drain electrodes and the molecular levels determine the threshold for electron transport through the junction.

single-molecule SET.

As the threshold for electron transport through the molecule is determined by the alignment between the molecular levels and the Fermi energy of the electrodes, the properties of single-molecule SETs are highly dependent on the size of the polarization energies. In order to obtain quantitative estimates for the polarization energies in single-molecule SETs, a quantum mechanical calculation of the total energies in Eq. (1.7) including the effect of junction polarization is required. A theoretical framework for this purpose is presented in Chap. 2.

Other polarizable environments

The effect of environmental polarization on molecular levels is well known from other fields. In electrochemistry charging processes of single molecules take place under potential control in ionic solutions at room temperature. Here, the analog of the polarization energies $P_{\pm}$ is the solvation free energy which describes the effect of solvent polarization [44]. The measured redox potentials of a given molecule are equivalent to the charge degeneracy points of a single-molecule SET. However, due to the different environmental situation, direct comparison between the two are not possible. For example, both response time and screening length are expected to differ markedly for the polarization of a ionic solvent and solid state environment. Fig. 1.8 illustrates the various contributions to the dielectric response and their characteristic frequencies. While solvent screening is characterized by orientational polar-

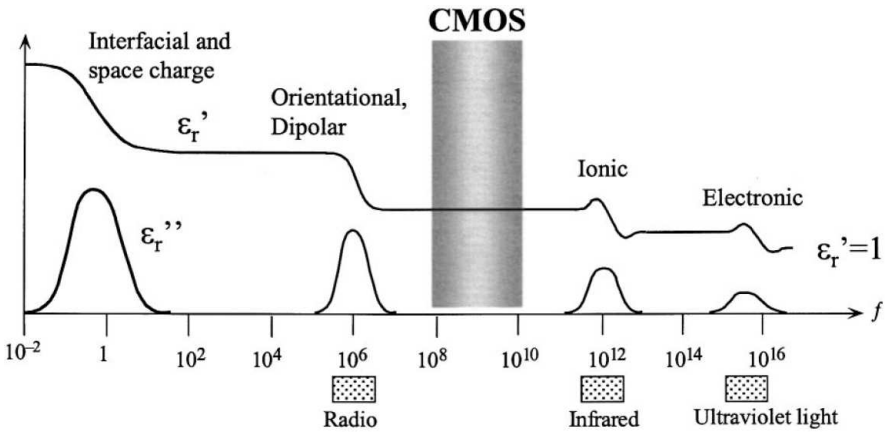

Figure 1.8: Characteristic frequencies of various polarization mechanisms showing their contribution to a generic dielectric function $\varepsilon_r = \varepsilon_r' + i\varepsilon_r''$. Taken from Ref. [2].

ization with relatively low frequencies, the electronic and ionic solid state screening have significantly higher frequencies. This implies that screening of dynamical electron transfer processes will in general be more efficient in solid state environments.

Polarization is also an important factor for electron transport in organic semiconductor crystals. Due to the weak van der Waals bonds between the molecular units the electronic structure of organic semiconductors is characterized by narrow bands (~ 0.1 eV). This renders a band description with delocalized Bloch states inappropriate. As a consequence, charge transport in these materials is better characterized by incoherent hopping between localized states on the molecular units. Due to the relatively long residence time on the individual molecular units (given by the bandwidth), the polaron picture also applies here. In this case, however, the polaron cloud is formed by electronic polarization of the neighboring molecular units. The polarization energies in organic semiconductors are on the order of $P_\pm \sim 1 - 2$ eV [45], leaving the band gap of the crystal significantly smaller than the gap of the isolated molecule.

1.3.4 Experimental overview

Due to the weak coupling between the electrodes and the molecule, single-molecule SETs allows to study electron transport through well-defined states of the molecule. For excited states this gives rise to additional features in the charge stability diagram apart from the Coulomb diamonds. From these features the nature and the energy of the excitations can be inferred.

Single-molecule SETs therefore provides a means of doing single-molecule spectroscopy in solid-state environments.

Over the past decade this has led to interesting observations of both the transport mechanism and molecular properties in single-molecule SETs. For example, in a pioneering work on the C_{60} molecule, it has been demonstrated that the tunneling of electrons can excite vibrational modes associated with the center-of-mass motion of the molecule [11]. In the charge stability diagram such excitations shows up as lines parallel to the diamond edges. In experiments on single-molecule magnets the magnetic properties of the molecules has been addressed [46, 47, 48]. From the charge stability diagram the different spin excitations of the molecule could be identified showing that the molecules remain magnetic in the solid-state junction environment. Moreover, the molecular spin degree of freedom was found to play an important role for the transport through the molecule.

A series of experiments have studied the properties of single-molecule SETs based on the conjugated oligo-phenylene vinylene molecule OPV5 [20, 49, 50]. The structure of the OPV5 molecule, which consists of alternating phenylene and vinylene groups, is illustrated in Fig. 1.9(a). The delocalized π-electron system of the molecule is intended to provide a pathway for electron transport between the electrodes. The experiments have provided detailed information about the molecular excitations in the junction. The following sections give a brief overview of the experimental results.

Access to several redox states

The experiment published in Ref. [20] was the first to report access to several charge states of a molecule in a single-molecule SET. The stability diagram in Fig. 1.9(b) show no less than eight well-defined charge states of the molecule. With such a large number of charge states one should be concerned that it really is a single molecule that has been trapped in the gap between the electrodes, and not a metal particle or more than one molecule. There are, however, several indications that the charge states in the stability diagram belong to one and the same molecule. First of all, the Coulomb diamonds are seen to vary significantly in size. This means that the level spacing Δ contribution to the addition energy in Eq. (1.2) is significant. Therefore, the possibility that the charge states belong to a metal particle is unlikely. Secondly, the slope of the diamond edges which correspond to the gate coupling is seen to be the same for all the diamonds. Since it must be regarded as relatively unlikely that two molecules trapped in the nanogap would end up with exactly the same gate coupling, this also supports the picture of a single molecule.

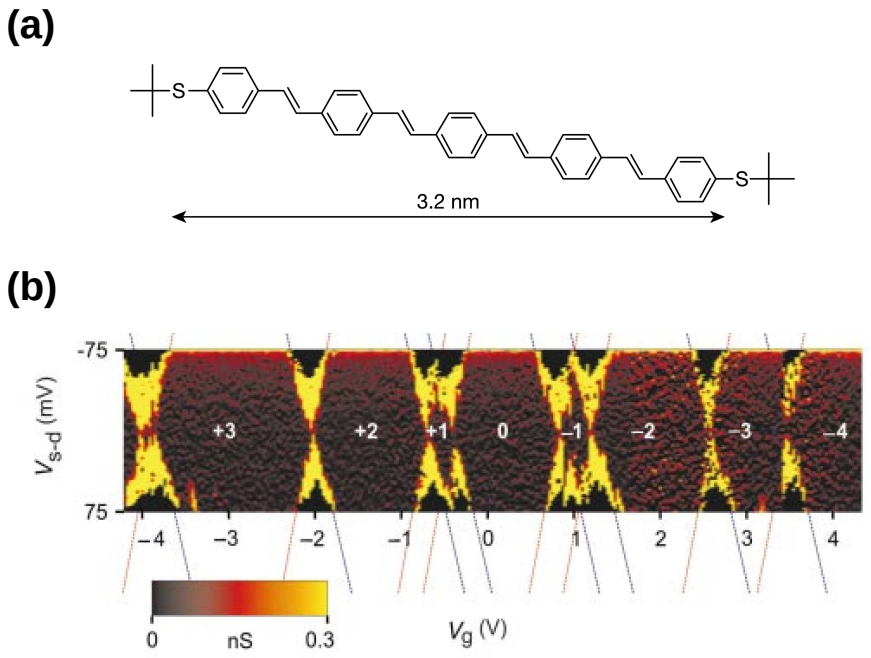

Figure 1.9: Molecular structure and stability diagram showing access to several charge states of the OPV5 molecule [20]. (a) Molecular structure of a thiol-terminated OPV5 molecule. (b) Charge stability diagram showing access to several charge (redox) states of OPV5. The polarization of the junction environment most likely plays an important role for the stability of the large number of observed charge states (see text).

From the complete diamonds corresponding to the charge states $Q \pm 1$ of the molecule, a gate coupling of ~ 0.2 can be inferred. As the width of the diamonds are given by $E_{\mathrm{add}}/(e\alpha)$, the addition energy of the neutral molecule which corresponds to the gap of the molecule in the junction, can be estimated to $\sim 200 - 300$ meV. As discussed in Secs. 1.3.2 and 1.3.3, molecular gaps are expected to be reduced significantly in polarizable junction environments. This is also the interpretation of Ref. [20], which ascribes the origin of the small gap to image charges, i.e. polarization, in the metal electrodes. For reference, the electrochemical gap of the OPV5 molecule was reported to be ~ 2.5 eV. Independent density functional calculation using the B3LYP exchange-correlation functional yields a gap of ~ 4.5 eV for the isolated molecule. Based on the considerations from the simple capacitor model of the C_{60} molecule in Sec. 1.3.2, the reduction of the sum of the HOMO-LUMO gap and the charging energy to a few hundreds of electronvolts seems drastic.

The large difference between the gap of the molecule in the SET envi-

ronment and the electrochemical gap has fueled a discussion whether the interpretation of this experiment is correct [4, 29]. In electrochemical measurements the compensating ions that stabilize the non-neutral redox states of the molecule are only a few Å distant from the molecule. Accordingly, the screening should be more efficient than in a nanojunction. However, the small gap observed in the single-molecule SET suggests the opposite. As pointed out in Sec. 1.3.3, the screening properties of a ionic solution at room temperature and a solid-state environment cooled to cryogenic temperatures are very different. This makes a direct comparison between them difficult. Another argument against the single molecule interpretation of the stability diagram in Fig. 1.9(b), is the large number of observed charge states which must pose a serious challenge for the chemical stability of the molecule. However, the efficient screening of the junction environment play a stabilizing role for the charge states of the molecule. This could be a decisive factor for the chemical stability of the molecule in the large number of charged states observed.

It should be noted that the stability diagram in Fig. 1.9(b) is the only observation of such a large number of charge states in a single-molecule SET so far. This, in conjunction with the fact that weakly coupled molecules in solid-state environments held at cryogenic temperatures is still a relatively unexplored field, must leave the correct interpretation of this experiment as an open question. There is, however, no question that polarization plays an important role for the position of the molecular levels in single-molecule SETs. In experiments where full Coulomb diamonds have been measured, small addition energies have been observed consistently. In Chap. 4 a quantitative estimate of the effect in a realistic OPV5 single-molecule SET is presented.

Spin excitations and Kondo effect

The stability diagram from another experiment on the OPV5 molecule is shown in Fig. 1.10(a) [49]. The schematic drawing in Fig. 1.10 gives an overview of the important information in the stability diagram and the charge states of the diamonds. Similar to the stability diagram in Fig. 1.10, the diagram here consists of diamonds with varying size. As discussed in the previous section this is an indication of the molecule being the active transport pathway for electron tunneling between the electrodes. Another similarity is the small addition energies associated with the charged states. The addition energy for the $Q = +1$ state is ~ 50 meV which is in good agreement with the value for the same charge state in Fig. 1.10(a). Thus, also in this experiment does junction screening seem to be pronounced.

The horizontal features inside the Coulomb diamonds originate from

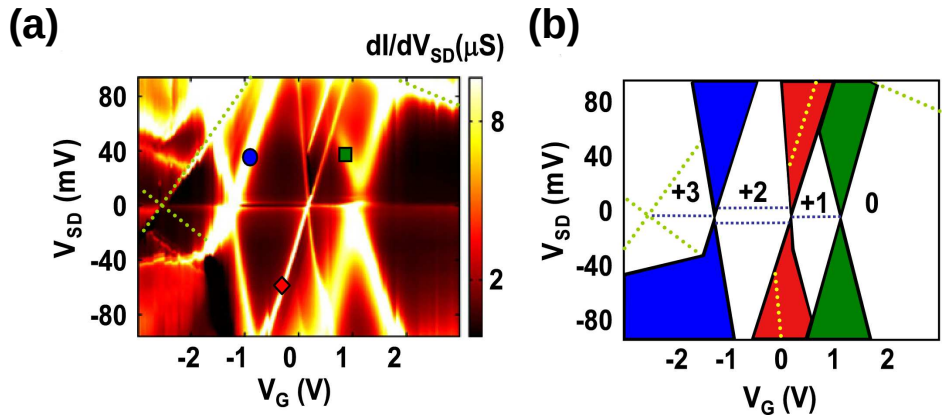

Figure 1.10: Kondo effect and singlet-triplet excitation [49]. (a) Charge stability diagram for the OPV5 molecule showing features from higher-order tunneling processes inside the Coulomb diamonds. (b) Schematic drawing showing the important information contained in the stability diagram. The Kondo effect shows up as a zero-bias feature inside the $Q = +1, +3$ diamonds. The two parallel lines inside the $Q = +2$ diamond are due to inelastic cotunneling that leaves the molecule in the excited triplet state (see text).

higher-order tunneling processes. An example is the Kondo effect which manifests itself in a zero-bias resonance inside the Coulomb diamonds in the stability diagram [51, 52]. In Fig. 1.10 this gives rise to the horizontal lines at zero bias inside the $Q = +1, +3$ diamonds. The Kondo resonance arises from a correlated many-body state between a single electron spin on the molecule and the conduction electrons of the leads. Since it requires an unpaired electron spin on the molecule, the zero-bias Kondo resonance appears only in diamonds with odd number of electrons. Hence, the presence of a Kondo resonance can be used to identify the charge states of the measured diamonds.

The two parallel lines inside the $Q = +2$ diamond come from inelastic cotunneling processes which are next-to-leading order in the tunnel coupling between the molecule and the leads. Cotunneling describes processes in which an electron is transferred between the electrodes via an intermediate state of the molecule that can have a higher energy than the initial state. In inelastic cotunneling the molecule is left in an excited state which is why it shows up at finite bias values. In the present case a splitting of the inelastic cotunneling lines in a magnetic field allowed to connect them with the excited triplet state of the doubly charged OPV5 molecule. The energy splitting between the singlet ground state and the excited triplet state can be inferred from the distance between the zero-bias axis and the cotunneling lines. It here amounts to ~ 1.7 meV. The singlet-triplet splitting can be accounted for

by an effective antiferromagnetic exchange coupling J between two spatially separated single-particle states A and B holding the unpaired electrons of the doubly charged molecule,

$$H = J\mathbf{S}_A \cdot \mathbf{S}_B, \tag{1.9}$$

where $\mathbf{S}_{A/B}$ denotes the spin operators. The spatially separated states A and B were ascribed to image charge stabilized localizations of the unpaired spins at the terminating phenylene units in each end of the molecule. This serves to illustrate that the junction polarization not only affects the size of the Coulomb diamonds but also the excitation spectrum of the molecule.

Vibrational excitations

In a last example, the fine structure from the vibrational excitations of the OPV5 molecule was observed [50]. This is shown in the stability diagram in Fig. 1.11(a), where the vibrational excitations shows up as lines running parallel to the edge of the Coulomb diamonds.

The energies of the vibrational excitations correspond to the vertical distance between the zero-bias axis and the point where the excitation lines intersect with the Coulomb diamonds. Excitation energies in the range $1 - 125$ meV could be identified from the stability diagram (a zoom of the stability diagram is show in Fig. 1.11). Furthermore, an overall good agreement with the vibrational modes from Raman and IR spectroscopy was obtained confirming the vibrational nature of the observed excitations. In case the vibrational excitations are equidistant in energy they can be ascribed to different number of phonons created in the same vibrational mode. However, as the excitation energies extracted from Fig. 1.11(a) do not form a harmonic spectrum, they must be attributed to different vibrational modes of the molecule.

It is important to note that due to selection rules between the different vibrational states, not all vibrational excitations will show up in the stability diagram. These selection rules are dictated by the Franck-Condon factors which are essentially overlap integrals between the vibrational states of the molecule. In the case of a strong electron-phonon coupling, i.e. where there is a large displacement of the nuclei upon charging of the molecule, the overlap between the vibrational ground states can become vanishingly small. This is illustrated in Fig. 1.11(b) where the two parabolas correspond to potential energy surfaces of the molecule in two charge states. As a result the ground state to ground state transition is drastically suppressed which in turn leads to a blocking of the current at low bias. This phenomenon is known as the Franck-Condon blockade [53, 54].

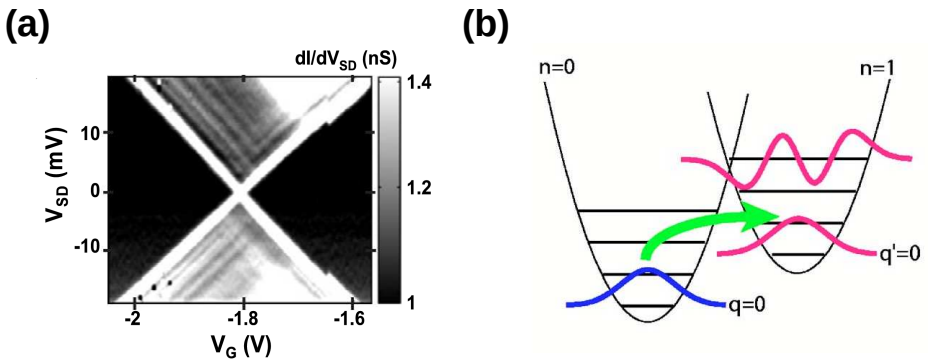

Figure 1.11: Vibrational excitations of the OPV5 molecule [50]. (a) Stability diagram with a detailed fine structure from the vibrational excitations of the OPV5 molecule. The excitations appears as lines parallel to the diamonds edges. (b) Potential energy surfaces as a function of a general nuclei coordinate q for two charge states of a molecule. For a strong electron-phonon coupling the horizontal displacement between the energy surfaces is large resulting in a suppression of the transition indicated by the green arrow. This gives rise to the Franck-Condon blockade (see text).

1.3.5 Theoretical descriptions

Theoretical descriptions of single-molecule SETs are typically based on a two-step procedure. In the first step the molecular states which are involved in the electron transport are determined. In a second step, the current is calculated from a stationary solution to the so-called Master equations. The following section gives a brief overview of this approach together with some considerations on different methods for the determination of the molecular states.

The starting point is the following generic junction Hamiltonian

$$H = H_{\text{mol}} + H_{\text{leads}} + H_t \tag{1.10}$$

where H_{mol} denotes the Hamiltonian of the molecule, H_{leads} the Hamiltonian of the electrodes and H_t the tunnel coupling between the two. Due to the weak tunnel coupling the states of the molecule are assumed to be unaffected by the tunnel coupling. Hence, they can be obtained as the many-body states of H_{mol} which are characterized by the number of electrons N on the molecule and a general index i referring to some excited state of the molecule. Under finite bias conditions the occupations of the $|N, i\rangle$-states are given by a non-equilibrium probability distribution $P_{N,i}$ for the states. Treating H_t as a perturbation, the transition rates Γ between the molecular states can be described using Fermi's Golden rule.

Knowing the transition rates, the probability for being in the i'th excited N-electron can be found from the equation

$$\frac{d}{dt}P_{N,i} = \sum_j \left[-\left(\Gamma_{\substack{N+1,j \\ N,i}} + \Gamma_{\substack{N-1,j \\ N,i}} \right) P_{N,i} + \Gamma_{\substack{N,i \\ N+1,j}} P_{N+1,j} + \Gamma_{\substack{N,i \\ N-1,j}} P_{N-1,j} \right], \tag{1.11}$$

which gives the time-derivative of the probability in terms of the rates for tunneling in and out of the state. The set of equation formed by the probabilities for all the considered states are usually referred to as the master equations. From a stationary solution for the probabilities, i.e. $d/dtP_{N,i} = 0$, the current from the sequential tunnel processes can be obtained [55].

The molecular states $|N, i\rangle$ enter the transition rates. The rates for increasing the number of electrons by one are given

$$\Gamma_{\substack{N+1,j \\ N,i}} = \frac{2\pi}{\hbar} \sum_\alpha \Gamma^\alpha_{j,i} f_\alpha(E_{ij}), \tag{1.12}$$

where f_α is the fermi distribution of the electrodes, $E_{ij} = E^{N+1}_j - E^N_i$ is the total energy difference between the molecular states. In the case of i and j referring to ground states of the N and $N+1$ electron molecules, E_{ij} corresponds to the electron affinity (see (1.7)). The alignment between the Fermi energy of the electrodes and the molecular levels are therefore contained in the Fermi function. The factor $\Gamma^\alpha_{j,i}$ is given by

$$\Gamma^\alpha_{j,i} = \rho_\alpha \left| t_\alpha \right|^2 \left| \langle N+1, j | c^\dagger | N, i \rangle \right|^2. \tag{1.13}$$

Here, t_α denotes the tunnel matrix element to the electrodes and ρ_α is the density of states of the electrodes. It is the matrix element between the states $|N, i\rangle$ and $|N+1, j\rangle$ that determines the selection rules for the current-induced transitions between two molecular states. For vibrational excitations the Franck-Condon factors constitute the part of the overlap that deals with the vibrational degrees of freedom.

Since the master equation approach is based on a perturbative treatment to lowest order in the tunneling Hamiltonian H_t, the width of the resonances is determined solely by the temperature. Therefore,

$$E_c, \Delta \gg k_\mathrm{B}T > \Gamma \tag{1.14}$$

in order for the master equation approach to be correct.

Theoretical descriptions of single-molecule SETs most often rely on a model Hamiltonian description that includes the essential physics needed to describe the molecular states of interest. This approach has been extremely

successful in explaining experimentally observed features in the stability diagram and how different molecular degrees of freedom affect the transport through the molecule.

Part of the present work examines the effect of junction polarization on the molecular states and their energetic positions. This requires the total energies of the neutral and charged states of the molecule which are needed to determine the ionization potential and electron affinity. For this purpose first-principles methods which yields accurate total energies are to be preferred instead of a model Hamiltonian approach. Furthermore, as the polarization response of the junction must be expected to be highly dependent on the spatial charge distribution of the molecule, an atomic description taking into account the 3-dimensional structure of the molecule is required to obtain a quantitative estimate of the polarization effects.

1.4 Thesis outline

The present work can be divided up into two parts. The first part, which deals with polarization effects and general characteristics of single-molecule SETs, covers chapters 2-4. The second part which covers chapters 5 and 6 addresses the accuracy of the many-body GW method for describing charge excitations in small molecules. The relevance of this study is connected to the increased use of the GW approximation for the description of the electronic structure of isolated systems. Furthermore, the GW approximation is also applied to describe the electronic structure of metal-molecule interfaces with a significant hybridization between the metal and the molecule. Such interfaces occur for instance in molecular self-assembled monolayers and single-molecule junctions in the strong coupling regime. Their electronic structure is difficult to describe. Factors like hybridization and dipole formation at the interface complicate things considerably as compared to the situation in e.g. single-molecule SETs where the molecule can be treated as an isolated system. As the GW approximation has been demonstrated to take into account the effect of surface polarization on the molecular levels, first-principles GW calculations could be a candidate for an accurate descriptions of metal-molecule interfaces. It is therefore of relevance to known how the GW approximation describes the electronic structure of the isolated molecule.

The following paragraphs give an overview of the contents of the remaining chapters of this thesis. Equations in these chapters are given in atomic units (see App. A).

In Chap. 2, a general Hamiltonian describing the molecular states that enter the master equations via the rates in Eq. (1.13) is given. Most im-

portantly, this Hamiltonian takes into account the interaction between the charge carriers on the molecule and their polarization cloud in the junction environment. This framework allows to study the effect of junction polarization on the molecular levels.

Chap. 3 gives an introduction to Poisson's equation and the electrostatic Green's function which plays an important role in the framework presented in Chap. 2. Furthermore, a brief overview of the finite element method which has been used to solve Poisson's equation in the present work is given.

Chap. 4 presents a study of a OPV5-based single-molecule SET. Most of the results presented here were published in the attached Paper I. The effect of junction polarization on the molecular levels, the gate coupling to the molecule, and the behavior of the molecular states at non-zero bias is addressed. The properties of the OPV5-SET described in this chapter can be expected to be relevant for single-molecule SETs in general.

Chap. 5 introduces the many-body GW approximation and gives a brief account of first-principles GW calculations. Recent calculations studying single molecules physisorbed on metallic surfaces are discussed. These calculations have demonstrated that the GW approximation takes into account the shift of the molecular levels due to the polarization of the surface.

Finally, Chap. 6 presents GW benchmark calculations for a range of small conjugated molecules described with the semi-empirical Pariser-Parr-Pople Hamiltonian. By comparing to exact results an unbiased estimate of the performance of the GW approximation is obtained. The results in this chapter have been collected in Paper II, which at the time of writing has not yet been published.

Chapter 2

Electrostatics of single-molecule SETs

In single-molecule SETs where the molecule is surrounded by metallic electrodes and a gate dielectric, the molecular states and their energetic positions can not be assumed to be those of the isolated molecule. For example, the electric field from an applied source-drain voltage may polarize the molecule and thereby alter the molecular states [56]. Another important factor is the polarization of the metallic electrodes and the gate dielectric that accompanies the charging of the molecule when a current is running through the junction. Due to the short distance between the molecule and the junction environment the Coulomb interaction with the induced polarization/image charge can be on the order of eV leading to significant shifts of the molecular levels. As the threshold for electron transport through the SET is determined by the positions of the molecular levels with respect to the Fermi levels of the electrodes, this is an important effect to include in theoretical descriptions of single-molecule SETs.

The following chapter presents a general framework that allows to study the effect of polarization in realistic single-molecule SET geometries. It is based on general considerations on the macroscopic electrostatic energy of the junction environment for a given charge on the molecule. From these considerations an effective Hamiltonian for the single-molecule SET that includes the polarization effects is derived. It should be noted that similar approaches have been reported previously in the literature [57, 58].

Alternative DFT approaches addressing the effect of polarization in molecular junctions in the weakly coupled regime has recently been published [59, 60]. However, since they rely on an atomic description of both the molecule and the polarizable environment simulations of realistic single-molecule SETs are numerically intractable.

Despite the focus being on single-molecule SETs here, the method presented in the following applies equally well to other nanostructures in macroscopic dielectric environments. The discussion is therefore kept general in the following section.

2.1 Junction Hamiltonian

The starting point for the following analysis is a nanojunction consisting of a nanoscale system S, e.g. a molecule, and the junction environment E which usually consists of a number of metallic electrodes and a gate dielectric separating the system from gate electrode. The situation is sketched in Fig. 2.1 which illustrates the polarization and charge distribution of the junction for a positive gate voltage and charge $Q = -e$ on the system S. In order to calculate the position of the electronic levels of the system, the total energy of the system plus junction must be evaluated as a function of the charge Q on the system. This is a consequence of long ranged Coulomb interaction which couples the system charge with the polarization charge in the junction. With all the microscopic degrees of freedom of the junction environment, this of course posses an unsolvable problem. However, if the junction environment is described with classical macroscopic electrostatics the problem simplifies considerably. Within this approach the metallic electrodes are represented by equipotentials with their potentials given by the applied voltages V_i. It is assumed that there is no net accumulation of charge in the junction environment, i.e. $\rho_{_E} = 0$, when the junction is considered without the system S and in the absence of applied voltages.

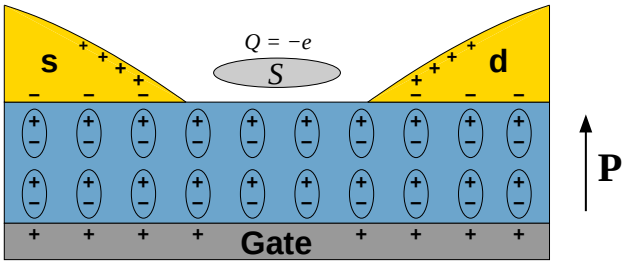

Figure 2.1: Schematic illustration of the charge distribution and polarization **P** of the junction with a positive voltage applied to the gate electrode and the source (**s**) and drain (**d**) electrodes grounded. The positive gate voltage has left the system S in the charge state $Q_{_S} = -e$. The positive charges on the surface of the source and drain electrodes illustrates the polarization charge induced by the extra electron on the system.

The full junction Hamiltonian can be written as a sum of the following four terms,

$$H = H_S + H_{SE} + H_E + H_V. \tag{2.1}$$

The first term is the Hamiltonian of the nanoscale system S, which in general will be a quantum mechanical many-body Hamiltonian. For now, H_S will not have to be specified further.

The second term H_{SE} accounts for the interaction between the system S and the environment E. With the assumption of a weak tunnel coupling between the system and the electrodes, the tunneling part of H_{SE} can be neglected. Only the Coulomb interaction between the system charge and the charge of the environment remains, i.e.

$$H_{SE} = \int d\mathbf{r} \int d\mathbf{r}' \; \rho_S(\mathbf{r}) V_C(\mathbf{r} - \mathbf{r}') \rho_E(\mathbf{r}'). \tag{2.2}$$

Here $V_C(\mathbf{r} - \mathbf{r}') = 1/|\mathbf{r} - \mathbf{r}'|$ denotes the Coulomb interaction and $\rho_{S/E}$ the charge distributions of the system and the environment. Both ρ_S and ρ_E are considered to be the total charge distribution having contributions from both the electrons and the ions of the system and the junction environment.

The third term H_E in Eq. (2.1) describes the polarization of the junction environment and accounts for the energy associated with the build-up of the induced polarization charge of the environment. In electrostatics there is a qualitative difference between the polarization of a metal and that of a dielectric. In the former the polarization is caused by free electrons which accumulates on the surface until the external electric field causing the polarization has been completely expelled from the bulk of the metal. In dielectrics the situation is different. Here the polarization is generated by small dipoles $\mathbf{p}_i$ in the bulk of the dielectric. This gives rise to a macroscopic polarization $\mathbf{P} = \sum_i \mathbf{p}_i$ which only partially screens an external field. The net bound charge ρ_b that resides in the dipoles is related to the polarization via $\rho_b = -\nabla \cdot \mathbf{P}$. With the polarization of the environment characterized by (i) the free electrons in the metallic electrodes, and (ii) the macroscopic polarization of the dielectric, the energy of the environment is written as [61]

$$\begin{aligned} H_E = & \frac{1}{2} \int d\mathbf{r} \int d\mathbf{r}' \; \rho_E(\mathbf{r}) V_C(\mathbf{r} - \mathbf{r}') \rho_E(\mathbf{r}') \\ & + \frac{1}{2} \int d\mathbf{r} \int d\mathbf{r}' \; \mathbf{P}(\mathbf{r}) K(\mathbf{r}, \mathbf{r}') \mathbf{P}(\mathbf{r}'), \end{aligned} \tag{2.3}$$

where the kernel $K = 4\pi\chi_e^{-1}$ is related to the inverse of the electric susceptibility χ_e. The first term in Eq. (2.3) accounts for the Coulomb interaction between net accumulations of charges in the electrodes and dielectric. The

second term describes the elastic polarization energy of the dipoles $\mathbf{p}_i$ which is dominated by short ranged interactions. The polarization of the dielectric is connected to the electric field $\mathbf{E}$ via $\mathbf{P} = \chi_e \mathbf{E}$. Since the energy of the polarized dielectric is specified in terms of its macroscopic polarization, no assumption about the microscopic origin of the polarization is here required. However, it should be noted that an electrostatic description of the dynamical response of the junction environment relies on certain assumptions on the time scale of the polarization response. A comment on this will follow in Sec. 2.3.

In order to write the Hamiltonian of the environment in Eq. (2.3) as an interaction between the environmental charges $\rho_{_E}$, the second term in Eq. (2.3) is recast in the form of a density-density interaction between the bound polarization charges ρ_b,

$$\frac{1}{2}\int d\mathbf{r}\int d\mathbf{r}'\rho_b(\mathbf{r})V_b(\mathbf{r},\mathbf{r}')\rho_b(\mathbf{r}'). \tag{2.4}$$

The interaction V_b between the bound charges is related to the kernel K in Eq. (2.3) [1]. For the present purpose a further specification of V_b is not necessary. With this rearrangement the sum of the two terms in Eq. (2.3) can now be written

$$H_{_E} = \frac{1}{2}\int d\mathbf{r}\int d\mathbf{r}'\ \rho_{_E}(\mathbf{r})V(\mathbf{r},\mathbf{r}')\rho_{_E}(\mathbf{r}'), \tag{2.5}$$

where V is either $V_{_C}$ or $V_{_C} + V_b$ depending on whether $\mathbf{r}$ and $\mathbf{r}'$ belong to the metallic and/or the dielectric parts of the environment.

Finally, the last term of the junction Hamiltonian in Eq. (2.1) is the energy it costs to place a charge Q_i on the i'th electrode which is held at the potential V_i,

$$H_{_V} = \sum_i Q_i V_i. \tag{2.6}$$

[1] Expressing the polarization in terms of the bound charge density via

$$\mathbf{P}(\mathbf{r}) = -\int d\mathbf{r}'\frac{\mathbf{r}-\mathbf{r}'}{|\mathbf{r}-\mathbf{r}'|^2}\rho_b(\mathbf{r}'),$$

the interaction between the bound charges V_b can be written as the following double integral over the extend of the dielectric,

$$V_b(\mathbf{r},\mathbf{r}') = \int d\mathbf{r}''\int d\mathbf{r}'''\frac{\mathbf{r}-\mathbf{r}''}{|\mathbf{r}-\mathbf{r}''|^2}K(\mathbf{r}'',\mathbf{r}''')\frac{\mathbf{r}'''-\mathbf{r}'}{|\mathbf{r}'''-\mathbf{r}'|^2}.$$

The charge on the i'th electrode is given by the spatial integral of $\rho_{_E}$ over the extend of the electrode, $Q_i = \int_{\mathbf{r}\in i} d\mathbf{r}\ \rho_{_E}(\mathbf{r})$. With the different parts of the junction Hamiltonian in Eq. (2.1) specified it now takes the form

$$H = H_{_S} + \rho_{_S} V_{_{SE}} \rho_{_E} + \frac{1}{2}\rho_{_E} V_{_{EE}} \rho_{_E} + \sum_i Q_i V_i, \tag{2.7}$$

where the shorthand notation $V_{mn}\rho_n = \int d\mathbf{r}' V(\mathbf{r},\mathbf{r}')\rho(\mathbf{r}')$ with $m,n = S,E$ has been introduced for brevity. The subscripts in Eq. (2.7) indicate which part of the junction the spatial variable belongs to. In the following it is shown how an explicit treatment of the degrees of freedom of the environment can be avoided.

For a given charge distribution $\rho_{_S}$ of the system and applied voltages V_i to the electrodes, the environment will polarize in order to lower the total energy. Since the part of the Hamiltonian involving $\rho_{_E}$ is treated classically here, the solution for $\rho_{_E}$ can be found by minimizing the Hamiltonian in Eq. (2.7) with respect to $\rho_{_E}$. This yields the following expression for charge distribution of the junction environment

$$\begin{aligned} \rho_{_E} &= -[V_{_{EE}}]^{-1}\left(V_{_{ES}}\rho_{_S} + \sum_i V_i\right) \\ &\equiv \rho_{\text{ind}} + \rho_{\text{ext}}. \end{aligned} \tag{2.8}$$

Two contributions are here identified. The first denoted ρ_{ind}, represents the polarization charge induced by the system charge $\rho_{_S}$. In linear response theory the response function χ relates the induced charge density to an external potential,

$$\rho_{\text{ind}}(\mathbf{r}) = \int d\mathbf{r}' \chi(\mathbf{r},\mathbf{r}')\Phi(\mathbf{r}'). \tag{2.9}$$

In Eq. (2.8) above, the potential from the system charge $\Phi_{_S} = V_{_{ES}}\rho_{_S}$ takes the role of the external potential. Therefore, the inverse of the interaction $V_{_{EE}}$ can be identified as the linear response function of the junction, $\chi = -V_{_{EE}}^{-1}$.

The second contribution ρ_{ext} to the charge distribution of the environment in Eq. (2.8), represents the charge induced in the junction when external voltages V_i are applied to the electrodes. This consists of the charge that is supplied by an external battery in order to maintain the applied voltages, plus the charge that results from the polarization of the dielectric that follows a finite voltage applied to one or more of the electrodes (see e.g. Fig. 2.1).

With the expression for $\rho_{_E}$ in Eq.(2.8) inserted back into the Hamiltonian

in Eq. (2.7), the following effective junction Hamiltonian is obtained,

$$\begin{aligned} H &= H_{S} - \frac{1}{2}\rho_{S} V_{SE}[V_{EE}]^{-1} V_{ES}\rho_{S} - \sum_{i} V_{i}[V_{EE}]^{-1} V_{ES}\rho_{S} \\ &\quad - \frac{1}{2}\sum_{ij} V_{i}[V_{EE}]^{-1} V_{j} \\ &= H_{S} + \frac{1}{2}\int d\mathbf{r}\int d\mathbf{r}'\ \rho_{S}(\mathbf{r})\widetilde{V}(\mathbf{r},\mathbf{r}')\rho_{S}(\mathbf{r}') + \int d\mathbf{r}\ \rho_{S}(\mathbf{r})\Phi_{\text{ext}}(\mathbf{r}) \\ &\quad + \frac{1}{2}\sum_{ij} V_{i} C_{ij} V_{j} \\ &\equiv H_{S} + H_{\text{pol}} + H_{\text{ext}} + H_{C}. \end{aligned} \tag{2.10}$$

The elimination of the charge density of the environment ρ_{E} has resulted in the appearance of new quantities in the Hamiltonian. These are defined by the second equality where the real space notation has been reintroduced. Firstly, an effective interaction

$$\widetilde{V} = -V_{SE}[V_{EE}]^{-1} V_{ES} \tag{2.11}$$

between the system charges has been identified. As will be discussed in Sec. 2.1.2, this interaction is mediated by the induced polarization charge. Secondly, the electrostatic potential $\Phi(\mathbf{r})_{\text{ext}} = \int d\mathbf{r}' V_{C}(\mathbf{r}-\mathbf{r}')\rho_{\text{ext}}(\mathbf{r}')$ from the charge distribution ρ_{ext} in Eq. (2.8) has been introduced. Last, the elements C_{ij} of the capacitance matrix are identified as

$$C_{ij} = -\int_{\mathbf{r}\in i} d\mathbf{r} \int_{\mathbf{r}'\in j} d\mathbf{r}'\ V^{-1}(\mathbf{r},\mathbf{r}'), \tag{2.12}$$

where the integration extends over the volume of the i'th and j'th electrode and V is the interaction in the environment from Eq. (2.5). As the inverse V^{-1} of the interaction is related to the response function, the capacitance matrix is fully determined by the geometry of the junction and its dielectric properties.

Each of the terms in the effective Hamiltonian in Eq. (2.10) accounts for well defined contributions to the total energy. Starting with the last term, H_{C} is the electrostatic energy of the junction in the absence of the system S and with voltages V_{i} applied to the electrodes. This part of the electrostatic energy is provided by a battery and has no influence on the electronic levels of the system. The term H_{ext}, is the energy of the system charge ρ_{S} in the potential from the applied voltages. The capacitive coupling to the gate electrode is described by this term. The polarization Hamiltonian H_{pol}

accounts for the interaction between the system charge and the polarization charge. Assuming for a moment that $\rho_{_S}$ is a classical charge distribution (a quantum mechanical treatment will follow in the next section), this term can be expressed in terms of the potential $\Phi(\mathbf{r})_{\text{ind}} = \int d\mathbf{r}' V_{_C}(\mathbf{r}-\mathbf{r}')\rho_{\text{ind}}(\mathbf{r}')$ from the induced polarization charge ρ_{ind} in Eq. (2.8),

$$H_{\text{pol}} = \frac{1}{2}\,\rho_{_S} V_{_{SE}} \rho_{\text{ind}} = \frac{1}{2}\int d\mathbf{r}\;\rho_{_S}(\mathbf{r})\Phi_{\text{ind}}(\mathbf{r}). \tag{2.13}$$

This term is exactly half of the Coulomb interaction between the system charge and the polarization charge in Eq. (2.2). The factor of one half arises because the energy from Eq. (2.3) required to build up the polarization charge in the environment is included in this term. In other words, this means that the energy associated with building up the polarization charge in the environment is exactly half of the Coulomb interaction between the system charge and the polarization charge.

The polarization Hamiltonian in Eq. (2.13) can be regarded as a generalization of the classical image charge problem illustrated in Fig. 2.2. It considers a point charge q placed in front of a perfect conducting surface. The potential from the induced surface charge at the position z of the charge q is identical to the potential $\Phi_{\text{image}}(z) = -q/2z$ from a fictitious image charge $q' = q$ located behind the surface. The total energy of the surface plus charge,

$$E(z) = \frac{1}{2} q \Phi_{\text{image}}(z) = -\frac{q^2}{4z}, \tag{2.14}$$

is only half of this [62]. The reason for this can be understood by considering the energy stored in the electric field $\mathbf{E}$,

$$E = \frac{1}{8\pi}\int d\mathbf{r}\;|\mathbf{E}|^2. \tag{2.15}$$

For the situation illustrated in Fig. 2.2 the field from the charge q is only different from zero for $z > 0$ due to the perfect screening from the conducting surface. However, if both charges q and q' are considered to be real charges, the field is different from zero also for $z < 0$. Due to symmetry the energy of the former situation is therefore exactly half of the energy of the latter situation. As the energy of the two real charges is $E(z) = -q^2/(2z)$, the result in Eq. (2.14) follows directly. With the result for the polarization Hamiltonian in Eq. (2.13), this has been generalized to an arbitrary geometry of the polarizable environment.

To summarize the present section, it has been shown how an effective junction Hamiltonian in Eq. (2.10) can be derived from general consideration

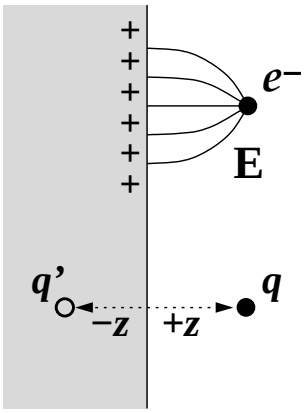

Figure 2.2: The classical image charge problem with a charge $q = -e$ located at a distance z from a perfect conducting surface. The effect of the positive surface charge is equivalent to a fictitious image charge $q' = -q$ behind the metal surface.

on the electrostatic energy of the junction. In the resulting Hamiltonian the charge distribution of the junction environment has been replaced by macroscopic quantities describing the mutual interaction between the charges of the environment and their interaction with the system. These include an effective interaction $\widetilde{V}$ between the system charges, the potential Φ_{ext} from the charge ρ_{ext} which is added to the electrodes to maintain the applied voltages V_i, and the elements C_{ij} of the capacitance matrix of the junction.

2.1.1 Quantum mechanical version

For systems where the electronic degrees of freedom are governed by the Schrödinger equation, a quantum mechanical version of the effective junction Hamiltonian in Eq. (2.10) is required.

In its most general form the Hamiltonian of the system will be a many-body Hamiltonian consisting of a non-interaction part H_0 including the kinetic energy of the electrons and the potential from the ionic cores of the system, and an interacting part H_{int} which describes the Coulomb interaction between the electrons,

$$\begin{aligned} H_{_S} &= H_0 + H_{\text{int}} \\ &= -\frac{1}{2}\int d\mathbf{r}\ \psi^\dagger(\mathbf{r})\nabla^2\psi(\mathbf{r}) + \int d\mathbf{r}\ \psi^\dagger(\mathbf{r})\psi(\mathbf{r})V_{\text{ion}}(\mathbf{r}) \\ &\quad + \frac{1}{2}\int d\mathbf{r}\int d\mathbf{r}'\ \psi^\dagger(\mathbf{r})\psi^\dagger(\mathbf{r}')V_{_C}(\mathbf{r}-\mathbf{r}')\psi(\mathbf{r}')\psi(\mathbf{r}). \end{aligned} \tag{2.16}$$

Here $\psi^\dagger$ and ψ denote the creation and annihilation field operators and

$V_{\text{ion}}(\mathbf{r}) = -\int d\mathbf{r}\, V_C(\mathbf{r}-\mathbf{r}')\rho_{\text{ion}}(\mathbf{r}')$ is the energy of the electrons in the potential from the ionic cores. To ease the notation, the electronic spin variable has been suppressed in Eq. (2.16) and in the remainder of this chapter.

The quantum mechanical version of the effective junction terms in Eq. (2.10) follows by replacing the charge distribution of the system by its contributions from the ionic cores and the electrons with the latter represented by the electronic field operators, i.e. $\rho_S = \rho_{\text{ion}} - \psi^\dagger\psi$. The term H_{ext} accounting for the applied voltages takes the form

$$H_{\text{ext}} = \int d\mathbf{r} \left[\rho_{\text{ion}}(\mathbf{r}) - \psi^\dagger(\mathbf{r})\psi(\mathbf{r})\right] \Phi_{\text{ext}}(\mathbf{r}). \tag{2.17}$$

Under the assumption that the ionic cores of the system S remain fixed as a function of applied voltages and number of electrons on the system, the first term affects only the zero point of the total energy and can hence be neglected. The single-particle contribution in the other term adds to the non-interaction part H_0 of the system Hamiltonian. It affects the eigenstates and hence also the electronic charge distribution of the system when voltages are applied to the electrodes. Furthermore, this term accounts for the shift of the electronic levels due to an applied gate voltage.

The quantum mechanical version of the polarization Hamiltonian H_{pol} is given by

$$\begin{aligned} H_{\text{pol}} = \frac{1}{2}\int d\mathbf{r} \int d\mathbf{r}'\ \rho_{\text{ion}}(\mathbf{r})\widetilde{V}(\mathbf{r},\mathbf{r}')\rho_{\text{ion}}(\mathbf{r}') \\ - \int d\mathbf{r} \int d\mathbf{r}'\ \psi^\dagger(\mathbf{r})\psi(\mathbf{r})\widetilde{V}(\mathbf{r},\mathbf{r}')\rho_{\text{ion}}(\mathbf{r}') \\ + \frac{1}{2}\int d\mathbf{r} \int d\mathbf{r}'\ \psi^\dagger(\mathbf{r})\psi(\mathbf{r})\widetilde{V}(\mathbf{r},\mathbf{r}')\psi^\dagger(\mathbf{r}')\psi(\mathbf{r}'), \end{aligned} \tag{2.18}$$

where $\widetilde{V}$ is the effective interaction between the system charges from Eq. (2.11). Again, the term involving the ionic charge distribution ρ_{ion} can be neglected under the assumption that the ionic cores remain fixed. The second term contains the interaction between the electrons and the image charges of the ions and visa versa. This is a single-particle term that adds to H_0 as above. The last term, which in the following will be denoted $H_{\text{pol}}^{\text{int}}$, describes the interaction between the electrons and their image charges. Except for the ordering of the field operators and the substitution of the Coulomb interaction V_C with the effective interaction $\widetilde{V}$, this term is equivalent to the interaction part H_{int} of the system Hamiltonian in Eq. (2.16). Due to the different ordering of the field operators in $H_{\text{pol}}^{\text{int}}$, this term includes contributions where the electrons interact with themselves. This self-interaction is a

consequence of the fact that an electron can interact with itself via its own image charge. By reordering the field operators, the self-interaction of the electrons can be separated out in an extra single-particle term

$$H_{\rm pol}^{\rm int} = \frac{1}{2}\int d\mathbf{r}\ \psi^\dagger(\mathbf{r})\psi(\mathbf{r})\widetilde{V}(\mathbf{r},\mathbf{r}) + \frac{1}{2}\int d\mathbf{r}\int d\mathbf{r}'\ \psi^\dagger(\mathbf{r})\psi^\dagger(\mathbf{r}')\widetilde{V}(\mathbf{r},\mathbf{r}')\psi(\mathbf{r}')\psi(\mathbf{r}). \tag{2.19}$$

The last term now has the same ordering of the field operators as the Coulomb interaction term $H_{\rm int}$ in the system Hamiltonian. Consequently, the polarization of the environment modifies the interaction on the system by replacing the bare Coulomb interaction with a screened interaction $V_{\rm scr} = V_{_C} + \widetilde{V}$. On top of this, the polarization Hamiltonian introduced two new single-particle terms (the second term in Eq.(2.18) and the first term in Eq. (2.19)). Except for the self-interaction term in Eq. (2.19), all terms in the polarization Hamiltonian have equivalent counterparts in the system Hamiltonian $H_{_S}$ in Eq. (2.16) with $\widetilde{V}$ replaced by the Coulomb interaction $V_{_C}$. They can therefore be joined and expressed in terms of the screened interaction $V_{\rm scr}$. The full quantum mechanical version of the effective junction Hamiltonian in Eq. (2.10) then takes the form

$$\begin{aligned} H = &-\frac{1}{2}\int d\mathbf{r}\ \psi^\dagger(\mathbf{r})\nabla^2\psi(\mathbf{r}) + \int d\mathbf{r}\ \psi^\dagger(\mathbf{r})\psi(\mathbf{r})V_{\rm ext}(\mathbf{r}) \\ &- \int d\mathbf{r}\int d\mathbf{r}'\ \psi^\dagger(\mathbf{r})\psi(\mathbf{r})V_{\rm scr}(\mathbf{r},\mathbf{r}')\rho_{\rm ion}(\mathbf{r}') \\ &+ \frac{1}{2}\int d\mathbf{r}\int d\mathbf{r}'\ \psi^\dagger(\mathbf{r})\psi^\dagger(\mathbf{r}')V_{\rm scr}(\mathbf{r},\mathbf{r}')\psi(\mathbf{r}')\psi(\mathbf{r}) \\ &+ \frac{1}{2}\int d\mathbf{r}\ \psi^\dagger(\mathbf{r})\psi(\mathbf{r})\widetilde{V}(\mathbf{r},\mathbf{r}), \end{aligned} \tag{2.20}$$

where the terms not depending on the electronic degrees of freedom have been neglected. This Hamiltonian provides a general starting point for a description of the electronic structure of a system which is weakly coupled to the metallic electrodes of a nanoscale junction. Since it is merely a modification of the terms contained in the Hamiltonian of the isolated system in Eq. (2.16), the junction Hamiltonian can be tackled with existing methods for many-body eigenvalue problems. These range from exact diagonalization to mean-field treatments in the Hartree and Hartree-Fock approximation. In Sec. 2.2 the version of the junction Hamiltonian suitable for effective single-particle descriptions such as e.g. density functional theory, is presented.

2.1.2 The screened Coulomb interaction

The screened Coulomb interaction of the system introduced above consists of two parts, (i) the direct Coulomb interaction $V_{_C}$ between the system charges, and (ii) the effective interaction $\widetilde{V}$ that arises from the interaction with polarization charge in the junction environment. Utilizing the connection between the response function and the inverse of the interaction $V_{_{EE}}$ in the junction environment, the screened interaction can be illustrated diagrammatically as

$$\begin{aligned} V_{\rm scr}(\mathbf{r},\mathbf{r}') &= V_{_C}(\mathbf{r}-\mathbf{r}') + \widetilde{V}(\mathbf{r},\mathbf{r}') \\ &= V_{_{SS}} + V_{_{SE}}\chi_{_{EE}}V_{_{ES}} \\ &= \quad + \quad . \end{aligned} \tag{2.21}$$

The wiggly lines represent the Coulomb interaction and the bubble diagram represents the response function of the junction. Since the present approach has not made any assumptions on the nature of junction polarization, the response function must in general be considered to include both the electronic and ionic responses of the junction environment. The full diagram in the last term that represents the effective interaction $\widetilde{V}$ has the following physical interpretation. With a unit point charge placed in $\mathbf{r}'$, $\widetilde{V}$ is the potential from the polarization charges in $\mathbf{r}$ that another point charge would feel. Adding to this the direct Coulomb interaction between the two point charges, the screened interaction $V_{\rm scr}$ represents the total potential in $\mathbf{r}$ due to a point charge in $\mathbf{r}'$. This corresponds to the general definition of a screened Coulomb interaction which takes into account the combined potentials of the bare charge and the polarization charge.

In the case of a macroscopic dielectric environment the screened interaction is given by the electrostatic Green's function [57]

$$V_{\rm scr}(\mathbf{r},\mathbf{r}') = G(\mathbf{r},\mathbf{r}'). \tag{2.22}$$

The screened interaction can therefore be obtained from a solution to Poisson's equation. The electrostatic Green's function is introduced in Sec. 3.2. Since the electrostatic Green's function can be separated in two contributions equivalent to those of the screened interaction in Eq. (2.21), it also provides the electronic self-interaction $\widetilde{V}$ in the last term of Eq. (2.20) .

2.2 Effective single-particle Hamiltonian

First-principle methods based on density functional theory (DFT) and Hartree-Fock are among the most widely used for the calculation total en-

ergies of molecules. Therefore, a reformulation of the junction Hamiltonian in Eq. (2.20) to an effective single-particle Hamiltonian is of high practical relevance.

In effective single-particle descriptions the electrons are treated as non-interacting moving in an effective potential that accounts for the electron-electron interactions at the level of mean-field theory. The difference between various single-particle descriptions lies in their approximation to the effective single-particle potential V_{eff}.

Without loss of generality an effective single-particle Hamiltonian can be written as

$$H_{\text{eff}} = -\frac{1}{2}\nabla^2 + V_{\text{eff}}(\mathbf{r}) \tag{2.23}$$

with the effective potential given by the sum of the following contributions

$$V_{\text{eff}}(\mathbf{r}) = V_{\text{ion}}(\mathbf{r}) + V_{\text{H}}(\mathbf{r}) + V_{\text{xc}}(\mathbf{r}) + V_{\text{ind}}(\mathbf{r}) + V_{\text{ext}}(\mathbf{r}). \tag{2.24}$$

The first three terms of the effective potential originate from the molecule itself. They include the potential V_{ion} from the ionic cores, the Hartree potential from the electron density n_e,

$$V_{\text{H}}(\mathbf{r}) = \int d\mathbf{r}'\, V_{C}(\mathbf{r}-\mathbf{r}')n_e(\mathbf{r}'), \tag{2.25}$$

and the exchange-correlation potential V_{xc} which accounts for the part of the electron-electron interactions not included in the Hartree potential. This could be e.g. the exchange-correlation potential from the Kohn-Sham Hamiltonian in DFT or the non-local exchange potential of Hartree-Fock [63]. The fourth term describes the interaction with the polarization charge through the induced potential V_{ind}. It follows from a Hartree approximation to the image charge mediated electron-electron interactions in the polarization Hamiltonian in Eq. (2.18). Since self-interactions are included in this interaction, the Hartree approximation captures the essential physics of this term. It should be noted that $V_{\text{ind}} = V_{\text{ind,e}} + V_{\text{ind,ion}}$ is the sum of the potentials induced by the electrons and the ionic cores of the molecule. The last contribution to the effective potential in Eq. (2.24) accounts for the potential from applied voltages.

The electron density is obtained by occupying the lowest lying eigenfunction ϕ_i of the effective Hamiltonian in Eq. (2.23)

$$n_e(\mathbf{r}) = \sum_{i\in\text{occ}} |\phi_i(\mathbf{r})|^2. \tag{2.26}$$

As the effective potential depends on the electron density, the eigenfunctions and their corresponding energies ε_i must be determined self-consistently by

updating the effective potential from the electron density in each iteration. The self-consistent scheme allows the electron density of the molecule to relax in response to the junction polarization and applied voltages which are represented by the induced potential V_{ind} and the external potential V_{ext}, respectively. As a consequence, the molecular orbitals ϕ_i might change qualitatively compared to those of the isolated molecule.

From the eigenvalues of the effective Hamiltonian the total energy can be obtained as

$$E = \sum_{i\in\mathrm{occ}} \varepsilon_i - \frac{1}{2}\int d\mathbf{r}\; n_e(\mathbf{r})\left[V_{\mathrm{H}}(\mathbf{r}) + V_{\mathrm{ind},e}(\mathbf{r})\right] + \Delta_{\mathrm{xc}}. \tag{2.27}$$

Here the second term prevents double counting contributions to the total energy which are included twice in the sum of the eigenvalues. Notice that this term includes only the induced potential $V_{\mathrm{ind},e}$ from the electronic charge and not the full induced potential V_{ind}. The last term Δ_{xc}, which accounts for the exchange-correlation part of the total energy, depends on the different single-particle descriptions.

The results presented in this thesis are based on the semi-empirical method outlined in App. B. It is based on the extended Hückel scheme which for the present purpose has been extended with a self-consistent field taking into account electron-electron interactions at the level of Hartree theory. The potentials V_{ind} and V_{ext} are obtained from a finite element solution to Poisson's equation. The next chapter introduces Poisson's equation and the finite element method.

2.3 Validity of an electrostatic approach

The derivation of the effective junction Hamiltonian in Eq. (2.20) relies on the assumption that the junction environment can be described by a classical electrostatic Hamiltonian. Below it is discussed which requirements this imposes on the size of the junction constituents and the time scales of the junction polarization.

First of all, the classical treatment is based on the macroscopic dielectric properties of the junction environment. Therefore, the dimensions of the electrodes and dielectric must be sufficiently large that these can be defined. For the metallic electrodes which are assumed to be equipotentials, this implies that their size must be larger than the metallic screening length. With typical metallic screening lengths being on the order of $1-2$ Å [62], this is readily fulfilled. The macroscopic polarization $\mathbf{P}$ of a dielectric follows by averaging the microscopic fluctuations over a suitable volume. For a crystalline solid

this is the unit cell. Hence, the dimensions of the dielectric components of the junction must be larger than the unit cell dimensions. As the gate dielectric in single-molecule SETs is on the order of nanometers, this is also fulfilled.

Secondly, the assumption of an electrostatic environment neglects dynamical polarization effects. For this to hold the dynamics of the polarization response need to be the fastest time scale in the problem such that the environment can be assumed to responds instantaneously to changes in the number of electrons on the molecule. Based on the time-scale discussion in Sec. 1.3.3 which introduced the junction polaron concept, this seems to be well justified. An electrostatic approach is therefore a good starting point for studying polarization effects in single-molecule SETs.

There is another time scale associated with the electron dynamics internally on the molecule. It is given by the energy of the molecular gap which is on the order of $\sim$ eV. For time scales faster than the one set by the molecular gap the molecular orbitals of an effective single-particle approach are not well-defined. As the time scale given by the inverse of the plasmon frequency is also on the order of eV, this implies that a single-particle description of the polarization effects does not necessarily give a correct description of the molecular wavefunction. Alternatively, the problem should be attacked in its many-body form in Eq. (2.20) which takes into account the image charges of the electronic point charges instead of the image charge of the molecular orbitals. However, as a first iteration of the study of polarization effects in single-molecule SETs, the effective single-particle description adopted in the present work can be expected to give the order of magnitude of the effect on the molecular levels.

Chapter 3

Poisson's equation

The spatial profile of the electrostatic potential in the nanoscale gap of a single-molecule SET is an important factor for its transistor related properties. Therefore, the solution of Poisson's equation in a realistic 3-dimensional geometry is a compulsory part in the characterization of the electrostatic properties of single-molecule SETs. The following chapter discusses the different contributions to the electrostatic potential in a single-molecule junction. Furthermore, the numerical finite element method for the solution of Poisson's equation is introduced.

3.1 Junction potential

The electrostatic potential Φ in a nanojunction is given Poisson's equation

$$-\nabla \cdot [\varepsilon_r(\mathbf{r})\nabla\Phi(\mathbf{r})] = 4\pi\rho_{_S}(\mathbf{r}) \tag{3.1}$$

with boundary conditions given by the voltages applied to the electrodes

$$\Phi(\mathbf{r})|_{\mathbf{r}\in S_i} = V_i. \tag{3.2}$$

Here S_i denotes the surface of the i'th electrode with potential V_i. The screening properties of the junction are included via the spatially dependent dielectric constant ε_r and $\rho_{_S}$ is the charge distribution of the system/molecule.

Due to the superposition principle the total potential of the junction can be split up in a part $\Phi_{_S}$ describing the part of the potential that stems from the presence of the charge distribution $\rho_{_S}$ and a part Φ_{ext} associated with the applied voltages V_i,

$$\Phi(\mathbf{r}) = \Phi_{_S}(\mathbf{r}) + \Phi_{\text{ext}}(\mathbf{r}). \tag{3.3}$$

The potential $\Phi_{_S}$ obeys the Poisson equation in Eq. (3.1) with boundary conditions $\Phi(\mathbf{r}) = 0$ for $\mathbf{r} \in S_i$. The remaining part of the total potential is the potential from the applied voltages in the absence of the system charge $\rho_{_S}$ which can be expressed by the sum

$$\Phi_{\text{ext}}(\mathbf{r}) = \sum_i \alpha_i(\mathbf{r}) V_i \tag{3.4}$$

where the characteristic electrode functions α_i are determined by Laplace's equation

$$\nabla \cdot [\varepsilon_r(\mathbf{r}) \nabla \alpha_i(\mathbf{r})] = 0 \tag{3.5}$$

with boundary conditions $\alpha_i(\mathbf{r}) = \delta_{ij}$ for $\mathbf{r} \in S_j$. The characteristic functions α_i represent the electrostatic potential of the junction with a unit potential applied to electrode i and all other electrodes grounded.

The potential $\Phi_{_S}$ arising due to the presence of the system charge is the sum of the potential $\Phi'_{_S}$ from the system charge itself when considered without the junction and the potential Φ_{ind} from the induced polarization charge ρ_{ind} in the junction

$$\Phi_{_S}(\mathbf{r}) = \Phi'_{_S}(\mathbf{r}) + \Phi_{\text{ind}}(\mathbf{r}). \tag{3.6}$$

Each of the potentials on the right-hand side follows from their corresponding charge distributions

$$\Phi(\mathbf{r}) = \int d\mathbf{r}' \; V_{_C}(\mathbf{r} - \mathbf{r}') \rho(\mathbf{r}'). \tag{3.7}$$

In the following two sections methods for solving Poisson's equation are introduced. While a formal solution can be obtained with the aid of the electrostatic Green's function, in practice, one must often resort to numerical methods such as the finite element method.

3.2 Electrostatic Green's function

The electrostatic Green's function solves Poisson's equation with a δ-function source term

$$-\nabla \cdot [\varepsilon_r(\mathbf{r}) \nabla G(\mathbf{r}, \mathbf{r}')] = 4\pi\delta(\mathbf{r} - \mathbf{r}') \tag{3.8}$$

and boundary conditions

$$G(\mathbf{r}, \mathbf{r}')|_{\mathbf{r} \in S_i} = 0. \tag{3.9}$$

Its interpretation is that it gives the potential at position $\mathbf{r}$ due to a unit point charge in $\mathbf{r}'$. Consequently, the Green's function is fully determined by the

screening properties and the geometry of the junction. As the potential $\Phi_{_S}$ in Eq. (3.6) the Green's function can be written as the sum of two contributions

$$G(\mathbf{r},\mathbf{r}') = \frac{1}{|\mathbf{r}-\mathbf{r}'|} + \widetilde{G}(\mathbf{r},\mathbf{r}'). \tag{3.10}$$

The first term is the bare potential from the point charge in $\mathbf{r}'$ and the second term is the induced junction potential. Notice that the contribution $\widetilde{G}$ is equivalent to the effective interaction $\widetilde{V}$ in Eq. (2.21).

The Green's function gives a formal solution to Poisson's equation for the potential $\Phi_{_S}$ via

$$\Phi_{_S}(\mathbf{r}) = \int d\mathbf{r}'\; G(\mathbf{r},\mathbf{r}')\rho_{_S}(\mathbf{r}'). \tag{3.11}$$

That this is in fact a solution can be readily confirmed by inserting in Poisson's equation (3.1) and utilizing that the Green's function is the solution to Eq. (3.8). Also, the characteristic electrode functions α_i can be expressed in terms of the Green's function as [64]

$$\alpha_i(\mathbf{r}) = -\int_{S_i} dS'\; \varepsilon_r(\mathbf{r})\hat{\mathbf{n}}\cdot\nabla' G(\mathbf{r},\mathbf{r}'), \tag{3.12}$$

where $\hat{\mathbf{n}}$ is an outward pointing normal to the electrode surface S_i.

3.2.1 Analytical solution in simplified junction

In the following an analytic solution for the Green's function in the simplified junction geometry shown in Fig. 3.1 is given. Despite its simple appearance, this junction resembles the screening properties of more realistic junction geometries rather well. The electrodes are represented by infinite parallel metal surfaces with the dielectric material filling the lower half of the spacing between them.

Consider a unit point charge located in $\mathbf{r}' = (x', y', z')$ in the spacing between the electrodes and dielectric. The presence of the point charge induces a polarization in the junction. At the surface of the metallic electrodes the potential from the induced charge cancels the potential from the point charge. This results in the boundary condition in Eq. (3.9) for the Green's function at the electrode surfaces. At the dielectric interface the cancellation of the point charge potential is only partial. The potential can be obtained by solving Eq. (3.8) where the dielectric constant ε_r describes the screening of the dielectric. Alternatively, the induced charge of the dielectric can be treated as a source term on equal footing with the point charge. With the induced charge included explicitly as a source term, Poisson's equation must

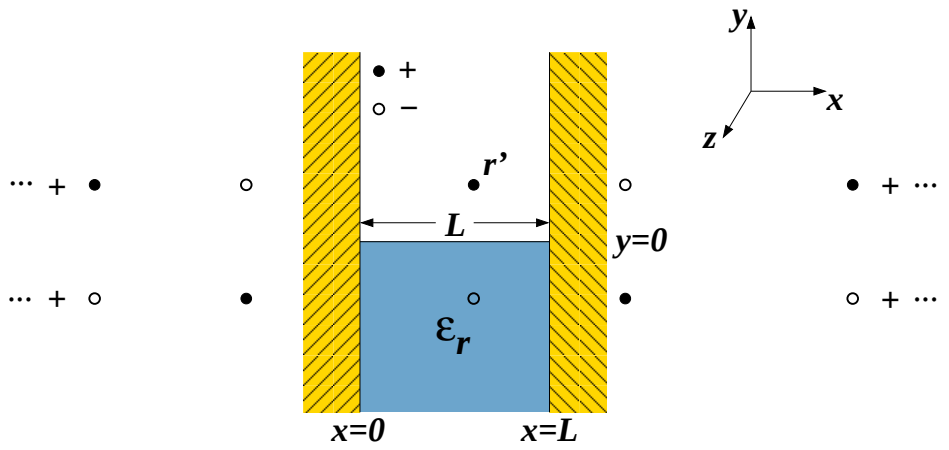

Figure 3.1: Simplified junction geometry for which an analytic solution to the electrostatic Green's function G can be obtained. The junction consists of two infinite metal surfaces modeling the source and drain electrodes and a material with dielectric constant ε_r filling the lower half of the spacing between them. The image charge solution in Eq. (3.16) is illustrated by the empty and filled circles.

be solved with $\varepsilon_r = 1$ everywhere. For a homogeneous dielectric the induced charge resides at the interface as a surface charge σ. The Green's function can therefore be obtained from the following Poisson equation

$$-\nabla^2 G(\mathbf{r}, \mathbf{r}') = 4\pi \left[\delta(\mathbf{r} - \mathbf{r}') + \sigma(\mathbf{r})\right], \tag{3.13}$$

where the surface charge is located in the xz-plane $\sigma(\mathbf{r}) = \sigma(x, z)\delta(y)$. The surface charge is given by the normal component of the polarization on the interface,

$$\sigma = \mathbf{P} \cdot \hat{\mathbf{n}} = (\varepsilon_r - 1)\, \mathbf{E} \cdot \hat{\mathbf{n}}. \tag{3.14}$$

Here the normal component (in this case the y-component) is evaluated immediately below the interface, i.e. $y = 0^-$. Expressing the electric field by the gradient of the Green's function, the following relation between the latter and the surface charge is obtained

$$-\hat{\mathbf{n}} \cdot \nabla G(\mathbf{r}, \mathbf{r}') = \frac{1}{\varepsilon_r - 1}\sigma(\mathbf{r}). \tag{3.15}$$

The Eqs. (3.13) and (3.15) can be solved for the surface charge and the

Green's function resulting in the following intuitive image charge solution

$$G(\mathbf{r},\mathbf{r}') = \sum_{\sigma=\pm1}\sum_{\tau=\pm1}\sigma\left(\frac{\varepsilon_r+\tau}{\varepsilon_r+1}\right)\tau\Bigg[\frac{1}{\sqrt{(x-\sigma x')^2+(y-\tau y')^2+(z-z')^2}} + \sum_{n=1}^{\infty}\Bigg(\frac{1}{\sqrt{(2nL-(x-\sigma x'))^2+(y-\tau y')^2+(z-z')^2}} + \frac{1}{\sqrt{(2nL+(x-\sigma x'))^2+(y-\tau y')^2+(z-z')^2}}\Bigg)\Bigg], \quad (3.16)$$

which is illustrated in Fig. 3.1. Here, L is the electrode spacing and the sums run over all repeated images of the point charge in $\mathbf{r}'$ in the metallic electrodes and the dielectric surfaces. The strength of the image charges is seen to be given by the factor $(\varepsilon_r+\tau)/(\varepsilon_r+1)$ in Eq. (3.16). This implies that the image charges located below the dielectric interface (corresponding to $\tau=-1$) have a strength of

$$q_{\varepsilon_r} = \frac{\varepsilon_r-1}{\varepsilon_r+1}. \quad (3.17)$$

This is also the image charge strength of an infinite surface with dielectric constant ε_r [62]. The strength of the remaining image charges ($\tau=1$) is unity corresponding to the screening from a metallic surface.

By leaving out the contribution from the point charge itself in Eq. (3.16), only the induced potential $\widetilde{G}$ in Eq. (3.10) remains. The analytic solution therefore provides a mean of obtaining the image charge mediated self-interaction $\widetilde{V}$ of an electron in Eq. (2.20).

3.3 Finite Element Method

The finite element method (FEM) is a widely used method for the solution of boundary value problems in various disciplines of science and engineering. One of its major strengths is its ability to handle solution domains with complex shapes. This is accomplished by decomposing the solution domain into a set of discrete sub-domains referred to as elements which together define the so-called mesh. Fig. 3.2 illustrates such a mesh for the single-molecule junction studied in the present work. The nonuniform mesh allows for the use of a coarse discretization in the regions close to the boundaries of the solution domain where the potential is smooth. As a consequence, the errors introduced by the non-physical boundaries of a finite solution domain can be minimized using a large simulation cell. In the present work the open source FEM code from the FEniCS project [65] has been used.

In general, the boundary value problem for Poisson's equation in the solution domain Ω defined by the junction geometry can be formulated as

$$-\nabla \cdot [\varepsilon_r \nabla u] = f, \quad \mathbf{r} \in \Omega \tag{3.18}$$

$$u = g, \quad \mathbf{r} \in \partial\Omega_{\mathrm{D}} \tag{3.19}$$

$$\hat{\mathbf{n}} \cdot \nabla u = h, \quad \mathbf{r} \in \partial\Omega_{\mathrm{N}} \tag{3.20}$$

In the more general notation introduced here, u denotes the electrostatic potential, $f = 4\pi\rho$ is the source term, and g and h are scalar functions specifying the value of the potential and its normal derivative on the Dirichlet and Neumann parts of the boundary, respectively.

Instead of the differential form above, the finite element method takes its starting point in the variational formulation of the boundary value problem. To rewrite the differential boundary value problem to its variational form, Eq. (3.18) is multiplied with an arbitrary test function v belonging to the function space V in which the solution is sought. Subsequently, the equation is integrated over the solution domain Ω and using integration by parts the variational form follows

$$\int_\Omega d\mathbf{r}\, \varepsilon_r \nabla v \cdot \nabla u = \int_\Omega d\mathbf{r}\, v f + \int_{\partial\Omega} dS\, \varepsilon_r v \left(\hat{\mathbf{n}} \cdot \nabla\right) u. \tag{3.21}$$

The boundary integral on the right-hand side is handled by inserting the Neumann boundary condition from equation (3.20). The fact that only first order derivatives appears, ensures that the variational formulation is well-defined as long as v and u are continuous piecewise differentiable functions. Since such functions do not have continuous first derivatives as required by the differential form of Poisson's equation, the variational formulation is also referred to as the weak form and its solution a weak solution. Introducing the bilinear form

$$a(v, u) = \int_\Omega d\mathbf{r}\, \varepsilon_r \nabla v \cdot \nabla u \tag{3.22}$$

and linear form

$$b(v) = \int_\Omega d\mathbf{r}\, v f \tag{3.23}$$

on V, then for u to be a solution

$$a(v, u) = b(v) \quad \forall v \in V. \tag{3.24}$$

From the variational form of the boundary value problem, the next step is the discretization in the finite element space which is composed of basis

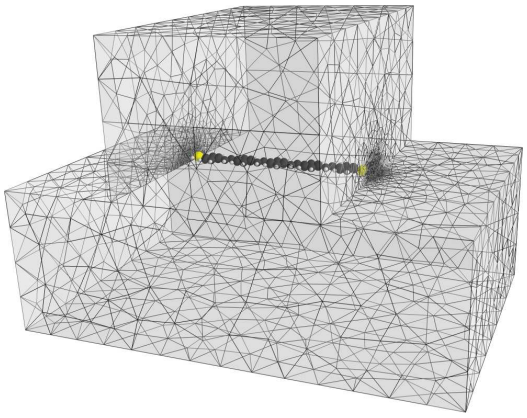

Figure 3.2: Boundary mesh of the 3-dimensional simulation cell for a single-molecule junction. The nonuniform mesh allows to obtain an accurate representation of the potential in the relevant region near the molecule while at the same time minimizing the errors due to non-physical boundaries by using a large simulation cell.

functions ϕ_i with compact support. The most simple basis is the linear basis function which for each node (element vertex) of the mesh connects to the neighboring nodes with a linear function with value one at the node itself and zero at the neighboring nodes (hence the compact support). In the finite element basis the solution u is expanded as

$$u = \sum_i u_i \phi_i \tag{3.25}$$

where $\{\phi_i\}_{i=1}^N$ is the global basis of the finite element space. The expansion is then substituted into the weak formulation and the test function v is chosen to coincide with a basis function ϕ_i. This particular approach is often referred to as Galerkin finite element discretization. The resulting algebraic system can be written in matrix form as

$$\mathbf{Ku} = \mathbf{f} \tag{3.26}$$

where $\mathbf{u}$ is a vector holding the expansion coefficients in Eq. (3.25), $K_{ij} = a(\phi_i, \phi_j)$ and the elements of the right-hand side are given by $f_i = b(\phi_i)$ where a and b are the bilinear and linear forms defined above in Eqs. (3.22) and (3.23). The assembly and the solution of the matrix equation in Eq. (3.26) are the time-consuming parts of a FEM calculations. Depending on the size N of the linear system it can be tackled with either direct or iterative methods [66].

Chapter 4

Characterization of an OPV5 SET

Single-molecule SETs based on the conjugated oligo-phenylene vinylene (OPVs) molecules have been subject to a number of studies over the recent years [20, 36, 49, 50]. The experiment published in Ref. [20] was the first to report access to several charge states of a molecule in a single-molecule SET. The measured stability diagram (see Fig. 1.9) showed diamonds of varying size. This serves as a fingerprint of the quantization of the molecular levels. Interestingly, the gap of the OPV5 molecule extracted from the stability diagram was strongly reduced ($\sim$ 300 meV) compared to its value in electrochemical experiments ($\sim$ 2.5 eV). This effect, which has been observed consistently for various single-molecules SETs, been ascribed to image charges in the metallic electrodes [58]. So far, however, no satisfactory explanation of the effect in single-molecule SETs has been given. As the image charge effect is strongly dependent on the geometry of the junction and the position of the molecule in the junction, a quantitative estimate requires a 3-dimensional simulation of the junction combined with an atomic description of the molecule.

To date, only a few theoretical studies of single-molecule SETs based on an atomic description of the molecule and a realistic junction geometry have been reported in the literature. They have focused on the vibrational properties of the OPV5 molecule in the junction [67] and image charge effects in a simplified junction geometries [58, 60]. The purpose of the present chapter is to study the effect of image charges/junction polarization in a realistic OPV5-based single-molecule junctions with the formalism developed in Chap. 4. Furthermore, some general aspects such as the gate coupling to the molecule and the effect of a finite source-drain voltage will be addressed.

4.1 OPV5 SET

The simulated OPV5 SET is illustrated in Fig. 4.1. It has the molecule stretched out between the source and drain electrodes which are separated by a $\sim$ 3.2 nm gap. Without the molecule, the junction is taken to be translation invariant in the direction parallel to the electrode edges. In order to resemble the experimental settings [20], the molecule is separated from the gate electrode by a 5 nm thick gate dielectric with dielectric constant $\varepsilon_r = 10$. This corresponds to the high-κ dielectric Al_2O_3 [2]. The relatively high dielectric constant of the gate dielectric ensures a reasonable capacitive coupling between the gate and the molecule. The source and drain electrodes in Fig. 4.1 have been cutoff in the vertical direction for visual reasons. In the numerical simulations they are modelled by infinitely high metal blocks with potentials given by the applied voltages. The molecule is positioned flat on top of the gate dielectric with a distance of 1 Å to the surfaces of the source/drain electrodes and the gate dielectric. With the electrostatic image plane located outside the atomic surfaces [68, 69], this effectively corresponds to a distance on the order of a van der Waals distance ($\sim$ 3 Å) between the molecule and the surface atoms.

The molecular structure of the OPV5 molecule is shown in the right side of Fig. 4.1 together with the HOMO and LUMO orbitals. To resemble the molecule used in experiments [20], a thiol group (SH) is attached to the terminating phenylene units. The thiol group localizes the HOMO on the terminating phenylene unit. Furthermore, it donates electrons the π-system on the carbon backbone of the molecule, which result in a net positive charge of the thiol group. In all calculations presented in the following the molecule

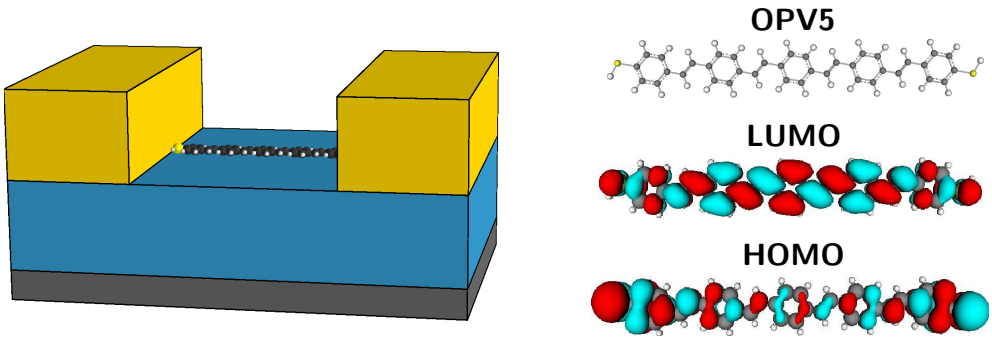

Figure 4.1: OPV5-SET and molecular orbitals. (left) Geometry of the simulated OPV5-SET. The OPV5 molecule is stretched out between the electrodes which are separated by $\sim$ 3.2 nm. (right) Structure and HOMO/LUMO orbitals of the thiol-terminated OPV5 molecule.

will be considered in neutral state geometry.

In this chapter the positions of the molecular levels are studied as a function of different junction properties and applied voltages to the source, drain and gate electrodes. For this purpose the total energy is evaluated for the different charge states of the molecule, i.e. with varying number of electrons on the molecule. The molecular ionization potential (IP) and electron affinity (EA) are given by the difference in total energy between the neutral and singly charged states of the molecule, i.e.

$$\mathrm{IP} = E^{N-1} - E^{N} \quad \text{and} \quad \mathrm{EA} = E^{N} - E^{N+1}. \tag{4.1}$$

Here, N denotes the number of electrons in the neutral state of the molecule. The charged states with one electron added $(N+1)$ and removed $(N-1)$, correspond to the anion and cation, respectively. The molecular gap is given by the difference between the ionization potential and electron affinity,

$$E_{\mathrm{gap}} = \mathrm{IP} - \mathrm{EA} = E^{N-1} + E^{N+1} - 2E^{N}. \tag{4.2}$$

In the following the effect of junction polarization is quantified in terms of the polarization energy P which gives the reduction of the gap relative to its gas phase (g) value, i.e. $E_{\mathrm{gap}} = E_{\mathrm{gap}}(g) - P$. It can be regarded as a sum of the polarization energies of the negatively and positively charged states of the molecule, $P = P_{+} + P_{-}$ (see Fig. 1.7). The physical interpretation of the polarization energies $P_{+/-}$ is that they give the total gain in energy upon introducing the charged molecule in the junction.

In the present work a self-consistent Hückel implementation of the effective junction Hamiltonian in Eq. (2.23) is used to calculate the total energies. The details of the Hückel implementation is outlined in App. B. It should be noted that the self-consistent Hückel method underestimates the molecular gaps as compared to DFT. However, since the change in the gap due to the interaction with the polarization charge is relatively independent on the size of the gap, this should not have any significant influence on the conclusions drawn here.

4.2 Polarization effects

The present section studies the effect of junction polarization in the absence of applied voltages. The polarization of the junction is illustrated in Fig. 4.2 which shows contour plots of the induced potential Φ_{ind} for the neutral molecule and the negatively charged anion. From the induced potential it is clear that the negative charge of the anion results in a significant

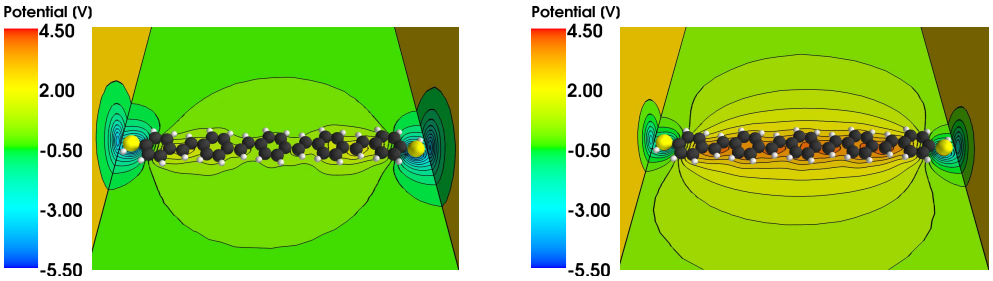

Figure 4.2: Illustration of the polarization response of the junction showing contour plots of the induced potential Φ_{ind} at the surfaces of the electrodes and gate dielectric. (left) Neutral OPV5 molecule. (right) Negatively charged anion.

polarization of the junction. The polarization due to the neutral molecule is less pronounced. However, the positively charged thiol groups induces a negative potential in their vicinity which results in an increased polarization of the molecule during the self-consistent cycle of the electronic structure calculation. The junction polarization must therefore be expected to affect both the neutral and charged state of the molecule.

In order to address the size of the polarization effects for different molecule sizes and electrode spacing, the analysis has been carried out for the molecules OPV2 to OPV5. The geometry of the different junctions is equivalent to the one for OPV5 in Fig. 4.1 with the molecule stretched out between the electrodes and the electrode spacing adjusted accordingly. Tab. 4.1 summarizes the calculated gaps for the following three cases (i) gas phase, (ii) OPV-SET, and (iii) molecule placed between two parallel metal surfaces with the same spacing as the source and drain electrodes in the SET. The polarization energies due to the presence of the junction environments are seen to result in significant reductions of the molecular gaps relative to their gas phase values.

For further analysis, it is instructive to use the following simplified interpretation of the molecular gap: starting with two neutral molecules then the gap in Eq. (4.2) is the energy cost of transferring an electron from one molecule to the other. Since this process involves the promotion of an electron from the HOMO in one of the molecules to the LUMO in the other molecule, it is suggestive to write the molecular gap as the HOMO-LUMO gap of the neutral molecule, Δ_{HL}, plus two times the Coulomb energy, E_c, required to charge the molecule

$$E_{\text{gap}} = \Delta_{\text{HL}} + 2E_c. \tag{4.3}$$

It should be noted that this is equivalent to the expression for the addition energy of conventional quantum dots SETs when the size quantization of the

	Gas phase		SET			Surfaces		
	E_{gap}	Δ_{HL}	E_{gap}	Δ_{HL}	P	E_{gap}	Δ_{HL}	P
OPV2	4.84	1.64	1.28	1.10	3.56	2.95	1.55	1.89
OPV3	4.01	1.34	0.90	0.75	3.11	2.49	1.22	1.52
OPV4	3.56	1.20	0.75	0.60	2.81	2.24	1.04	1.32
OPV5	3.27	1.12	0.68	0.53	2.59	2.08	0.92	1.19

Table 4.1: Calculated gaps, E_{gap}, single-particle HOMO-LUMO gaps, Δ_{HL}, and polarization energies, P, (all in eV) for thiol-terminated OPV molecules in the three environments: gas phase (isolated molecule), SET, and Surfaces (molecule placed in the gap between two infinite parallel metal surfaces).

dot is taken into account [27].

In a naive first guess one would expect the reduction of the gap to be mainly a consequence of screening of the charging energy E_c. However, the values listed in Tab. 4.1 show that also the HOMO-LUMO gaps are reduced in the environments. The origin of this reduction is illustrated in Fig. 4.2 for OPV5. The combination of the localization of the HOMO on the thiol groups and the negative induced potential in their vicinity, shifts the HOMO level to a higher energy. A similar reasoning for the negatively charged carbon backbone and the LUMO leads to a lowering of the LUMO level and hence a closing of the HOMO-LUMO gap. The charging energy obtained from Eq. (4.3) is for OPV5 in gas phase $E_c = 1.08$ eV. The screening response of the junction, which is shown for the OPV5 anion in Fig. 4.2, reduces this value considerably to $E_c = 75$ meV. To summarize, the reduction of the gap can be understood as a consequence of two parallel effects: (i) a reduction of the HOMO-LUMO gap and (ii) screening of the Coulomb repulsion on the molecule which lowers the charging energy.

Returning to Tab. 4.1, the polarization energy is seen to increase with decreasing molecule size. Since the reduction of the HOMO-LUMO gap is similar for all the molecules, this trend must be related to the Coulomb interaction between the molecules and their polarization charge. For the junctions considered here two things play a role in this respect. First of all, the extend of the polarization charge in the dielectric is to a good approximation given by the size of the molecule. Since the Coulomb energy associated with the interaction between two charge distributions increases with their degree of localization (assuming that their center distances are kept fixed), the smaller molecules interact more strongly with their polarization charge. Secondly,

with the electrode spacing given by the length of the molecules, the average distance between the polarization charge in the electrodes and the molecular charge increases with decreasing molecule size. As above this results in a higher Coulomb energy and hence also a larger polarization energy. The latter effect is clearly demonstrated by the last column in Tab. 4.1 where the dielectric is absent. The polarization energy for the shortest molecule OPV2 is 0.7 eV larger than the one for OPV5. In the SET geometry this difference is 0.97 eV, indicating that the latter effect dominates the increase of the polarization energy for the smaller molecules.

In the following the different contributions to the polarization energy of OPV5 in the SET environment will be discussed. Due to its relatively high dielectric constant, the gate dielectric must be expected to have a large influence on the polarization energy. For example, assuming that the gate dielectric is equivalent to an infinite dielectric surface, the image charge strength is given by $q_{\varepsilon_r} = (\varepsilon_r - 1)/(\varepsilon_r + 1)$. For $\varepsilon_r = 10$ this results in an image charge strength of almost unity corresponding to metallic screening properties. The important role of the gate dielectric is clearly demonstrated by the large difference between the polarization energies for the SET and Surfaces environments in Tab. 4.1. For OPV5 the value for the latter of 1.19 eV is less than half the value for the SET environment which is 2.59 eV. The reduction of the molecular gap in the OPV5 SET has thus equivalent contributions from the source/drain electrodes and the gate dielectric. Note, however, that the contribution from the gate dielectric is highly dependent on its dielectric constant. With a dielectric constant of $\varepsilon_r = 3.9$ corresponding to SiO_2 the polarization energy for OPV5 was reduced to 2.11 eV.

The contribution from the gate electrode was found to be negligible. The reason for this is twofold. First, the dielectric screens the molecular charge. Therefore the net charge seen by the gate electrode is $q - q_{\varepsilon_r}$ and not the bare charge of the molecule. Second, due to the relatively large distance between the gate electrode and the molecule the Coulomb interaction with the polarization charge in the gate is small. A simple image charge estimate shows that the thickness of the gate dielectric must be ~ 1 nm in order to see a contribution of ~ 0.1 eV to the polarization energy from the gate electrode.

4.3 Gate coupling

The gate electrode and its capacitive coupling to the molecule is fundamental for the functionality of single-molecule SETs. It allows to shift the molecular levels by simple electrostatic means and thereby turn the current on and off. The following section addresses the gate coupling in the OPV5 SET and its

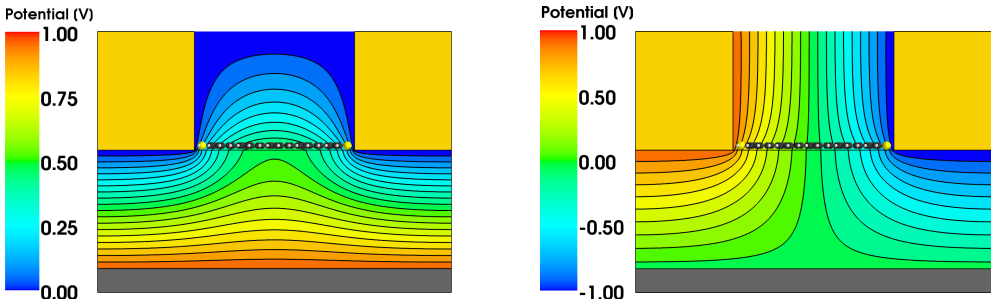

Figure 4.3: Spatial profiles of the electrostatic junction potential. (left) 1 V applied to the gate electrode. (right) ±1 V applied to the left and right electrodes, respectively. The thickness of the gate dielectric has here been set to 2.5 nm for visual reasons.

dependence on the thickness and dielectric constant of the gate oxide.

The small size of the gap between the source and drain electrodes in single-molecules SETs makes it hard to modulate the position of the molecular levels with a gate electrode. Screening in the source and drain electrodes drastically reduces the value of the gate potential in the gap. This effect is demonstrated in the left hand side plot of Fig. 4.3 which shows the spatial profile of an applied gate voltage in the OPV5 SET. Apart from reducing the gate potential, the screening by the electrodes also results in a gate potential that varies significantly over the extend of the molecule. With the HOMO located at the thiol groups close to the electrodes and the LUMO on the carbon backbone of the OPV5 molecule, the gate coupling to the different charge states of the molecule must therefore be expected to differ. This is in contrast to conventional quantum dot SETs where the gate coupling to a good approximation can be assumed to be independent on the charge on the dot [27].

When an voltage V_g is applied to the gate electrode the resulting shift of the molecular ionization potential and electron affinity is given by the corresponding changes in the total energies in Eq. (4.1). In an effective single-particle description as e.g. Hartree-Fock or the semi-empirical approach used in the present work, the total energy must be determined self-consistently as a function of the gate potential for each of the charge states. However, under the assumption that the self-consistent changes in the electron density can be neglected, the situation simplifies considerably. This essentially means that the polarization of the molecule due to perturbations is neglected. With this approximation the shift of the molecular ionization energy and electron affinity can be expressed by

$$\Delta E_{\mathrm{IP/EA}} = V_g \cdot \alpha_n, \tag{4.4}$$

where α_n is the gate coupling to the molecular orbital n from which the electron is added or removed. With the assumption above the gate couplings can be obtain from the first order change $\Delta\varepsilon_i$ in the molecular single-particle levels,

$$\alpha_n \approx \Delta\varepsilon_n = \langle n|\alpha_{\mathrm{g}}(\mathbf{r})|n\rangle. \tag{4.5}$$

Here α_{g} is the characteristic potential that results from applying a unit voltage to the gate electrode.

In the following the gate couplings to the HOMO and LUMO, and thereby also the shift of the IP and EA with an applied gate voltage, are considered. Their dependence on the thickness and the dielectric constant of the gate dielectric is shown on the left and right plots of Fig. 4.4, respectively. Furthermore, the line denoted Mean shows the average of the gate couplings to the atomic sites of the molecule.

As expected, the gate couplings to the HOMO and LUMO orbitals differ markedly with the latter being approximately twice as large as the former. The mean gate coupling to the atomic sites of the molecules is close to the LUMO gate coupling. This can be attributed to the fact that the LUMO is distributed more uniformly on the molecule as compared to the HOMO (see Fig. 4.1).

The left plot clearly shows the effect of using a thin dielectric layer. A significant increase in the gate coupling can be obtained by decreasing the layer thickness to a few namometers. From a practical point of view this is however not as straight forward as it sounds since varying material properties and leakage currents to the gate electrode play an important role for ultrathin oxide layers [2].

Alternatively, a higher dielectric constant of the gate oxide can help to increase the gate coupling. However, as the right plot shows, increasing the dielectric constant beyond ~ 10 does not result in any significant increase of the gate coupling. The saturation of the gate coupling is due to screening in the metallic source and drain electrodes. The same screening is responsible for a decreasing gate coupling when the molecule is elevated from the dielectric surface. This effect is illustrated by the spatial profile of the gate potential in Fig. 4.3 which decreases rapidly as a function of the distance to the gate dielectric.

Similar conclusions as the above have been drawn in a recent theoretical study on gate coupling in nanoscale junctions [70]. This work also studied the effect of changing the geometry of the source and drain electrodes. A junction with tapered electrodes having a triangular shape was found to have a substantially greater gate coupling than the one with infinite electrodes considered in the present work. This, in particular, when the molecule was

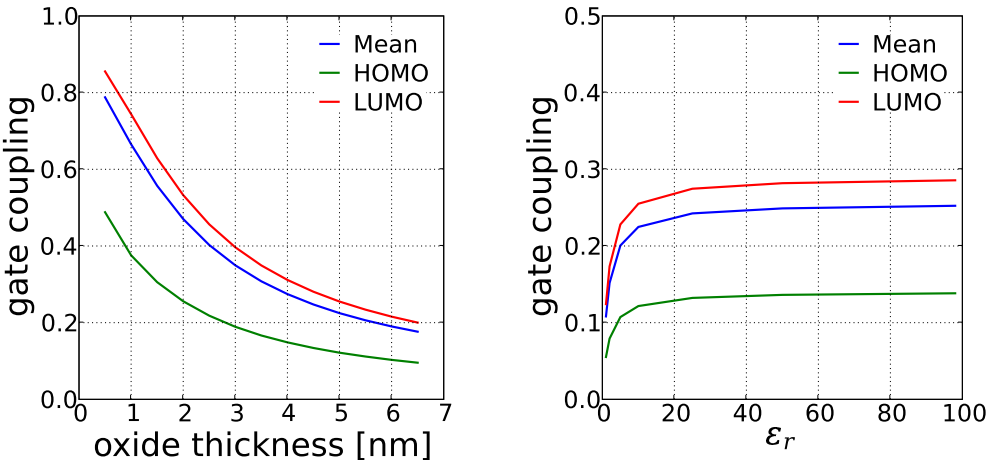

Figure 4.4: Gate couplings α_n to the HOMO and LUMO orbitals in the OPV5 SET. The line denoted Mean is the average of the gate couplings on the atomic positions of the OPV5 molecule. (left) Gate coupling as a function of gate oxide thickness with $\varepsilon_r = 10$. (right) Gate coupling as a function of the dielectric constant ε_r with an oxide thickness of 5 nm.

elevated from the surface of the gate dielectric. The screening effect due to the electrode geometry is therefore another significant parameter in determining the gate coupling of a nanoscale junction.

4.4 Stability diagram

The charge stability diagram for the OPV5 SET has been calculated by evaluating total energies of the neutral, singly charged and doubly charged molecule as a function of gate and source-drain voltage. The assumption that the molecule remains chemically stable in the considered charge states is in agreement with experimental findings [20, 49]. The Fermi energy of the metallic source and drain electrodes is treated as a parameter and placed in the gap between the ionization potential and the electron affinity. The resulting stability diagram is depicted in Fig. 4.5 where the colour indicates the number of levels that are located in the bias window. The source-drain bias has been applied symmetrically to the electrodes as illustrated in the right plot of Fig. 4.3 for $V_{\mathrm{sd}} = 2\,V$. It should be noted that the voltage drop across the junction is non-linear close to the dielectric interface where the majority of the drop occurs close to the electrodes.

Like the experimentally observed stability diagram [20], the calculated diagram is characterized by a big central diamond corresponding to the neutral

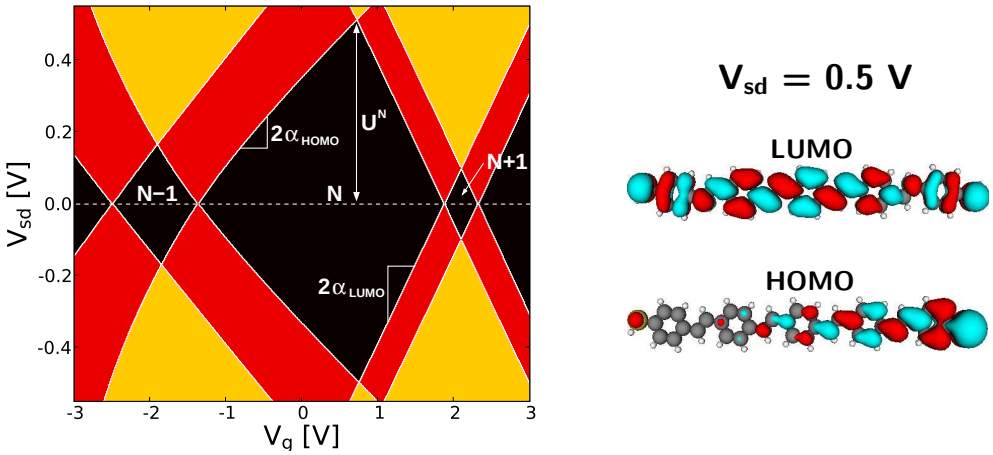

Figure 4.5: Stability diagram and molecular orbitals at finite bias. (left) Calculated charge stability diagram for the OPV5-SET. The color indicates the number of levels located inside the bias window (black: 0, red: 1, yellow: 2) (right) Molecular orbitals of the OPV5 molecule at $V_{\mathrm{sd}} = 0.5$ V. The non-linear diamond edges on the left site of the central diamond is a consequence of the localization of the HOMO at the right electrode.

state of the molecule surrounded by two small diamonds corresponding to the positively and negatively charged molecule. Since only the ground states of the neutral and charged molecule are considered, the stability diagram contains no lines due to excited states of the molecule. This could e.g. be vibrational excitations which have been observed experimentally with energies ranging from a few meV to ~ 100 meV. A recent theoretical study has shown that some of the vibrational excitations are expected to involve the gold atoms to which the molecule binds [67]. Electronic excitations of the OPV5 molecule with electrons/holes occupying higher/lower molecular orbitals have energies on the order of the single-particle level spacings (~ 100 meV). These are therefore harder to observe experimentally.

The addition energy given by the height of the central diamond is equal to the gap of the molecule under finite bias conditions. Compared to the zero bias gap of 0.68 eV from Tab. 4.1 a substantial decrease of the gap under finite bias is found. From Fig. 4.5 a value of ~ 0.50 eV is read off. The lower value of the addition energy stems from the non-linear edges on the left side of the central diamond which indicates that the single-particle levels are bias independent. Indeed, it was found that HOMO localizes at the negatively biased electrode as illustrated in Fig. 4.5. As a consequence, the HOMO level moves upwards with the applied source-drain voltage making the state with only one electron in the HOMO energetically favourable compared to the

neutral state which has a doubly occupied HOMO. The fact that the energy of the neutral molecule increases more than the energy of the cation as a function of the source-drain bias, reduces the ionization energy and hence also the threshold for pulling out an electron from the molecule. With a source-drain voltage of $V_{\rm sd} = 0.5$ V corresponding to the top of the central diamond in Fig. 4.5, the shift of the HOMO level was ~ 0.15 eV, in good agreement with the discrepancy between the zero bias and finite bias gaps discussed above.

The height of the two smaller diamonds correspond to the addition energies of the positively and negatively charged cation and anion, respectively. For these states the addition energy is given by the difference between the first and second ionization potential/electron affinity. In terms of total energies this is

$$E_{\rm add}^{N\pm1} = E^N + E^{N\pm2} - 2E^{N\pm1}. \tag{4.6}$$

The small addition energies associated with these states is due to their half filled frontier orbitals. Therefore, only the charging energy in Eq. (4.3) contributes when adding/removing an electron to/from the anion/cation. The resulting charging energies are ~ 50 meV and ~ 85 meV, respectively. The difference in charging energies of the anion and cation is a consequence of the different spatial distributions of the HOMO and LUMO.

As expected from the considerations in the previous section the gate couplings to the ionization potential and electron affinity differ markedly. In Fig. 4.5 these are given by the left and right slopes of the central diamond edges, respectively. Similar variations in the gate couplings have also been observed in a recent experiment [49]. The slopes of the diamond edges in Fig. 4.5 agree well with the calculated gate couplings in Fig. 4.4, where we read off the values $\alpha_{\rm HOMO} \sim 0.12$ and $\alpha_{\rm LUMO} \sim 0.25$ for an oxide thickness of 5 nm. This is also in good agreement with the value ~ 0.2 reported experimentally [20]. Often, the exact position of the molecule in experiments is relatively unknown. However, the good agreement between the gate couplings suggests that the molecule also in the experiment is positioned directly on the gate oxide.

4.5 Conclusion and outlook

In conclusion, the present chapter has demonstrated that polarization plays an important role in single-molecule SETs. For the junction considered here, a gap renormalization of ~ 2.6 eV was found for the OPV5 molecule. The renormalization could be attributed to both a reduction of the HOMO-LUMO gap and a reduction of the Coulomb interaction. It should be noted

that the semi-empirical method applied in the present work, leaves some uncertainty on the calculated gap of 680 meV for OPV5 in the junction. As mentioned, this is likely to be an underestimation. Nevertheless, the experimentally reported value of ~ 300 meV is considerably lower than this. Different effects not considered in the present work can help to explain this discrepancy. For example, the formation of polarons upon charging of the molecule is known to result in relaxation energies on the order of $\sim 200 - 300$ meV for OPV-molecules [71]. Furthermore, a larger polarization energy is obtained if the molecule is positioned closer to the metallic electrodes where the screening is more pronounced. Taking into account these additional effects, the observed gap of ~ 300 meV might not seem that unlikely after all.

In order to address the effect of junction polarization on electronic and spin excitations of the molecule, model Hamiltonians based on the effective many-body Hamiltonian in Eq. (2.20) must be developed. The Pariser-Parr-Pople Hamiltonian, which is considered in Chap. 6 in a different context (see Eq. 6.3), is an example of a simple model Hamiltonian description for conjugated molecules. Here, the Hamiltonian is expressed in a basis of p_z orbitals localized on each carbon atom in molecule. Taking into account the screening of the Coulomb interaction in Eq. (2.20) leads to a renormalization of the Coulomb matrix elements in the Pariser-Parr-Pople Hamiltonian and a modification of the onsite energies of the p_z orbitals. Since an exact treatment of the Pariser-Parr-Pople Hamiltonian is limited to models with relative few basis orbitals, models using the molecular orbitals of the molecular subunits as basis orbitals have been developed [72]. The impact of junction screening on the molecular excitations of such model Hamiltonians is subject for further studies. With the inclusion of image charge effects at the level of the basis functions, it can be addressed to which extend the picture of image charge stabilized states in Ref. [49] is correct.

Chapter 5

Surface polarization and the GW approximation

Understanding the electronic structure of metal-molecule interfaces is a fundamental challenge in molecule-based electronics. The electronic transport properties of a metal-molecule interface are determined by the alignment between the molecular levels and the Fermi energy of the metal substrate. Factors like hybridization with the metal substrate, dipole formation at the interface as well as the polarization of the substrate in response to charge carriers on the molecule play an important role in this respect [73]. It has been demonstrated by several experiments that study the electronic structure of individual molecules, self-assembled monolayers and organic thin films on metal surfaces using photoemission techniques and scanning tunneling spectroscopy, that the molecular electronic structure is modified at the interface [16, 43, 74, 75].

Due to the hybridization with the metal substrate, first-principles studies of the interface are based on an atomic description of both the molecule and the metal. The electronic structure is most often obtained within the framework of density functional theory (DFT). In this context the eigenvalues of the effective single-particle Kohn-Sham Hamiltonian are interpreted as excitation energies. As DFT is a ground state theory this interpretation is questionable. In particular, the intriguing many-body effects associated with the polarization of the metal substrate and its effect on molecular levels are completely missing from DFT as well as other mean-field descriptions.

Recently, theoretical studies of single molecules physisorbed on metallic and dielectric surfaces have demonstrated that the Green's function based GW method captures the dynamical screening effects from the surface polarization. As a consequence, the molecular gaps were reduced by several eV [76, 77, 78]. Similar effects have been observed in GW calculations on

a simple model Hamiltonian for the interface [79]. Other GW studies of polarization effects at interfaces have demonstrated band-gap narrowing at metal-semiconductor interfaces [80, 81] and state localization in metal embedded semiconductor nanorods [82]. Also, the GW approximation have been demonstrated to describe the internal polarization of bulk polymer materials [83] and molecular self-assembled monolayers [84].

5.1 The GW approximation

The GW approximation originates from the so-called Hedin equations [85, 86] which form a closed set of equations for the many-body Green's function. Despite being formally exact, the complexity of the self-consistent framework provided by Hedin's equations necessitates the use of approximations in practical calculations. The simplest approximation to Hedin's equations is the GW approximation which neglects the so-called vertex corrections to the electronic self-energy.

In the GW approximation the electronic self-energy Σ is given by the product of the Green's function G and the dynamically screened interaction W, and can be written symbolically as [1]

$$\Sigma(1,2) = iG(1,2)W(1,2), \tag{5.1}$$

where the short-hand notation $1 = (\mathbf{r}_1, t_1)$ has been introduced. The Green's function obeys the usual Dyson equation

$$G(1,2) = G_0(1,2) + \int d3d4\; G_0(1,3)\Sigma(3,4)G(4,2) \tag{5.2}$$

with G_0 denoting the Hartree Green's function. The screened interaction W is given by the Dyson-like equation

$$W(1,2) = V(1,2) + \int d3d4\; V(1,3)\Pi(3,4)W(4,2), \tag{5.3}$$

where V is the bare Coulomb interaction and

$$\Pi(1,2) = -iG(1,2)G(2,1) \tag{5.4}$$

[1] The equations given here are for the time ordered (zero temperature) Green's function

$$G(1,2) = -i\langle T[\psi(1)\psi^\dagger(2)]\rangle.$$

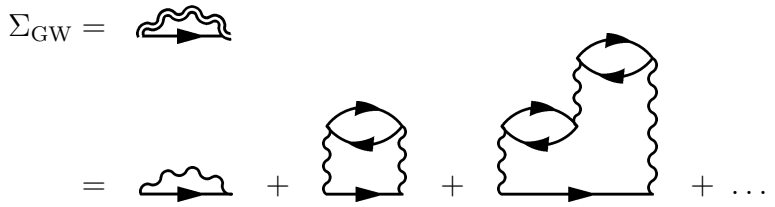

Figure 5.1: Diagrammatic representation of the GW self-energy. The single and double wavy lines denotes the bare (V) and the screened Coulomb interaction (W), respectively. The polarization function Π is represented by the bubble diagrams.

is the polarization function in the random-phase approximation (RPA) which contains the response of the system to an added hole or electron. The diagrammatic representation of the GW self-energy in Eq. (5.1) is illustrated in Fig. 5.1. It can be regarded as a generalization of the exchange potential $\Sigma_{\mathrm{x}} = iGV$ in Hartree-Fock (represented by the first diagram in the second equality) which does not take into account screening effects.

In fully self-consistent GW the set of coupled equations for Σ, G, Π, and W are solved iteratively until the Green's function has converged. However, due to the computational requirement of a fully self-consistent GW scheme, first-principles GW calculations are usually carried out non-selfconsistently. This approach, which is referred to as $\mathrm{G_0W_0}$, starts from an approximate G_0 from which a single self-energy iteration is carried out to obtain the final Green's function. In contrast to fully self-consistent GW, this has the disadvantage that the final result depends on the starting Green's function.

A self-consistent GW scheme has another advantage that it obeys the macroscopic conservation laws. For example, the conservation of particle number guaranteed by a self-consistent GW scheme means that the continuity equation

$$\partial_{t_1}\rho(1) + \nabla_1 \cdot \mathbf{j}(1) = 0 \tag{5.5}$$

is satisfied when the electronic charge density ρ and the current density is obtained from the self-consistent Green's function. This is due to Kadanoff and Baym [87, 88] who proved that an approximation for the self-energy Σ is conserving when it can be obtained as a functional derivative of a so-called Φ-functional with respect to G

$$\Sigma(1,2) = \frac{\delta\Phi[G]}{\delta G(1,2)}. \tag{5.6}$$

Such approximations to the self-energy are called Φ-derivable approximations. An extra bonus of this procedure for the self-energy is that the value for the total energy evaluated in terms of the self-consistent Green's function is independent of the method used to evaluate it. Apart from the GW approximation, other self-energy approximations of this type include the Hartree-Fock approximation, the second Born approximation and the T-matrix approximation [89].

As a final remark, it is noted that the RPA approximation to the polarization function Π does not represent a conserving approximation to the response function in the Baym-Kadanoff sense when evaluated with the self-consistent GW Green's function. This is substantiated by the fact that it violates the f-sum rule which must be fulfilled for a physical meaningful response function [90, 91]. Therefore, in a self-consistent GW scheme the polarization function Π must be regarded as an auxiliary quantity needed to construct the screened interaction.

5.2 The spectral function

Within a Green's function approach the charged excitations of a metal-molecule interface can be obtained from the spectral function (see App. C). The spectral function is given by the imaginary part of the (retarded) Green's function

$$A(\varepsilon) = -\frac{1}{\pi}\mathrm{Im}G(\varepsilon). \tag{5.7}$$

The quantities A and G are here assumed to be energy dependent matrices in a suitable set of basis functions $\{\phi_i\}$ where the i-index refers to a set of quantum numbers that characterizes the electronic excitations. The Green's function follows from the matrix inversion

$$G(\varepsilon) = [\varepsilon - H_0 - \Sigma(\varepsilon)]^{-1}, \tag{5.8}$$

where H_0 denotes the Hartree Hamiltonian. In general, the spectral function is a strongly peaked function with narrow main peaks at the quasi-particle energies $\varepsilon = \varepsilon_i$. The quasi-particle energies which correspond to well defined electron-like excitations coincide with the poles of the Green's function. In a diagonal approximation they are given by the real part of the self-energy via $\varepsilon_i = \varepsilon_0 + \mathrm{Re}\Sigma_i(\varepsilon_i)$. If the self-energy is expanded around the quasi-particles energies the spectral function takes the form of a Lorentzian

$$A_i(\varepsilon) = \frac{1}{\pi}\frac{Z_i\Gamma_i}{(\varepsilon - \varepsilon_i)^2 + \Gamma_i^2}, \tag{5.9}$$

where the width of the quasi-particle peak $\Gamma_i = Z_i \mathrm{Im}\Sigma_i(\varepsilon_i)$ corresponds to the inverse lifetime of the quasi-particle and

$$Z_i = \left[1 - \left.\frac{\partial \mathrm{Re}\Sigma_i}{\partial \varepsilon}\right|_{\varepsilon=\varepsilon_i}\right]^{-1} \leq 1 \tag{5.10}$$

is the spectral weight of the quasi-particle.

5.2.1 First-principles calculations

As mentioned in the introductory part of this chapter, first-principles calculations are often based on DFT. For the Green's function this amounts to approximating the non-local and energy dependent self-energy Σ by the local and energy independent exchange-correlation potential V_{xc}. In real-space notation this is

$$\Sigma(\mathbf{r}, \mathbf{r}', \varepsilon) = V_{\mathrm{xc}}(\mathbf{r})\delta(\mathbf{r} - \mathbf{r}'). \tag{5.11}$$

The corresponding Kohn-Sham (KS) DFT Green's function

$$G_{\mathrm{KS}}(\varepsilon) = [\varepsilon - H_0 - V_{\mathrm{xc}}]^{-1} \tag{5.12}$$

has poles at the eigenvalues $\varepsilon_i^{\mathrm{KS}}$ of the effective single-particle Kohn-Sham Hamiltonian. From a pragmatic point of view this assigns the meaning of the quasi-particle energies to the Kohn-Sham eigenvalues. From the variational derivation of DFT, there is, however, no reason why the Kohn-Sham eigenvalues should correspond to excitation energies. In particular, the exchange-correlation potential is constructed to give the correct ground state energy and not excitation energies. The so-called bandgap problem of DFT, i.e. the empirical fact that DFT systematically underestimates bandgaps of solids and molecules, is a consequence of this [92, 93].

In first-principles GW calculations, the quasi-particles energies are usually obtained in a perturbative manner from the eigenvalues of the Kohn-Sham Hamiltonian in DFT [94]. Based on the assumption that the Kohn-Sham eigenvalues $\varepsilon_i^{\mathrm{KS}}$ are good approximations to the quasi-particle energies, the GW quasi-particle energies can be obtained in first order perturbation theory as

$$\varepsilon_i = \varepsilon_i^{\mathrm{KS}} + Z_i \Delta\Sigma_i. \tag{5.13}$$

Here $\Delta\Sigma_i = \langle \phi_i^{\mathrm{KS}} | \Sigma(\varepsilon_i^{\mathrm{KS}}) - V_{\mathrm{xc}} | \phi_i^{\mathrm{KS}} \rangle$ is the matrix element of the difference between the GW self-energy and the exchange-correlation potential from the DFT calculation evaluated with the eigenfunction ϕ_i^{KS} of the Kohn-Sham Hamiltonian. This procedure for the calculation of the quasi-particle energies is in the spirit of $\mathrm{G_0W_0}$ approach with the self-energy calculated from the Kohn-Sham Green's function in Eq. (5.12).

5.3 Renormalization of molecular levels

The effect of surface polarization on molecular levels has recently been addressed in a number of studies based on first-principles GW calculations of molecules physisorbed on various metallic and dielectric surfaces [76, 77, 78]. With an atomic description of both the molecule and the surface these studies address the polarization effects from the surface from a microscopic point of view. This makes them complementary to the study of polarization effects in single-molecule junction presented in the previous chapter which was based on a macroscopic description of the junction.

For benzene physisorbed flat 3.25 Å above a metallic graphite surface the gap of the molecule was found to be ~ 3.2 eV smaller than the calculated gas phase value [76]. Due to the weak hybridization between the molecular orbitals and the surface states this reduction of the molecular gap was ascribed to the polarization of the surface. In contrast, the gap obtained from Kohn-Sham DFT eigenvalues did not show any change in the presence of the surface environment.

Fig. 5.2 illustrates the Feynmans diagrams from the GW self-energy that contributes to the renormalization of the molecular levels. The infinite sum of diagrams with the polarization bubbles located in the surface and the base line Green's function on the molecule represents the interaction between an electron added/removed to/from the molecule and the induced polarization charge of the surface. The response function given by the polarization bubbles contains the full dynamical response of the surface. In general, dynamical effects are only important when the life-time of the excitations on the molecule is comparable to the response time of the surface. For the weakly coupled benzene molecule this is not the case. Here, dynamical effects were found to make a negligible contribution to the level renormalization. As a consequence, the majority of the polarization induced shifts of the HOMO and LUMO levels of the benzene molecule could be accounted for by the static polarization integral

$$P_\nu = \frac{1}{2}\int d\mathbf{r}\int d\mathbf{r}'\ \phi_\nu(\mathbf{r})\phi_\nu^*(\mathbf{r}')\Delta W(\mathbf{r},\mathbf{r}')\phi_\nu(\mathbf{r}')\phi_\nu^*(\mathbf{r}), \tag{5.14}$$

where ϕ_ν is a molecular orbital of the isolated molecule and ΔW is the change in the screened interaction on the molecule due to the presence of the surface. The latter was approximated by the classical image potential from a metallic surface, $\Delta W(\mathbf{r},\mathbf{r}) = 1/2(z - z_0)$, where z_0 is the image plane position of the surface. The classical image potential has been shown to account for the static polarization response of a jellium surface [95]. For this metallic surface the image plane position was found to lie $0.5 - 0.9$ Å outside the surface.

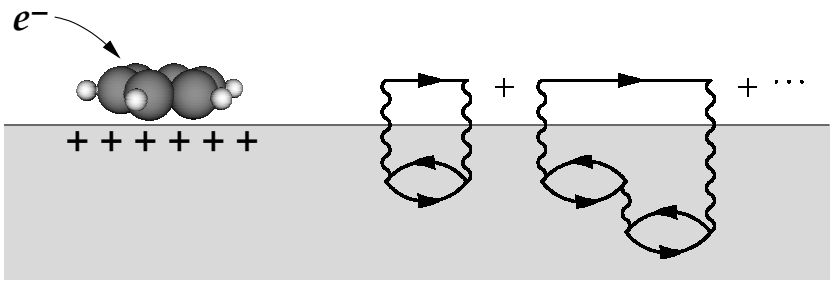

Figure 5.2: Physical picture and diagrammatic representation of the surface polarization and its interactions with the molecule. The infinite sum of Feynman diagrams with the polarization bubbles located in the surface gives the dynamical RPA response of the surface due to added/removed electrons on the molecule.

The resulting reduction of the gap is given by the sum of the polarization integrals for the HOMO and LUMO orbitals,

$$\Delta E_{\text{gap}} = P_{\text{HOMO}} + P_{\text{LUMO}}. \tag{5.15}$$

The polarization integral is equivalent to the polarization energies $P_{+/-}$ which were used to characterize the shifts of the molecular ionization potential and electron affinity in the previous chapter. Indeed, it has the same physical interpretation – it corresponds to the interaction between an electron in the molecular orbital ϕ_ν and its image charge in the surface.

The simplified description of the surface provided by the polarization integral in Eq. (5.14) has certain limitations. Since it is based on the orbitals for the isolated molecule it does not account for the polarization of the molecule in response to the surface polarization. For the symmetric case where the benzene molecule is physisorbed flat on the surface this effect is not important. However, if the benzene molecule is considered in an upright position with the molecule plane perpendicular to the surface, the part of the molecule which is closest to the surface will experience a stronger image potential as compared to the rest of the molecule. The resulting polarization of the molecule will cause a larger renormalization of the levels than expected from the polarization integral in Eq. (5.14) [59].

This is illustrates for the benzene/surface interface in Tab. 5.1. It lists the gap renormalizations for the flat and upright case as obtained with GW and the polarization integral P from Ref. [76]. Also listed, are the renormalizations obtained from total energy calculations of the gap in Eq. (4.1) using the Hückel implementation of the self-consistent framework in Sec. 2.2. For this purpose the classical image potential was used for the induced surface potential $V_{\text{ind}} = 1/2(z - z_0)$. In the calculations the distance between the

Position	SC Hückel	P	GW
Flat	2.84	2.93	3.2
Upright	2.10	1.93	2.41

Table 5.1: Calculated reductions of the molecular gap $E_{\text{gap}} = \text{EA} - \text{IP}$ for benzene on a metallic surface relative to its calculated gas phase value. The molecule is considered in a flat position and in an upright position on a metallic surface. For the two configurations the distance between the surface and the closest atom on the molecule was 3.25 Å and 2.21 Å, respectively. The first column is the gap reductions obtained with the self-consistent method of Sec. 2.2. The second and the third columns give the gap reductions resulting from the polarization integral P in Eq. (5.14) and GW calculations, respectively. Both of these have been taken from Ref. [76]. In the GW calculation the surface was described by an atomic graphite surface. For the two other cases a simple image charge potential was used to describe the polarization response of the surface. The position of the image plane is $z_0 = 1$ Å from the outermost atomic layer of the surface. For reference, the experimental gap phase gap for benzene is 10.42 eV.

molecule and the image plane of the surface was taken to be 2.25 Å for the flat case and 1.21 Å for the perpendicular case. This corresponds to an image plane position $z_0 = 1$ Å outside the atomic surface plane in agreement with Ref. [76].

For the flat case, the gap reductions from the total energy calculations and the polarization integral are in good agreement. This is to be expected since both results are based on a classical image potential description of the surface potential. The reduction obtained with GW is ~ 0.3 eV larger. A better agreement is obtained if the image plane of the surface is placed at $z_0 = 1.25$ Å outside the atomic surface. This yields a reduction of 3.12 eV with the self-consistent method. The gap is thus very sensitive to the distance between the molecule and the image plane implying that an accurate value for the latter is important. For atomic surfaces the image plane position must be determined in a separate calculation [68].

With the molecule is placed in an upright position on the surface the good agreement between the gap reduction from the self-consistent method of the present work and the polarization integral is lost. In contrast to the flat case, the self-consistent method here gives the largest reductions of the gap. This is a consequence of the polarization of the molecule which is not accounted for in the polarization integral P. In the self-consistent method the charge distribution of the charged molecule relaxes towards the surface where the

potential due to the oppositely charged image charges is lower. This lowers the total energy of the charged molecule, and in turn also the gap, more compared to the case where the molecular charge distribution is not allowed to relax. Again, a better agreement with the GW result is obtained with the position of the image plane equal to $z_0 = 1.25$ Å. This gives a gap reduction of 2.30 eV.

In the next chapter, the GW approximation is applied to study the molecular levels of isolated conjugated molecules described with a semi-empirical model Hamiltonian. This study is intended to address the quality of the GW spectral function for isolated systems.

Chapter 6

Assessment of the GW approximation for molecules

With the entry of nanoscience the use of the GW method for studying electronic structure has been extended to low-dimensional systems such as molecules, fullerenes, carbon nanotubes, graphene [96, 97, 98, 99, 100, 101, 102]. One strength of the GW method is that it accounts for the screening of the long range Coulomb interaction which is essential in finite systems. The metal-molecule interface discussed in the previous chapter is a good example of this. Here, the finite extended of the molecular orbitals results in a surface polarization which in turn screens the Coulomb interaction on the molecule when an electron is added or removed from the molecule.

As the range of systems to which the GW approximation is being applied continues to expand, critical investigations of the performance of GW for other systems than the crystalline solids become important. For example, with the application of GW to metal-molecule interfaces, knowledge on the performance of GW on isolated molecules is of relevance. Different first-principles works have reported that the GW values for the ionization potential and electron affinity of benzene are in good agreement with experimental values [76, 101]. A more systematic study is, however, still missing.

So far, benchmark studies of the GW approximation have focused on Hubbard models with local interactions [103, 104, 105, 106]. The general conclusion from these works is that the GW approximation works well for small interaction strengths but fails for larger interactions strength. The use of GW in systems with local interactions is in fact unfortunate because the importance of electronic screening, which is the main effect described by GW, is weak in comparison to correlation effects.

In the following chapter benchmark GW calculations for π-conjugated molecules based on the semi-empirical Pariser-Parr-Pople (PPP) model [107,

108, 109] are presented. By comparing with exact results a direct and unbiased estimate of the quality of the GW approximation in molecular systems is obtained.

6.1 Quasi-particle energies

The excitation spectrum of a system is contained in the spectral function which has the following Lehmann representation (see App. C)

$$A_i(\varepsilon) = \sum_n \left[|\langle \Psi_n^{N+1} | c_i^\dagger | \Psi_0^N \rangle|^2 \delta(\varepsilon - \varepsilon_n) + |\langle \Psi_n^{N-1} | c_i | \Psi_0^N \rangle|^2 \delta(\varepsilon - \varepsilon_n) \right]. \quad (6.1)$$

The peaks of the spectral function are positioned at the quasi-particle energies $\varepsilon_n = E_n^{N+1} - E_0^N$ and $\varepsilon_n = E_0^N - E_n^{N-1}$ corresponding to electronic addition and removal energies, respectively. Here E_n^N denotes the total energy of the N-electron excited state $|\Psi_n^N\rangle$ with N referring to the neutral state of the system. For molecules the first addition and the first removal energy, i.e. $n = 0$, corresponds to the electron affinity and the ionization potential. In Hartree-Fock theory Koopman's theorem [63] states that these are equal to the energies of the highest occupied orbital (HOMO) and lowest unoccupied molecular orbital (LUMO) of the Hartree-Fock Hamiltonian. In the remaining of this chapter the HOMO and LUMO abbreviations will be used to refer to the ionization potential and electron affinity also outside Hartree-Fock theory. When the ionization potential and electron affinity are obtained from Koopman's theorem, two important effects are neglected. One is the relaxation of the molecular orbitals when an electron is removed from or added to the molecule. The other is the correlation energy which by definition is omitted in Hartree-Fock theory. With the generalization of Koopman's theorem to excited states it is instructive to write the exact quasi-particle energies as the sum of the three contributions

$$\varepsilon_n = \varepsilon_n^{\mathrm{HF}} + \Delta_{\mathrm{relax}} + \Delta_{\mathrm{corr}}, \quad (6.2)$$

where $\varepsilon_n^{\mathrm{HF}}$ denotes the n'th eigenvalue of the single-particle Hartree-Fock Hamiltonian. The relaxation contribution is the correction that follows by calculating the quasi-particle energy from self-consistently determined Hartree-Fock energies of the neutral and the charged states $N \pm 1$. The last term Δ_{corr} is the remaining contribution from the correlation energy.

In extended systems the potential due to a single delocalized electron/hole decreases with the size of the system. Hence, in such systems there will be no or little relaxation of the states due to the addition/removal of an electron,

and the majority of the correction to the quasi-particle energy will come from the correlation part Δ_{corr}. In molecules, nanostructures, molecules at surfaces, and disordered systems with finite localization lengths, this is not the case. Here, the introduction of an additional electron or hole will lead to a relaxation of the single-particle orbitals corresponding to a screening of the additional charge. As a consequence, the relaxation correction Δ_{relax} to the quasi-particle energy cannot be neglected in such systems.

6.2 Pariser-Parr-Pople Hamiltonian

The Pariser-Parr-Pople (PPP) model is an effective π-electron description of conjugated molecules that includes electron-electron interactions explicitly. The PPP-Hamiltonian is given by

$$\begin{aligned} H = &\sum_i \varepsilon_i \hat{n}_i - \sum_{\langle ij\rangle\sigma} t_{ij} c^\dagger_{i\sigma} c_{j\sigma} \\ &+ \frac{1}{2}\sum_{i\neq j} V_{ij}(\hat{n}_i - Z_i)(\hat{n}_j - Z_j) + \sum_i U_i \hat{n}_{i\uparrow}\hat{n}_{i\downarrow}, \end{aligned} \tag{6.3}$$

where c_i ($c_i^\dagger$) creates (annihilates) an electron in the p_z orbital ϕ_i on atom i of the molecule, $\hat{n}_i = \hat{n}_{i\uparrow} + \hat{n}_{i\downarrow}$ is the number operator, $\hat{n}_{i\sigma} = c^\dagger_{i\sigma} c_{i\sigma}$, Z_i is the valence (i.e. the number of π-electrons) of atom i, and $\langle ij\rangle$ denotes nearest neighbor hopping. In the interacting part of the Hamiltonian only the direct matrix elements of the Coulomb interaction

$$V_{ij} = \int d\mathbf{r} \int d\mathbf{r}'\ \phi_i(\mathbf{r})\phi_i^*(\mathbf{r}) V_C(\mathbf{r}-\mathbf{r}')\phi_j(\mathbf{r}')\phi_j^*(\mathbf{r}') \tag{6.4}$$

are included. This is only a good approximation when the basis orbitals are localized as is the case here. As the PPP-model only treats the π-electrons explicitly, the screening effects from the σ-electrons are usually included within a semi-empirical parametrization for the matrix elements of the Coulomb interaction in Eq. (6.4). A common approximation for the long ranged Coulomb interactions is the Ohno parametrization [110]

$$V_{ij} = \frac{14.397}{\sqrt{(28.794/(U_i+U_j))^2 + R_{ij}^2}}\ , \tag{6.5}$$

where R_{ij} is the inter-atomic distance (in Å) and U_i is the onsite Coulomb interaction (in eV). For large distances the Ohno parametrization recovers the $1/r$ behavior of the Coulomb interaction while it for small distances

Thiophene			Pyridine			Benzene			Biphenyl/OPV2	
ε_S	t_S	U_S	ε_N	t_N	U_N	ε	t	U	t_s	t_d
-7.8	-3.0	5.0	-3.0	-2.05	12.06	0	-2.539	10.06	-2.22	-2.684

Table 6.1: PPP-parameters (in eV) for the molecules studied in the present work. For thiophene and pyridine only the parameters for the heteroatoms (S and N) are listed. Except for the transfer integral (see Eq. (6.6)), the C parameters for these two molecules are identical to the parameters for benzene. The benzene parameters have also been used for the conjugated parts of biphenyl, OPV2, naphthalene and anthracene. For biphenyl and OPV2 t_s and t_d denote the transfer integrals for the single and double bonds.

represents a screened interaction that interpolates to the onsite Coulomb interaction U_i for $R_{ij} = 0$. The onsite energy ε_i, the hopping element t_{ij} and the onsite Coulomb interaction U_i are treated as fitting parameters. In the present work these parameters have been taken from the literature [111, 112, 113, 114, 115]. Their values for the molecules studied here are listed in Tab. 6.1.

In the molecules with heteroatoms, here thiophene (S) and pyridine (N), the transfer integral for the C-C bonds are calculated from the empirical formula [111]

$$t_{\text{C-C}} = t + 3.2\,(R_{\text{C-C}} - 1.397)\,, \tag{6.6}$$

where $R_{\text{C-C}}$ is the C-C distance (in Å) and t is the transfer integral (in eV) for the conjugated bonds of benzene with $R_{\text{C-C}} = 1.397$ Å.

It should be noted that the parameters used here have been fitted to optical excitation spectra of the molecules. An exact agreement with experimental values for the molecular gaps is therefore not obtained.

6.3 Exact diagonalization

Exact diagonalization refers to an approach where the diagonalization of a many-body Hamiltonian is carried out directly in the Fock space spanned by many-particle states (Slater determinants). Since the dimensionality of the Fock space grows exponentially with the number of basis orbitals L, it is important to exploit symmetries of the Hamiltonian. This can help to reduce the dimensionality of the matrix to be diagonalized considerably. For the Pariser-Parr-Pople Hamiltonian in Eq. (6.3) the number of up and down electrons, $N_\uparrow$ and $N_\downarrow$, are good quantum numbers since their corresponding

L	dimension	memory
2	4	32 B
6	400	3 kB
8	4900	38 kB
10	63504	0.5 MB
12	853776	6.5 MB
14	11778624	90 MB
16	165636900	1.2 GB

Table 6.2: Dimensionality and memory requirements for a state vector of the half-filled subblock of the Fock space for different values of the number of basis orbitals L. The state vector is assumed stored in double floating point precision.

operators commute with the Hamiltonian. This implies that the diagonalization can be carried out in each of the $(N_\uparrow, N_\downarrow)$-subblocks of the Fock space independently. The dimensionality d of each $(N_\uparrow, N_\downarrow)$-subblock is given by the number of ways $N_\uparrow$ spin up electrons and $N_\downarrow$ spin down electrons can be distributed over L basis orbitals,

$$d(N_\uparrow, N_\downarrow) = \frac{L!}{N_\uparrow!(L-N_\uparrow)!} \times \frac{L!}{N_\downarrow!(L-N_\downarrow)!}. \tag{6.7}$$

Most often the ground state is located in the half-filled subblock, i.e. $N_\uparrow = N_\downarrow = L/2$. The dimensionality of this subblock together with the memory requirements for a single state vector belonging to this subblock are listed in Tab. 6.2 for different values of L. Already at $L = 16$ the memory requirements for a single state vector is on the order of the amount of RAM memory available in modern computers. With such memory requirements a full diagonalization of the Hamiltonian is of course out of reach. However, if only the ground state and a few low lying excited states are needed, iterative methods can be employed. Even with iterative methods one is restricted to a relatively small number of basis orbitals. To put things in perspective, the current world record in exact diagonalization using iterative methods is a 22 site Hubbard model with 9 and 8 up and down electrons. This corresponds to a Hilbert space dimension of ~ 159 billion resulting in a memory requirement of ~ 1 TB per state vector [116].

The following sections give a brief overview of some of the technical aspects and algorithms of an exact diagonalization scheme. Apart from an iterative diagonalization method, a scheme for the calculation of the Green's function is also presented.

6.3.1 Representation of the basis states

In the language of second quantization the basis states of the Fock space are specified in terms of the occupation numbers $n_{i\sigma}$ (= 0 or 1) of the single-particle basis orbitals

$$|\Phi_n\rangle = |n_{1\uparrow} \cdots n_{L\uparrow}, n_{1\downarrow} \cdots n_{L\downarrow}\rangle = \prod_{i\sigma} (c_{i\sigma}^\dagger)^{n_{i\sigma}} |0\rangle. \tag{6.8}$$

The exact meaning of this short hand notation is given by the expression in terms of the creation operators on the right-hand side. The order in which the creation operators are applied to the vacuum state $|0\rangle$ is a matter of convention, but due to the anti-commutation relations for the fermionic creation and annihilation operators nevertheless important.

In order to make the implementation of the basis states memory efficient it is convenient to map the sequence of occupation numbers $n_{i\sigma}$ onto a sequence of bits. If the number L of basis orbitals is smaller than or equal to 16, the bit representation of a 32-bit unsigned integer I can be used to represent the occupation numbers of each basis state. Denoting by $I_\uparrow$ and $I_\downarrow$ the integers with bit representations corresponding to the individual spin up and spin down configurations of a basis state, the integer representation of this state is obtained as

$$I = I_\uparrow + 2^L I_\downarrow. \tag{6.9}$$

The restriction to the $(N_\uparrow, N_\downarrow)$-subblocks of the Fock space implies that only integers whose binary representations have exactly N_σ bits set represent valid spin configurations. In practice, the integers corresponding to allowed spin configurations can be found by looping over the 2^L possible candidates and checking the number of set bits. If an integer meets the criterion it is stored in separate arrays for the up and down configurations. Subsequently, the integer representations of the product basis states in Eq. (6.9) are constructed and stored in an array of length $d(N_\uparrow, N_\downarrow)$. The index position of the integer in this array can be used as a label for the corresponding state.

The multiplication of the Hamiltonian with a general state vector $|\Psi\rangle$ is a central part of the iterative Lanczos method which will be introduced in the next section. In terms of the basis states the multiplications is

$$H|\Psi\rangle = \sum_n c_n H|n\rangle, \tag{6.10}$$

where $|n\rangle = |\Phi_n\rangle$ and $c_n = \langle n|\Psi\rangle$ are the expansion coefficients of the state in the targeted subblock of the Fock space. The application of the Hamiltonian

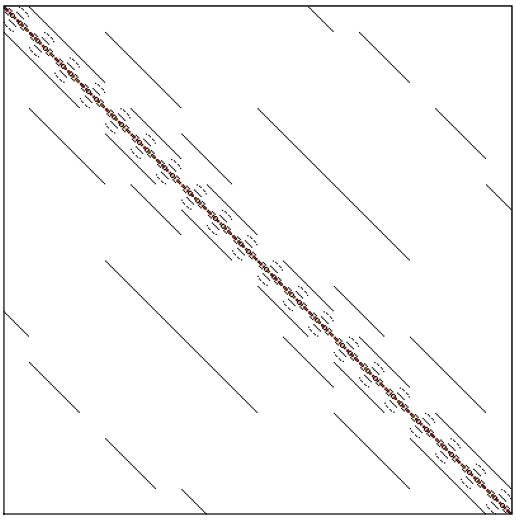

Figure 6.1: 400×400 matrix representation of the PPP-Hamiltonian for benzene in the half-filled subblock of the Fock space with $N_\uparrow = N_\downarrow = 3$.

to a basis state $|n\rangle$ can be carried out using bitwise operations on the binary representation of the corresponding integer. This generates a new vector

$$H|n\rangle = \sum_{n'} \langle n'|H|n\rangle |n'\rangle, \tag{6.11}$$

where the number of nonzero terms depends on the sparsity of the Hamiltonian. For states $|n'\rangle$ where the matrix element $\langle n'|H|n\rangle$ is different from zero, the integer representation of the state must be mapped back to its index in the subblock basis in order to update the coefficients of the product state $H|\Psi\rangle$. If the basis states are stored in increasing order of their integer value, a binary search of the basis array can be used to find the index of a given state in the basis. With this approach the memory requirements of an additional look-up table that tabulates the correspondence between the integer representation and the index is avoided.

In the Pariser-Parr-Pople Hamiltonian in Eq. (6.3) only the hopping terms give rise to off-diagonal elements. The Coulomb interaction only reads off the occupations numbers without modifying the basis states and is therefore diagonal. The inclusion of only nearest neighbor hopping results in highly sparse matrix representations. This is illustrated in Fig. 6.1 for the Hamiltonian of benzene ($L = 6$) in the half-filled subspace. Due to the long range Coulomb interaction included in the PPP-Hamiltonian, all the diagonal elements are of the same order of magnitude. This is in contrast to Hubbard Hamiltonians which only includes the onsite part of the Coulomb interaction

in Eq. (6.3). In this case the diagonal is dominated by states with doubly occupied sites which results in eigenstates that are qualitative different from those of the PPP-Hamiltonian.

6.3.2 Calculating the ground state - Lanczos algorithm

The basic idea of iterative methods is to project the Hamiltonian onto the Krylov subspace $\mathcal{K}$ generated by repeated applications of H on an arbitrary initial state $|\phi_0\rangle$, i.e.

$$\mathcal{K} = \text{span}\{|\phi_0\rangle, H|\phi_0\rangle, H^2|\phi_0\rangle, \cdots, H^{M-1}|\phi_0\rangle\}. \tag{6.12}$$

In the Krylov subspace the extreme eigenvalues of the Hamiltonian converge fast with respect to the size M of the subspace, thus reducing the full diagonalization to a manageable diagonalization of a $M \times M$ matrix with $M \ll d$.

In the Lanczos algorithm [1] the Hamiltonian is projected onto a specially constructed orthogonalised Krylov basis in which the Hamiltonian has a tridiagonal representation [118]. The basis vectors are generated recursively as

$$|\phi_{n+1}\rangle = H|\phi_n\rangle - a_n|\phi_n\rangle - b_n^2|\phi_{n-1}\rangle, \tag{6.13}$$

where the coefficient are given by

$$a_n = \frac{\langle\phi_n|H|\phi_n\rangle}{\langle\phi_n|\phi_n\rangle} \quad \text{and} \quad b_n^2 = \frac{\langle\phi_n|\phi_n\rangle}{\langle\phi_{n-1}|\phi_{n-1}\rangle} \tag{6.14}$$

with initial conditions $b_0 = 0$ and $|\phi_{-1}\rangle = 0$. At any point during the Lanczos iterations only three Lanczos vectors need to be kept in memory, which makes the algorithm memory efficient. In the basis of the normalized vectors (the basis vectors above are not normalized) the Hamiltonian has the following tridiagonal representation

$$H = \begin{pmatrix} a_0 & b_1 & 0 & \cdots & 0 \\ b_1 & a_1 & b_2 & & \vdots \\ 0 & b_2 & a_2 & \ddots & 0 \\ \vdots & & \ddots & \ddots & b_M \\ 0 & \cdots & 0 & b_M & a_M \end{pmatrix} \tag{6.15}$$

which can be readily diagonalized with methods for tridiagonal matrices yielding the ground state energy E_0. In practice the Lanczos iterations are

[1] The present work has used the implementation from the IETL project [117].

continued until the desired eigenvalues have converged to a given tolerance. For the ground state energy, typical values for M range from a few to ~ 200 depending on the system size.

The ground state resulting from a diagonalization of the tridiagonal Hamiltonian in Eq. (6.15) is provided in the Lanczos basis, i.e. $|\Psi_0\rangle = \sum_n \alpha_n |\phi_n\rangle$. In order to be able to calculate the Green's function, its representation in the original many-body basis is required. Since the Lanczos vectors are not stored, the Lanczos iterations must be repeated (starting from the same initial vector) to obtain the expansion coefficients in the original many-body basis, $c_i = \sum_n \alpha_n \langle \Phi_i | \phi_n \rangle$.

The most time consuming part of the Lanczos algorithm is the matrix-vector multiplication $H|\phi_n\rangle$. An efficient implementation of this part is therefore crucial for the performance of the Lanczos algorithm. If the Hamiltonian can be stored on sparse form in memory, fast matrix-vector multiplication routines can be used. However, for large systems where the whole memory is used by the Lanczos vectors this is not possible. In this case the matrix elements of the Hamiltonian, or rather its action on the basis states, must be recalculated on the fly in each iteration. With the basis states coded as unsigned integers, this can be done efficiently using bitwise operations.

6.3.3 Calculating the Green's function

Having obtained the ground state, the Green's function can now be calculated. From the Lehmann representation of the Green's function it follows that it can be written as

$$G^r_{ij}(\varepsilon) = G^e_{ij}(\varepsilon) + G^h_{ij}(\varepsilon) \tag{6.16}$$

with the electron and hole Green's functions defined by

$$G^e_{ij}(\varepsilon) = \langle \Psi^N_0 | c_i \frac{1}{\varepsilon - H + E^N_0 + i\eta} c^\dagger_j | \Psi^N_0 \rangle \tag{6.17}$$

and

$$G^h_{ij}(\varepsilon) = \langle \Psi^N_0 | c^\dagger_j \frac{1}{\varepsilon + H - E^N_0 + i\eta} c_i | \Psi^N_0 \rangle, \tag{6.18}$$

respectively. The electron Green's function is the matrix representation of the resolvent operator $(z - H)^{-1}$ in the basis spanned by the $|i\rangle = c^\dagger_i |\Psi^N_0\rangle$ vectors. To obtain the i'th diagonal element,

$$G^e_{ii}(\varepsilon) = \langle i | (z - H)^{-1} | i \rangle, \tag{6.19}$$

where $z = \varepsilon - E^N_0 + i\eta$, again the Lanczos algorithm is used to put H on a tridiagonal form, but this time the Lanczos iterations are started from the

normalized initial state $|\phi_0\rangle = |i\rangle/b_0$ where $b_0^2 = \langle i|i\rangle$. In the generated Krylov subspace the diagonal element of the Green's function corresponds to the matrix element $b_0^2[(\varepsilon - H + E_0^N + i\eta)^{-1}]_{11}$, which can be obtained as the continued fraction [119]

$$G_{ii}^e(\varepsilon) = \cfrac{b_0^2}{z - a_0 - \cfrac{b_1^2}{z - a_1 - \cfrac{b_2^2}{z - a_2 - \cdots}}}. \tag{6.20}$$

Again the Lanczos iterations are continued until the frequency dependent Green's function element has converged. The elements of the hole Green's function can be calculated similarly by starting the Lanczos iterations from the vector $|i\rangle = c_i|\Psi_0^N\rangle$.

6.3.4 Correlation measure - von Neumann entropy

The following section demonstrates how a quantitative measure of the level of correlations in a system can be obtained by considering the von Neumann entropy of the single-particle density matrix ρ. The entropy is defined by

$$S = -\mathrm{Tr}[\rho \log \rho] = -\sum_n \rho_n \log \rho_n, \tag{6.21}$$

where in the last equality ρ has been expressed in its diagonal representation, $\rho = \sum_n \rho_n |n\rangle\langle n|$.

In the basis of the atomic p_z orbitals of the PPP-Hamiltonian the matrix elements of the reduced density matrix of the ground state $|\Psi_0\rangle$ are given by (with the spin index suppressed)

$$\rho_{ij} = \langle \Psi_0 | c_j^\dagger c_i | \Psi_0 \rangle. \tag{6.22}$$

The diagonal elements ρ_{ii} of the density matrix correspond to the site occupations n_i of the ground state $|\Psi_0\rangle$. When expressed in its diagonal representation ρ_n represents the occupation of the eigenstate $|n\rangle$ of the density matrix.

In the half-filled subblock of the Fock space the ground state entropy is limited to $0 \leq S \leq L \log 2$, where $2L$ is the dimension of the single-particle Hilbert space including spin. Here, $S = 0$ corresponds to a state with no correlations, while the maximum value $S_{\max} = L \log 2$ for the entropy corresponds to a maximally correlated state. This follows from the natural diagonal representation of the density matrix in the two extreme cases (see

below). Therefore, the number $0 \leq S/S_{\max} \leq 1$ represents a natural measure of the degree of correlation in the state $|\Psi_0\rangle$.

By definition, Hartree-Fock theory is exact if the ground state in uncorrelated. Hence, the ground state is given by the Slater determinant

$$|\Psi_0\rangle = \prod_{\nu\sigma} c^\dagger_{\nu\sigma}|0\rangle, \tag{6.23}$$

where $c^\dagger_{\nu\sigma}$ are the creation operators for the single-particle Hartree-Fock orbitals ϕ_ν. Due to the mutual orthogonality of the HF orbitals, the density matrix is diagonal in this basis with eigenvalues equal to one for the occupied and zero for the unoccupied (virtual) orbitals. As a consequence, $S = 0$ for an uncorrelated state as stated above.

Hubbard models where only onsite interactions are included give rise to strongly correlated states. The singlet ground state $|\Psi_{\mathrm{s}}\rangle$ of the two-site Hubbard model in the limit $U \gg t$ is an example of a maximally correlated state. Due to the high U/t-ratio, the energy cost of having two electrons at the same site becomes prohibitly high. The ground state is therefore completely dominated by the two states with singly occupied sites

$$|\Psi_{\mathrm{s}}\rangle = \frac{1}{\sqrt{2}}\left(c^\dagger_{2\uparrow}c^\dagger_{1\downarrow}|0\rangle - c^\dagger_{2\downarrow}c^\dagger_{1\uparrow}|0\rangle\right), \tag{6.24}$$

where the positions of the spins refer to the site index. The corresponding density matrix is diagonal in the site basis with site occupations $n_{i\sigma} = 1/2$ from which $S = S_{\max}$ follows. In general, maximally correlated states have dominating weight on small subsets of orthogonal determinants corresponding to the energetically most favorable basis states. In Hubbard models where the onsite Coulomb repulsion dominates over the kinetic energy these are the basis states with no doubly occupied sites.

6.4 Results

The following two sections present the benchmark results for the seven conjugated molecules in Tab. 6.3. In the first section the accuracy of the GW ground state energies for the neutral molecules is represented in terms of the correlation energy. The second section focus on the spectral properties and the different contributions from Eq. 6.2 to the quasi-particle energies in GW. The GW results reported here have been obtained with a fully self-consistent GW scheme without any further approximations to the electronic self-energy apart from the GW approximation itself (see Ref. [120] for details).

6.4.1 Total energies

A good starting point for the following analysis is the von Neumann entropies of the density matrices which establish the degree of correlation and the qualitative nature of the exact ground states. The ground state entropies are listed in Tab. 6.3. For all molecules the entropy is $\sim 10\%$ of the maximum value $S_{\max}$ corresponding to weakly correlated systems. For comparison, the ground state entropy for a Hubbard description of benzene with $U/t \sim 4$ is 50% of its maximum value. The Hamiltonian of the Hubbard description of benzene is identical to the PPP-Hamiltonian in Eq. (6.3) except for the long range Coulomb interactions in the third term which are left out. The finite values of the ground state entropies for the molecules reveal that none of the ground states are single determinants implying that the Hartree-Fock ground state energies will be larger than the exact ones.

Following the usual convention, the correlation energy is here defined as the part of the total energy not included in Hartree-Fock, i.e.

$$E_{\text{corr}} = E_{\text{exact}} - E_{\text{HF}}. \tag{6.25}$$

The HF energies are obtained via a self-consistent solution to the single-particle HF Hamiltonian which for the PPP-Hamiltonian reads

$$\begin{aligned} H_{\text{HF}} = &\sum_i \tilde{\varepsilon}_i \hat{n}_i - \sum_{\langle ij\rangle\sigma} t_{ij} c^\dagger_{i\sigma} c_{j\sigma} \\ &+ \sum_{ij\sigma} \left[\delta_{ij} \sum_k V_{ik} n_k - V_{ij} \rho_{ij,\sigma} \right] c^\dagger_{i\sigma} c_{j\sigma}, \end{aligned} \tag{6.26}$$

	Formula	L	$S/S_{\max}$	E_{gap}
Thiophene	C_4H_4S	5	0.08	11.19
Pyridine	C_5H_5N	6	0.11	10.61
Benzene	C_6H_6	6	0.10	11.39
Biphenyl	$C_{12}H_{10}$	12	0.10	9.24
Naphthalene	$C_{10}H_8$	10	0.11	8.65
Anthracene	$C_{14}H_{10}$	14	0.12	7.06
OPV2	$C_{14}H_{12}$	14	0.10	8.30

Table 6.3: Chemical formula, number of p_z orbitals (L) included in the PPP-model, ground state entropies relative to maximum entropies ($S/S_{\max}$) and exact gaps (in eV) for the listed molecules.

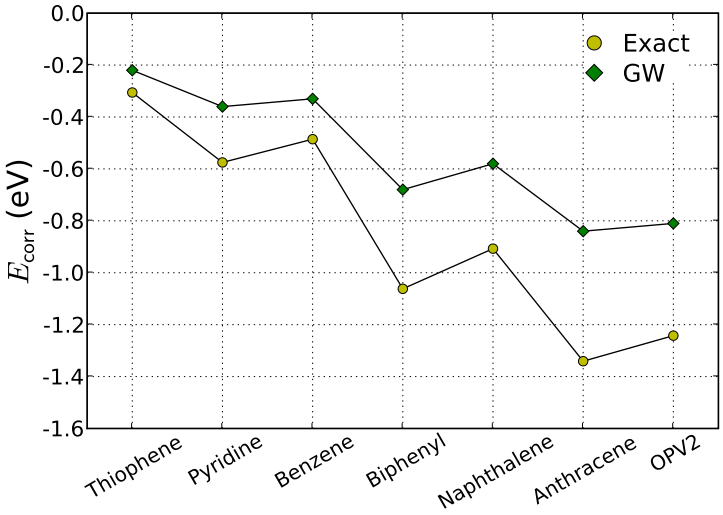

Figure 6.2: Exact and GW correlation energies of the neutral ground states for the seven molecules. Both are calculated as the difference in total energy with respect to the Hartree-Fock energy, i.e. $E_{\mathrm{corr}} = E - E_{\mathrm{HF}}$.

where $\tilde{\varepsilon}_i = \varepsilon_i - \sum_{k \neq i} V_{ik} Z_k$ and $V_{ii} = U_i$. The last term contains the Hartree potential which is diagonal in the site indices and the exchange potential which has off-diagonal contributions. The resulting eigenfunctions ϕ_ν are the canonical molecular orbitals from which the ground state Slater determinant in Eq. (6.23) is constructed. The total energy E_{HF} then follows by taking the expectation value of the PPP-Hamiltonian with respect to the ground state Slater determinant. The expectation value of the non-interacting part can be expressed directly in terms of the reduced density matrix. For the interacting part of the PPP-Hamiltonian, the expectation value can be evaluated by applying Wick's theorem to the product of creation and annihilation operators hidden in the site occupation operator $\hat{n}_i$. The resulting expression for the total energy can be written as

$$E_{\mathrm{HF}} = \langle H \rangle_{\mathrm{HF}} = \sum_{i\sigma} \tilde{\varepsilon}_i \rho_{ii,\sigma} - \sum_{ij\sigma} t_{ij} \rho_{ij\sigma} + \frac{1}{2} \sum_{\substack{ij \\ \sigma\sigma'}} V_{ij} \left[\rho_{ii,\sigma} \rho_{jj,\sigma'} - \delta_{\sigma,\sigma'} \rho_{ij,\sigma} \rho_{ji,\sigma} \right]. \tag{6.27}$$

The second term in the last sum is the exchange energy whose diagonal contribution removes the self-interactions included in the first Hartree term.

The GW total energy is identical to the HF energy above with the exception that the exchange-correlation energy [121]

$$E_{\mathrm{xc}} = \frac{1}{2i}\int \mathrm{Tr}\left[\Sigma^r(\varepsilon)G^<(\varepsilon) + \Sigma^<(\varepsilon)G^a(\varepsilon)\right] d\varepsilon \tag{6.28}$$

replaces the exchange energy in HF and the GW density matrix obtained from the GW Green's function (see App. C) replaces the HF density matrix.

Fig. 6.2 shows the exact correlation energies of the neutral ground states together with those obtained from the GW approximation. For the series of molecules considered here the correlation energy constitute less than 0.5% of the total energies. Furthermore, as expected, it increases (in absolute size) with the number of atoms in the molecule. The GW approximation performs reasonably well for all the molecules capturing on average 66% of the correlation energy.

6.4.2 Spectral properties

For isolated systems such as molecules, true quasi-particles resembling single-particle excitations are characterized by having a weight close to unity (for non-degenerate levels) in the spectral function, i.e.

$$Z_n = \sum_i |\langle \Psi_n^{N+1}|c_i^\dagger|\Psi_0^N\rangle|^2 \sim 1. \tag{6.29}$$

This is equivalent to the existence of a molecular orbital ϕ_ν which allow the excited state $|\Psi_n^{N+1}\rangle$ to be written as the single-particle excitation $c_\nu^\dagger|\Psi_0^N\rangle$. Fig. 6.3 shows the single-particle density of states (DOS),

$$D(\varepsilon) = \sum_i A_i(\varepsilon) \tag{6.30}$$

for the OPV2 molecule on a logarithmic scale. The height of the peaks reflects the value of Z_n (modulo degeneracies). The HF and, in particular, the GW approximation reproduce the lowest lying excitations quite well while higher excitations are poorly described. All the peaks in the HF spectrum have $Z_n = 1$ while GW shifts some spectral weight from the main peaks to tiny satellite structures (at higher energies than shown on the plot). This is in agreement with the exact results. For example, the exact spectral weight of the LUMO is $Z_{\mathrm{LUMO}} \sim 0.92$ and ~ 0.97 in GW. However, the GW satellites do not correspond to features in the exact spectrum. This shows that excitations with $Z_n \ll 1$, i.e. excitations which do not have single-particle character, are

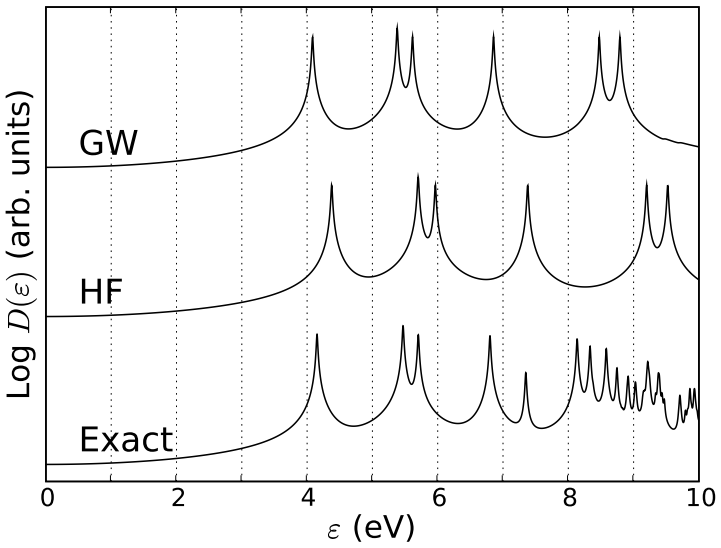

Figure 6.3: Single-particle DOS of the OPV2 molecule. The curves have been shifted vertically for clarity. Note the logarithmic axis.

not well described within GW whose main effect is to improve the position of the HF single-particle peaks.

In the following the relative contributions of Δ_{relax} and Δ_{corr} from Eq. (6.2) to the HOMO and LUMO energies of the molecules are addressed. Fig. 6.4 shows the difference between the exact gaps, which are listed in Tab. 6.3, and the gaps obtained from (i) the eigenvalues of the Hartree-Fock Hamiltonian in Eq. (6.26) which correspond to the quasi-particle energies of the HF spectral function, (ii) Hartree-Fock total energy differences which includes self-consistent relaxations in the $N \pm 1$ Slater determinants, and (iii) the distance between the HOMO and LUMO peaks in the GW spectral function. Using the expression for the quasi-particle energies in Eq. (6.2), the exact gap $E_{\text{gap}} = \varepsilon_{\text{LUMO}} - \varepsilon_{\text{HOMO}}$ can be expressed as

$$E_{\text{gap}} = \varepsilon^{\text{HF}}_{\text{LUMO}} - \varepsilon^{\text{HF}}_{\text{HOMO}} + \Delta^{\text{gap}}_{\text{relax}} + \Delta^{\text{gap}}_{\text{corr}}, \tag{6.31}$$

where $\Delta^{\text{gap}}_{\text{relax}}$ and $\Delta^{\text{gap}}_{\text{corr}}$ are the gap equivalents of the corresponding quantities in Eq. (6.2) and $\varepsilon^{\text{HF}}_{\text{HOMO/LUMO}}$ are the Hartree-Fock HOMO/LUMO eigenvalues. By definition $\Delta^{\text{gap}}_{\text{relax}}$ is difference between the gaps obtained from the HF eigenvalues and relaxed HF total energy differences. In Fig. 6.4 this is given by the vertical distance between the (red) squares and (blue) circles. The correlation contribution $\Delta^{\text{gap}}_{\text{corr}}$ can be read off as the difference between the exact gap (solid horizontal line) and the relaxed HF total energy gap (red

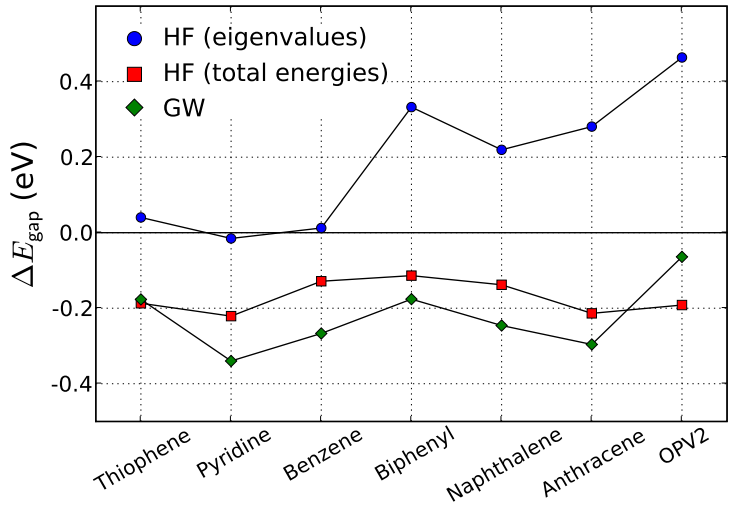

Figure 6.4: The molecular gaps $E_{\mathrm{gap}} = \varepsilon_{\mathrm{LUMO}} - \varepsilon_{\mathrm{HOMO}}$ relative to the exact values in Tab. 6.3. In addition to the HF and GW single-particle gaps, the gaps obtained from relaxed Hartree-Fock total energy differences, i.e. $E_{\mathrm{gap}} = E_{\mathrm{HF}}^{N+1} + E_{\mathrm{HF}}^{N-1} - 2E_{\mathrm{HF}}^{N}$ are also shown. The excellent results of HF for the three smallest molecules is a result of error cancellation between relaxation and correlation contributions.

squares). The relaxation effects included in the total energy based HF gaps leads to reduced gaps as compared to the HF eigenvalue gaps, implying that $\Delta_{\mathrm{relax}}^{\mathrm{gap}} < 0$. This reduction is due to the screening from the orbital relaxation which reduces the Coulomb interaction with the added hole or electron and hence also the gap.

It should be noted that the HF eigenvalues give excellent gaps for the small single-ring molecules thiophene, pyridine and benzene. The good agreement with the exact levels for these systems is not a result of HF giving a correct description of the many-body states and their energies – this was already clear from the entropy analysis above which showed that the eigenstates are not single Slater determinants and hence the excitation energies in Eq. (6.2) have contributions from both Δ_{relax} and Δ_{corr}. The good agreement must therefore be ascribed to cancellations between the relaxation and correlation contribution to the exact quasi-particle energies.

In contrast to the HF (eigenvalue) gaps for which the agreement with the exact gap worsens as a function of the size of the molecules, the GW gaps follow more consistently the same trend and underestimates the exact gaps with $0.05 - 0.35$ eV for all the molecules. The close resemblance between GW and the relaxed HF result indicates that the effect of GW is mainly to

account for the screening effects that are given by orbital relaxations Δ_{relax} in HF.

6.4.3 Lattice DFT

To demonstrate the shortcomings DFT when it comes to the interpretation of the Kohn-Sham eigenvalues $\varepsilon_i^{\text{KS}}$ as excitation energies, the spectrum of the benzene molecule as obtained with the lattice formulation of DFT [122] is here inspected.

The lattice version of DFT follows by extending the fundamental concepts of normal DFT, such as the Hohenberg-Kohn theorem and the Kohn-Sham equations, to model Hamiltonians as e.g. the PPP-Hamiltonian. In this reformulation of DFT the site occupations n_i replaces the continuous electron density $n(\mathbf{r})$ as the fundamental variable that determines the ground state properties. The lattice version of the single-particle Kohn-Sham Hamiltonian H_{KS} is given by the sum of the hopping terms (the kinetic energy) and a site dependent Kohn-Sham potential V_i^{KS} which is constructed to yield the correct site occupations of the ground state,

$$H_{\text{KS}} = -\sum_{\langle ij\rangle\sigma} t_{ij} c_{i\sigma}^{\dagger} c_{j\sigma} + \sum_i V_i^{\text{KS}} \hat{n}_i. \tag{6.32}$$

For the present purpose the explicit form of the site potential V_i^{KS} is not important. The fact that the lattice version of the Kohn-Sham potential is an onsite potential, is equivalent to the restriction of the Kohn-Sham potential $V_{\text{xc}}(\mathbf{r})$ in the real-space formulation of DFT to a local potential.

Due to the high symmetry of the benzene molecule all sites in the PPP-Hamiltonian are equivalent implying that V_i^{KS} has the same value for all sites. Except for a constant shift, the eigenvalues of the Kohn-Sham Hamiltonian are therefore given by those of the hopping part of the Hamiltonian. The HOMO-LUMO gap calculated from the Kohn-Sham eigenvalues is $E_{\text{gap}}^{\text{KS}} = 5.08$ eV which is a severe underestimation of the true gap of 11.39 eV.

To illustrate why the Kohn-Sham eigenvalues in general seem to consistently underestimate molecular gaps, a closer look at the Hartree-Fock Hamiltonian in Eq. (6.26) is instructive. As Fig. 6.4 showed, HF gave relatively good values for the gaps reproducing the exact gaps to within ~ 0.50 eV. The Hartree-Fock Hamiltonian is diagonal in the basis $\{\phi_\nu\}$ of molecular orbitals

$$H_{\text{HF}} = \sum_{\nu\sigma} \varepsilon_{\nu\sigma} \hat{n}_{\nu\sigma}, \tag{6.33}$$

with the diagonal elements (eigenvalues) given by

$$\varepsilon_{\nu\sigma} = t_{\nu\nu} + \sum_{\mu\sigma'} V_{\nu\mu} n_{\mu\sigma'} - V_{\nu\nu} n_{\nu\sigma}. \tag{6.34}$$

Notice that only the direct elements $V_{\nu\nu\mu\mu}$ of the Coulomb interaction have been included here. Due to the delocalized nature of the molecular orbitals this is in general not a good approximation. For the present purpose, however, this suffices to illustrate the point made below.

The exchange contribution to the eigenvalue in the last term removes the self-interaction contribution to the eigenvalue included in the Hartree part in the second term. However, since it depends on the occupation of the molecular orbital itself which is 1 for occupied and 0 for (virtual) unoccupied orbitals, only the occupied orbitals are affected by this self-interaction correction. This illustrates the orbital dependence of the single-particle HF potential – i.e. the fact that the HF Hamiltonian differs for occupied and unoccupied orbitals. This distinction between occupied and unoccupied orbitals, which is a consequence of the non-locality of the HF potential, cannot be obtained with a local site dependent potential in lattice DFT. The underestimation of the gap thus seems to be a intrinsic property of the Kohn-Sham formulation of DFT.

For benzene, the molecular orbitals from the non-interacting Hamiltonian and the HF Hamiltonian are identical implying that $t_{\nu\nu} = \varepsilon_\nu^{\mathrm{KS}}$. The difference between the Kohn-Sham gap and HF gap is thus given by the self-interaction correction of the HOMO level.

6.5 Conclusion and outlook

The present chapter has demonstrated that the GW approximation gives consistently good quasi-particle energies and gaps for the range of molecule considered here. In contrast the gaps obtained from the eigenvalues of the single-particle Hartree-Fock Hamiltonian which showed large variations in the errors, the GW approximation systematically underestimated the molecular gaps. The GW results were found to agree well with HF total energy calculations of the gaps in which relaxation of the molecular orbitals for the charged molecule is taken into account.

Furthermore, the failure of the interpretation of the Kohn-Sham DFT eigenvalues as excitation energies was demonstrated with a simple example. From the lattice version of DFT the gap of the benzene molecule was found to be severely underestimated by more than a factor of two.

The GW approximation has recently been extended to non-equilibrium situations within the framework of the non-equilibrium Green's function formalism. It has been applied to quantum transport calculations on single-molecule junction in the strong coupling regime [120, 123, 124], i.e. where the hybridization between the molecule and metal contacts is significant. As this results in extended states and decreased life-times of molecular states, dynamical polarization effects can be expected to be important in these junctions.

So far, first-principles calculations on single-molecule junctions in the strong coupling regime have almost exclusively been based on DFT descriptions of the electronic structure of the junction (see e.g. [125, 126, 127]). However, the zero bias conductance resulting from this approach does typically not agree with experimental values and is sometimes orders of magnitudes larger [128, 129]. The uncertainty connected with the atomic structure of the junction and the position of the molecule in the experiments is one possible reason for this discrepancy. Since the conductance of a single-molecule junction is highly dependent on the position of the molecular levels, the use of DFT in these calculation could be another possible reason for the observed discrepancies. Indeed, it has been demonstrated that better agreement with experiment is obtained by correcting the DFT levels of the molecule to represent true excitation energies [130, 131]. The corrections applied to the DFT levels in these works include (i) a shift of the HOMO level to fit known experimental ionization potentials, and (ii) a polarization shift of the levels equivalent to the polarization integral in Eq. (5.14).

With GW giving a good description of both excitation energies of molecules and polarization effects, it will be interesting to follow its development with respect to transport calculations in the strong coupling regime. Due to the computational requirements of a fully self-consistent GW calculation, such calculations are presently limited to simple junctions with small molecules.

Appendix A

Atomic units

The atomic unit system is often used in condensed matter physics and quantum chemistry which deals with the electronic properties of solids and molecules. Its three fundamental units which are set to unity is the electronic mass, the elementary charge and Planck's constant divided by 2π, i.e. $m_e = e = \hbar = 1$. They are listed in table A.1 together with some of the derived units.

In atomic units the Coulomb interaction simplifies to

$$V_C(r) = \frac{e^2}{4\pi\epsilon_0 r} \quad \rightarrow \quad \frac{1}{r} \approx \frac{14.4}{r} \text{ eV Å}, \tag{A.1}$$

where ϵ_0 is the permittivity of vacuum. The last equality provides a good figure of merit to keep in mind when considering electron-electron interaction in molecules and nanostructures.

Atomic Units		
Quantity	**Symbol**	**SI value**
mass	m_e	9.109×10^{-31} kg
charge	e	1.602×10^{-19} C
angular momentum	$\hbar$	1.054×10^{-34} J s
length	a_0	5.291×10^{-11} m
energy	E_h	4.359×10^{-18} J
permittivity	$4\pi\epsilon_0$	1.113×10^{-10} C^2 N^{-1} m^{-2}

Table A.1: The atomic unit system which follows by setting $m_e = e = \hbar = 1$.

Appendix B

Self-consistent Hückel scheme

In this appendix a semi-empirical treatment of the effective single-particle junction Hamiltonian in Eq. (2.23) is presented. It is based on the extended Hückel method [132] which has been developed to describe electronic structure of organic molecules. As this method is not self-consistent it is here extended within the framework of self-consistent Hartree theory. The resulting self-consistent scheme is similar to the one presented in Ref. [133].

For completeness the single-particle version of the junction Hamiltonian in Eq. (2.23) is given here once more,

$$\begin{aligned} H_{\text{eff}} &= -\frac{1}{2}\nabla^2 + V_{\text{ion}}(\mathbf{r}) + V_{\text{H}}(\mathbf{r}) + V_{\text{xc}}(\mathbf{r}) + V_{\text{ind}}(\mathbf{r}) + V_{\text{ext}}(\mathbf{r}) \\ &= H_{\text{mol}} + H_{\text{junc}}. \end{aligned} \tag{B.1}$$

Here, the first four terms, which are described together as H_{mol}, stem from the molecule itself. The last two terms included in H_{junc} describe the potential in the junction (see e.g. Chap. 3).

In the self-consistent Hückel scheme the molecular part of the Hamiltonian is written as a sum of a constant term H_0 and a self-consistent term H_{SC}

$$H_{\text{mol}} = H_0 + H_{\text{SC}}. \tag{B.2}$$

The constant term H_0 accounts for the effective Hamiltonian of the isolated molecule. It is approximated by the non-interacting Hückel Hamiltonian

$$H_0 = \sum_i \varepsilon_i c_i^\dagger c_i + \sum_{i \neq j} t_{ij} c_i^\dagger c_j, \tag{B.3}$$

where the sums runs over atomic valence orbitals $\{\phi_i\}$ and i is a collective index referring to atom, orbital and spin index. Within Hückel theory the

onsite energies ε_i and transfer integrals t_{ij} are described with the Hoffman parametrization [132]

$$\varepsilon_i = -V_i \tag{B.4}$$

$$t_{ij} = \frac{1}{2} k S_{ij} \left(\varepsilon_i + \varepsilon_j\right). \tag{B.5}$$

Here, V_i is associated with the ionization energy of the valence orbital ϕ_i, k is a fitting parameter usually set to $k = 1.75$ and $S_{ij} = \langle \phi_i | \phi_j \rangle$ is the overlap between the non-orthogonal atomic orbitals. Notice that Hartree and exchange-correlation effects are implicitly included in H_0 due to its parametrized form.

The self-consistent term H_{SC} of the molecular Hamiltonian takes into account electron-electron interactions at the level of Hartree theory. It accounts for rearrangement of the molecular charge distribution due to additional charges on the molecule and external potentials from the junction. Since the Hartree potential of the isolated molecule is indirectly included in H_0, only changes in the Hartree potential due to variations in the electron density from its value n_0 in the isolated molecule are considered,

$$\delta V_{\mathrm{H}}(\mathbf{r}) = \int d\mathbf{r}' \, \frac{\delta n(\mathbf{r}')}{|\mathbf{r} - \mathbf{r}'|}. \tag{B.6}$$

Here $\delta n = n - n_0$. Since the Hartree potential depends on the electron density, this posses a self-consistent problem that must be iterated to convergence.

To simplify the numerics, the Hartree potential in equation (B.6) is approximated by a sum over atomic point charges given by the Mulliken populations $n_i = \mathrm{Tr}\left[\rho S\right]_i$. The trace is taken over the orbitals on atom i and ρ denotes the single-particle density matrix. The matrix elements of the density matrix can be expressed in terms of the expansion coefficients c_i^ν to the molecular orbitals ϕ_ν as

$$\rho_{ij} = \sum_\nu (c_i^\nu)^* c_j^\nu. \tag{B.7}$$

With the above approximation the Hartree potential reads

$$\delta V_{\mathrm{H}}(\mathbf{r}) = \sum_i \frac{\delta n_i}{|\mathbf{r} - \mathbf{r}_i|}. \tag{B.8}$$

To avoid problems with the diverging point charge potential when evaluated at the atomic positions, $\mathbf{r}_i$, the onsite contribution to the sum is replaced by a species dependent Hubbard U taking into account the energy cost of adding an electron to the atom. These parameters are taken from the quantum

chemical CNDO method [63, 134]. In order to keep consistency between the onsite and the offsite interactions, the Magata-Nishimoto [135] interpolation formula is used

$$U_{ij} = \frac{1}{R_{ij} + \frac{2}{U_i + U_j}}. \tag{B.9}$$

The final form of the Hartree potential in equation (B.6) becomes

$$\delta V_{\mathrm{H}}(\mathbf{r}_i) = \delta n_i U_i + \sum_{j \neq i} \delta n_j U_{ij}. \tag{B.10}$$

The matrix elements of the Hartree potential in the atomic Hückel basis are approximated as follows

$$\begin{aligned} V_i^{\mathrm{H}} &= \langle \phi_i | \delta V_{\mathrm{H}} | \phi_i \rangle \approx \delta V_{\mathrm{H}}(\mathbf{r}_i) \\ V_{ij}^{\mathrm{H}} &= \langle \phi_i | \delta V_{\mathrm{H}} | \phi_j \rangle \approx \frac{1}{2} S_{ij} \left(V_i^{\mathrm{H}} + V_j^{\mathrm{H}} \right). \end{aligned} \tag{B.11}$$

The matrix elements of the potentials V_{ind} and V_{ext} in the junction part H_{junc} of the Hamiltonian are approximated similarly. The potentials are obtained from a finite element solution to Poisson's equation.

In the basis of atomic orbitals the effective single-particle Hamiltonian in Eq. (B.1) can now be written

$$H_{\mathrm{eff}} = \sum_i \varepsilon_i c_i^\dagger c_i + \sum_{i \neq j} t_{ij} c_i^\dagger c_j + \sum_{i,j} V_{ij} c_i^\dagger c_j, \tag{B.12}$$

where $V = V_{\mathrm{H}} + V_{\mathrm{ind}} + V_{\mathrm{ext}}$. The total energy can be evaluated from the eigenvalues ε_ν to the effective Hamiltonian as

$$E = \sum_\nu \varepsilon_\nu - \frac{1}{2} \sum_i \left[n_i V_{\mathrm{H}}(\mathbf{r}_i) + (n_i - Z_i) V_{\mathrm{ind}}(\mathbf{r}_i) \right]. \tag{B.13}$$

The last term subtracts contributions to the total energy that are doubled counted in the eigenvalues. Here Z_i denotes the valence of atom i.

The accuracy of the self-consistent Hückel scheme has been addressed by comparing the calculated gap (see Eq. (4.2)) of the OPV5 molecule with that obtained from a more accurate DFT calculation using the B3LYP exchange-correlation functional. The comparison showed that the self-consistent Hückel scheme underestimated the gap by 1.2 eV compared to the DFT. The majority of this difference was found to stem from an underestimation of the single-particle HOMO-LUMO gap in the Hückel calculations.

Appendix C

Green's function primer

Single-particle Green's functions (GFs) are very useful when considering the electronic structure of systems. The most important properties of the retarded and lesser Green's functions relevant for the present work are presented here.

The retarded and lesser functions have the following real-space definitions

$$G^r(\mathbf{r}t, \mathbf{r}'t') = -i\theta(t-t')\langle\{\psi(\mathbf{r}t), \psi^\dagger(\mathbf{r}'t')\}\rangle \tag{C.1}$$

and

$$G^<(\mathbf{r}t, \mathbf{r}'t') = i\langle\psi^\dagger(\mathbf{r}'t')\psi(\mathbf{r}t)\rangle, \tag{C.2}$$

respectively. For systems in equilibrium the GFs depend only on the time difference $t - t'$. Therefore, their Fourier transforms depend on only one energy argument ε.

In practical calculations it is often more useful to express the GFs in some convenient basis. Depending on the problem this could be e.g. the momentum-state basis of translationally invariant systems, the Bloch states of a periodic system, or molecular and atomic orbitals for molecules. In these basis the GFs can be written generally as

$$G^r_{ij}(t-t') = -i\theta(t-t')\langle\{c_i(t), c_j^\dagger(t')\}\rangle \tag{C.3}$$

and

$$G^<_{ij}(t-t') = i\langle c_j^\dagger(t')c_i(t)\rangle \tag{C.4}$$

where the creation and annihilation operators create and annihilate electrons in the generic set of basis orbitals $\{\phi_i\}$. They are connected to the real-space representations above by a simple change of basis.

Being the expectation value of a creation followed by an annihilation operator, the lesser function contains the single-particle density matrix

$$\rho_{ij} = \langle c_i^\dagger c_j\rangle = -iG^<_{ij}(t-t'=0) = -i\int \frac{d\varepsilon}{2\pi}\, G^<_{ij}(\varepsilon). \tag{C.5}$$

The occupations n_i of the basis orbitals are given by the diagonal elements ρ_{ii} of the density matrix.

A very useful quantity is the spectral function A which is defined by the imaginary part of the retarded Green's function

$$A(\varepsilon) = -\frac{1}{\pi}\mathrm{Im}\, G^r(\varepsilon). \tag{C.6}$$

In equilibrium the lesser function can be expressed in terms of the spectral function and the Fermi distribution n_F as

$$G^<(\varepsilon) = 2\pi i A(\varepsilon) n_\mathrm{F}(\varepsilon). \tag{C.7}$$

This relation is the fluctuation-dissipation theorem for the single-particle Green's function. Using this relation, the total number of electrons $N = \sum_i n_i$ of a system follows as

$$N = \sum_i \rho_{ii} = \sum_i \int d\varepsilon\; A_i(\varepsilon) n_\mathrm{F}(\varepsilon). \tag{C.8}$$

From this expression the density of states D is seen to be given by the sum over the elements of the spectral function

$$D(\varepsilon) = \sum_i A_i(\varepsilon). \tag{C.9}$$

A useful representation of the retarded Green's function can be obtained by a spectral decomposition with respect to a complete set of many-body eigenstates

$$H|\Psi_n\rangle = E_n|\Psi_n\rangle. \tag{C.10}$$

This so-called Lehmann representation follows by inserting the identity $1 = \sum_n |\Psi_n\rangle\langle\Psi_n|$ in the definition of the retarded Green's function in Eq. (C.3) and Fourier transforming,

$$G^r_{ij}(\varepsilon) = \sum_n \left[\frac{\langle\Psi_0^N|c_i|\Psi_n^{N+1}\rangle\langle\Psi_n^{N+1}|c_j^\dagger|\Psi_0^N\rangle}{\varepsilon - (E_n^{N+1} - E_0^N) + i\eta} + \frac{\langle\Psi_0^N|c_j^\dagger|\Psi_n^{N-1}\rangle\langle\Psi_n^{N-1}|c_i|\Psi_0^N\rangle}{\varepsilon - (E_0^N - E_n^{N-1}) + i\eta} \right]. \tag{C.11}$$

For an N-electron system the sum over many-body states $|\Psi_n\rangle$ is restricted to the states $|\Psi_n^{N\pm1}\rangle$ of the $N \pm 1$-electron system. From the Lehmann representation the poles of the retarded GF are seen to coincide with the electron addition $\varepsilon_n = E_n^{N+1} - E_0^N$ and removal energies $\varepsilon_n = E_0^N - E_n^{N-1}$. Using the

identity $1/(\varepsilon + i\eta) = \mathcal{P}(1/\varepsilon) - i\pi\delta(\varepsilon)$ with $\mathcal{P}$ denoting the principal value, the Lehmann representation of the spectral function follows as

$$A_i(\varepsilon) = \sum_n \left[\left| \langle \Psi_n^{N+1} | c_i^\dagger | \Psi_0^N \rangle \right|^2 \delta(\varepsilon - \varepsilon_n) + \left| \langle \Psi_n^{N-1} | c_i | \Psi_0^N \rangle \right|^2 \delta(\varepsilon - \varepsilon_n) \right] \tag{C.12}$$

Thus, the peaks of the spectral function correspond to the charge excitations of the system.

Perturbation series in the electron-electron interactions for the GF can be formulated in terms of the time-ordered (zero temperature) Green's function

$$G_{ij}(t - t') = -i\langle T[c_i(t) c_j^\dagger(t')] \rangle \tag{C.13}$$

where T denotes the time-ordering operator. With the aid of Feynman diagrams the following Dyson equation for the time-ordered GF can be derived from the perturbation series

$$G(t - t') = G_0(t - t') + \int dt_1 \int dt_2 \; G_0(t_1 - t') \Sigma(t_2 - t_1') G(t - t_2). \tag{C.14}$$

Here, the quantities are considered as matrices in the basis indices i and j and matrix-multiplication is implied. Σ is the irreducible self-energy which contains all Feynman diagrams that cannot be split into two separate parts by cutting a single Green's function (G_0) line. Depending on the definition of G_0, the exact definition of the self-energy varies. In the present work G_0 denotes the Hartree GF implying that the Hartree self-energy diagram should not be included in the definition of Σ.

From the Dyson equation it follows that the full diagrammatic representation of the time-ordered GF is given by all possible combinations of Green's function lines (G_0) and self-energy diagrams. In self-consistent schemes like the GW approximation the self-energy is defined by the full GF G and not G_0. Self-consistent schemes therefore include additional diagrams where the Green's function lines themselves have self-energy insertions.

The retarded Green's function obeys a Dyson equation identical to the one above with the time-ordered quantities replaced by their retarded counter parts. In Fourier space this leads to the following solution for the retarded Green's function

$$G^r(\varepsilon) = \left[\varepsilon - H_0 - \Sigma^r(\varepsilon) \right]^{-1}, \tag{C.15}$$

where H_0 denotes the single-particle Hartree Hamiltonian.

References

[1] International Technology Roadmap for Semiconductors, `http://public.itrs.net`.

[2] G. D. Wilk, R. M. Wallace, and J. M. Anthony, High-κ dielectrics: Current status and materials properties considerations, J. Appl. Phys. **89**(10), 5243 (2001).

[3] A. Javey, H. Kim, M. Brink, Q. Wang, A. Ural, J. Guo, P. McIntyre, P. McEuen, M. Lundstrom, and H. J. Dai, High-κ dielectrics for advanced carbon-nanotube transistors and logic gates, Nature Mat. **1**, 241 (2002).

[4] D. Natelson, Single-molecule transistors, in *Handbook of Organic Electronics and Photonics*, edited by H. S. Nalwa, volume 3, pages 1–49, American Scientific Publishers, Stevenson Ranch, CA, 2007.

[5] Z. Bao and J. Locklin, *Organic Field-Effect Transistors*, CRC Press, Boca Raton, 2007.

[6] E. C. P. Smits, S. G. J. Mathijssen, P. A. van Hal, S. Setayesh, T. C. T. Geuns, K. A. H. A. Mutsaers, E. Cantatore, H. J. Wondergem, O. W., R. Resel, M. Kemerink, S. Kirchmeyer, A. M. Muzafarov, S. A. Ponomarenko, B. de Boer, and P. W. M. B. . D. M. de Leeuw, Bottom-up organic integrated circuits, Nature **455**, 956 (2008).

[7] S. J. Tans, A. R. M. Verschueren, and C. Dekker, Room-temperature transistor based on a single carbon nanotube, Nature **393**, 49 (1998).

[8] J. Xiang, W. Lu, Y. Hu, Y. Wu, H. Yan, and C. M. Lieber, Ge/Si nanowire heterostructures as high-performance field-effect transistors, Nature **441**, 489 (2006).

[9] Y. Li, F. Qian, J. Xiang, and C. Lieber, Nanowire electronic and optoelectronic devices, Materials Today **9**, 18 (2006).

[10] A. Aviram and M. A. Ratner, Molecular rectifiers, Chem. Phys. Lett. **29**, 277 (1974).

[11] H. Park, J. Park, A. K. L. Lim, E. H. Anderson, A. P. Alivisatos, and P. L. McEuen, Nanomechanical oscillations in a single-C60 transistor, Nature **407**, 57 (2000).

[12] N. P. Guisinger, N. L. Yoder, and M. C. Hersam, Probing charge transport at the single-molecule level on silicon by using cryogenic ultra-high vacuum scanning tunneling microscopy, Proc. Natl. Acad. Sci. **102**, 8838 (2005).

[13] S. Y. Quek, J. B. Neaton, M. S. Hybertsen, E. Kaxiras, , and S. G. Louie, Negative differential resistance in transport through organic molecules on silicon, Phys. Rev. Lett. **98**, 066807 (2007).

[14] A. V. Danilov, S. E. Kubatkin, S. G. Kafanov, K. Flensberg, and T. Bjørnholm, Electron transfer dynamics of bistable single-molecule junctions, Nano. Lett. **6**, 2184 (2006).

[15] A. V. Danilov, P. Hedegård, D. S. Golubev, T. Bjønholm, and S. E. Kubatkin, Nanoelectromechanical switch operating by tunneling of an entire C_{60} molecule, Nano. Lett. **8**, 2393 (2008).

[16] J. Repp, G. Meyer, S. M. Stojković, A. Gourdon, and C. Joachim, Molecules on insulating films: Scanning-tunneling microscopy imaging of individual molecular orbitals, Phys. Rev. Lett. **94**, 026803 (2005).

[17] L. Gross, F. Mohn, N. Moll, P. Liljeroth, and G. Meyer, The chemical structure of a molecule resolved by atomic force microscopy, Science **325**, 1110 (2009).

[18] D. M. Cardamone, C. A. Stafford, and S. Mazumdar, Controlling quantum transport through a single molecule, Nano. Lett. **6**, 2422 (2006).

[19] D. Darau, G. Begemann, A. Donarini, and M. Grifoni, Interference effects on the transport characteristics of a benzene single-electron transistor, Phys. Rev. B **79**, 235404 (2009).

[20] S. Kubatkin, A. Danilov, M. Hjort, J. Cornil, J.-L. Brédas, N. S.-Hansen, P. Hedegård, and T. Bjørnholm, Single-electron transistor of a single organic molecule with access to several redox states, Nature **425**, 698 (2003).

[21] S. J. Tans, M. H. Devoret, H. Dai, A. Thess, R. E. Smalley, L. J. Geerligs, and C. Dekker, Individual single-wall carbon nanotubes as quantum wires, Nature **386**, 474 (1997).

[22] D. H. Cobden, M. Bockrath, P. L. McEuen, A. G. Rinzler, and R. E. Smalley, Spin splitting and even-odd effects in carbon nanotubes, Phys. Rev. Lett. **81**, 681 (1998).

[23] S. D. Franceschi, J. A. van Dam, E. P. A. M. Bakkers, L. F. Feiner, L. Gurevich, and L. P. Kouwenhoven, Single-electron tunneling in InP nanowires, Appl. Phys. Lett. **83**, 344 (2003).

[24] C. Thelander, T. Mårtensson, M. T. Björk, B. J. Ohlsson, M. W. Larsson, L. R. Wallenberg, and L. Samuelson, Single-electron transistors in heterostructure nanowires, Appl. Phys. Lett. **83**, 2052 (2003).

[25] C. Stampfer, E. Schurtenberger, F. Molitor, J. Güttinger, T. Ihn, and K. Ensslin, Tunable Graphene Single Electron Transistor, Nano. Lett. **8**, 2378 (2008).

[26] W. Lu, Z. Ji, L. Pfeiffer, K. W. West, and A. J. Rimberg, Real-time detection of electron tunnelling in a quantum dot, Nature **423**, 422 (2003).

[27] L. P. Kouwenhoven, D. G. Austing, and S. Tarucha, Few-electron quantum dots, Rep. Prog. Phys. **64**, 701 (2001).

[28] J. M. Thijssen and H. S. J. van der Zant, Charge transport and single-electron effects in nanoscale systems, Phys. Stat. Sol. (B) **245**, 1455 (2008).

[29] D. Natelson, L. H. Yu, J. W. Ciszek, Z. K. Keane, and J. M. Tour, Single-molecule transistors: Electron transfer in the solid state, Chemical Physics **324**, 267 (2006).

[30] C. H. Ahn, A. Bhattacharya, M. D. Ventra, J. N. Eckstein, C. D. Frisbie, M. E. Gershenson, A. M. Goldman, I. H. Inoue, J. Mannhart, A. J. Millis, A. F. Morpurgo, D. Natelson, and J.-M. Triscone, Electrostatic modification of novel materials, Rev. Mod. Phys. **78**, 1185 (2006).

[31] E. A. Osorio, T. Bjørnholm, J.-M. Lehn, M. Ruben, and H. S. J. van der Zant, Single-molecule transport in three-terminal devices, J. Phys.: Condens. Matter **20**, 374121 (2008).

[32] K. Moth-Poulsen and T. Bjørnholm, Molecular electronics with single molecules in solid-state devices, Nature Nanotech. **4**, 551 (2009).

[33] D. R. Strachan, D. E. Johnston, B. S. Guiton, S. S. Datta, P. K. Davies, D. A. Bonnell, and A. T. C. Johnson, Real-time TEM imaging of the formation of crystalline nanoscale gaps, Phys. Rev. Lett. **100**, 056805 (2008).

[34] A. R. Champagne, A. N. Pasupathy, and D. C. Ralph, Mechanically adjustable and electrically gated single-molecule transistors, Nano. Lett. **5**, 305 (2005).

[35] R. H. M. Smit, Y. Noat, C. Untiedt, N. D. Lang, M. C. van Hemert, and J. M. van Ruitenbeek, Measurement of the conductance of a hydrogen molecule, Nature **419**, 906 (2002).

[36] A. Danilov, S. Kubatkin, S. Kafanov, P. Hedegård, N. Stuhr-Hansen, K. Moth-Poulsen, and T. Bjørnholm, Electronic transport in single molecule junctions: Control of the molecule-electrode coupling through intramolecular tunneling barriers, Nano. Lett. **8**(1), 1 (2008).

[37] T. Dadosh, Y. Gordin, R. Krahne, I. Kivrich, D. Mahalu, V. Frydman, J. Sperling, A. Yacoby, and I. Bar-Joseph, Measurement of the conductance of single conjugated molecules, Nature **436**, 677 (2005).

[38] F. Chen, J. He, C. Nuckolls, T. Roberts, J. E. Klare, and S. Lindsay, A molecular switch based on potential-induced changes of oxidation state, Nano. Lett. **5**, 503 (2005).

[39] F. Chen, C. Nuckolls, and S. Lindsay, In situ measurements of oligoaniline conductance: Linking electrochemistry and molecular electronics, Chemical Physics **324**, 236 (2006).

[40] X. Li, B. Xu, X. Xiao, X. Yang, L. Zang, and N. Tao, Controlling charge transport in single molecules using electrochemical gate, Faraday Discuss. **131**, 111 (2006).

[41] D. Ward, N. Grady, C. Levin, N. Halas, Y. Wu, P. Nordlander, , and D. Natelson, Electromigrated nanoscale gaps for surface-enhanced Raman spectroscopy, Nano. Lett. **7**, 1396 (2007).

[42] D. R. Ward, N. J. Halas, J. W. Ciszek, J. M. Tour, Y. Wu, P. Nordlander, and D. Natelson, Simultaneous measurements of electronic conduction and raman response in molecular junctions, Nano. Lett. **8**, 919 (2008).

[43] R. Hesper, L. H. Tjeng, and G. A. Sawatzky, Strongly reduced band gap in a correlated insulator in close proximity to a metal, Europhys. Lett. **40**(2), 177 (1997).

[44] R. A. Marcus, On the theory of oxidation-reduction reactions involving electron transfer. I, J. Chem. Phys. **24**, 966 (1956).

[45] M. Pope and C. E. Swenberg, *Electronic Processes in Organic Crystals and Polymers*, Oxford University Press, Oxford, 1999.

[46] H. B. Heersche, Z. de Groot, J. A. Folk, H. S. J. van der Zant, C. Romeike, M. R. Wegewijs, L. Zobbi, D. Barreca, E. Tondello, and A. Cornia, Electron transport through single Mn_{12} molecular magnets, Phys. Rev. Lett. **96**, 206801 (2006).

[47] M.-H. Jo, J. E. Grose, K. Baheti, M. M. Deshmukh, J. J. Sokol, E. M. Rumberger, D. N. Hendrickson, J. R. Long, H. Park, , and D. C. Ralph, Signatures of molecular magnetism in single-molecule transport spectroscopy, Nano. Lett. **6**, 2014 (2006).

[48] J. E. Grose, E. S. Tam, C. Timm, M. Scheloske, B. Ulgut, J. J. Parks, H. D. Abruña, W. Harneit, and D. C. Ralph, Tunnelling spectra of individual magnetic endofullerene molecules, Nature Mat. **7**, 884 (2008).

[49] E. A. Osorio, K. O'Neill, M. Wegewijs, N. Stuhr-Hansen, J. Paaske, T. Bjørnholm, and H. S. J. van der Zant, Electronic excitations of a single molecule contacted in a three-terminal configuration, Nano. Lett. **7**(11), 3336 (2007).

[50] E. A. Osorio, K. O'Neill, N. Stuhr-Hansen, O. F. Nielsen, T. Bjørnholm, and H. S. J. van der Zant, Addition energies and vibrational fine structure measured in electromigrated single-molecule junctions based on an oligophenylenevinylene derivative, Adv. Mater. **19**(2), 281 (2007).

[51] A. N. P. J. Park, J. I. Goldsmith, C. Chang, Y. Yaish, J. R. Petta, M. Rinkoski, J. P. Sethna, H. D. Abruña, and P. L. McEuen, Coulomb blockade and the Kondo effect in single-atom transistors, Nature **417**, 722 (2002).

[52] L. H. Yu and D. Natelson, The Kondo effect in C_{60} single-molecule transistors, Nano. Lett. **4**, 79 (2004).

[53] S. Braig and K. Flensberg, Vibrational sidebands and dissipative tunneling in molecular transistors, Phys. Rev. B **68**, 205324 (2003).

[54] J. Koch, F. von Oppen, and A. V. Andreev, Theory of the Franck-Condon blockade regime, Phys. Rev. B **74**, 205438 (2006).

[55] H. Bruus and K. Flensberg, *Many-Body Quantum Theory in Condensed Matter Physics: An Introduction*, Oxford University Press, Oxford, 2004.

[56] S. Lakshmi, S. Dutta, and S. K. Pati, Molecular Electronics: Effect of external electric field, J. Phys. Chem. C **112**, 14718 (2008).

[57] L. D. Hallam, J. Weis, and P. A. Maksym, Screening of the electron-electron interaction by gate electrodes in semiconductor quantum dots, Phys. Rev. B **53**, 1452 (1996).

[58] P. Hedegård and T. Bjørnholm, Charge transport through image charged stabilized states in a single molecule single electron transistor device, Chemical Physics **319**, 350 (2005).

[59] J. D. Sau, J. B. Neaton, H. J. Choi, S. G. Louie, and M. L. Cohen, Electronic energy levels of weakly coupled nanostructures: C_{60}-metal interfaces, Phys. Rev. Lett. **101**, 026804 (2008).

[60] R. Stadler, V. Geskin, and J. Cornil, Screening effects in a density functional theory based description of molecular junctions in the Coulomb blockade regime, Phys. Rev. B **79**, 113408 (2009).

[61] A. C. Maggs and R. Everaers, Simulating nanoscale dielectric response, Phys. Rev. Lett. **96**, 230603 (2006).

[62] J. D. Jackson, *Classical Electrodynamics*, John Wiley & Sons, New York, 2 edition, 1975.

[63] P. Fulde, *Electron Correlations in Molecules and Solids*, Number 100 in Springer Series in Solid-State Sciences, Springer, Berlin, 3 edition, 1995.

[64] T. Ihn, *Electronic Quantum Transport in Mesoscopic Semiconductor Structures*, Springer, New York, 2004.

[65] FEniCS, FEniCS Project, `http//www.fenics.org/`, 2007.

[66] Y. Saad, *Iterative methods for sparse linear systems*, SIAM, 2 edition, 2003.

[67] J. S. Seldenthuis, H. S. J. van der Zant, M. A. Ratner, and J. M. Thijssen, Vibrational excitations in weakly coupled single-molecule junctions: A computational analysis, ACS Nano **2**(7), 1445 (2008).

[68] S. C. Lam and R. J. Needs, First-principles calculation of the screening of electric fields at the aluminium(111) and (110) surfaces, J. Phys.: Condens. Matter **5**(14), 2101 (1993).

[69] E. V. Chulkov, V. M. Silkin, and P. M. Echenique, Image potential states on metal surfaces: binding energies and wave functions, Surf. Sci. **437**, 330 (1999).

[70] S. S. Datta, D. R. Strachan, and A. T. C. Johnson, Gate coupling to nanoscale electronics, Phys. Rev. B **79**, 205404 (2009).

[71] V. M. Geskin, J. Cornil, and J. L. Brédas, Comment on 'Polaron formation and symmetry breaking' by L. Zuppiroli et al., Chem. Phys. Lett. **403**, 228 (2005).

[72] W. Barford, R. J. Bursill, and M. Y. Lavrentiev, Density matrix renormalization group calculations of the low-lying excitations and nonlinear optical properties of poly(para-phenylene), J. Phys.: Condens. Matter **10**, 6429 (1998).

[73] X.-Y. Zhu, Charge transport at metal-molecule interfaces: A spectroscopic view, J. Phys. Chem. B **108**(26), 8778 (2004).

[74] E. V. Tsiper, Z. G. Soos, W. Gao, and A. Kahn, Electronic polarization at surfaces and thin films of organic molecular crystals: PTCDA, Chem. Phys. Lett. **360**, 47 (2002).

[75] X. Lu, M. Grobis, K. H. Khoo, S. G. Louie, and M. F. Crommie, Charge transfer and screening in individual C_{60} molecules on metal substrates: A scanning tunneling spectroscopy and theoretical study, Phys. Rev. B **70**, 115418 (2004).

[76] J. B. Neaton, M. S. Hybertsen, and S. G. Louie, Renormalization of molecular electronic levels at metal-molecule interfaces, Phys. Rev. Lett. **97**, 216405 (2006).

[77] C. Freysoldt, P. Rinke, and M. Scheffler, Controlling polarization at insulating surfaces: Quasiparticle calculations for molecules adsorbed on insulator films, Phys. Rev. Lett. **103**, 056803 (2009).

[78] J. M. Garcia-Lastra, A. Rubio, and K. S. Thygesen, Image charge effects and level alignment at solid-molecule interfaces, unpublished (2009).

[79] K. S. Thygesen and A. Rubio, Renormalization of molecular quasiparticle levels at metal-molecule interfaces: Trends across binding regimes, Phys. Rev. Lett. **102**, 046802 (2009).

[80] J. C. Inkson, Many-body effects at metal-semiconductor junctions: II. The self energy and band structure distortion, J. Phys. C **6**, 1350 (1973).

[81] J. P. A. Charlesworth, R. W. Godby, and R. J. Needs, First-principles calculations of many-body band-gap narrowing at an Al/GaAs(110) interface, Phys. Rev. Lett. **70**(11), 1685 (1993).

[82] D. O. Demchenko and L.-W. Wang, Localized electron states near a metal/semiconductor nanocontact, Nano. Lett. **7**(10), 3219 (2007).

[83] J.-W. van der Horst, P. A. Bobbert, M. A. J. Michels, G. Brocks, and P. J. Kelly, Ab initio calculation of the electronic and optical excitations in polythiophene: Effects of intra- and interchain screening, Phys. Rev. Lett. **83**, 4413 (1999).

[84] Y. Li, D. Lu, and G. Galli, Calculation of quasi-particle energies of aromatic self-assembled monolayers on Au(111), J. Chem. Theory Comput. **5**, 881 (2009).

[85] L. Hedin, New method for calculating the one-particle Green's function with application to the electron-gas problem, Phys. Rev. **139**, A796 (1965).

[86] L. Hedin and S. Lundquist, Effects of Electron-Electron and Electron-Phonon Interactions on the One-Electron States of Solids, in *Solid State Physics*, edited by F. Seitz, D. Turnbull, and H. Ehrenreich, volume 23, page 1, Academic Press, New York, 1969.

[87] G. Baym and L. P. Kadanoff, Conservation Laws and Correlatoin Functions, Phys. Rev. **124**(2), 287 (1961).

[88] G. Baym, Self-consistent approximations in many-body systems, Phys. Rev. **127**(4), 1391 (1962).

[89] L. Kadanoff and G. Baym, *Quantum Statistical Mechanics*, W. A. Benjamin, New York, 1962.

[90] B. Holm and U. von Barth, Fully self-consistent GW self-energy of the electron gas, Phys. Rev. B **57**, 2108 (1998).

[91] G. Pal, Y. Pavlyukh, H. C. Schneider, and W. Hübner, Conserving quasiparticle calculations for small metal clusters, Eur. Phys. J. B **70**, 483 (2009).

[92] W. G. Aulbur, L. Jonsson, and J. W. Wilkins, Quasiparticle calculations in solids, in *Solid State Physics*, edited by H. Ehrenreich and F. Saepen, volume 54, page 1, Academic Press, New York, 2000.

[93] F. Aryasetiawan and O. Gunnarsson, The GW method, Rep. Prog. Phys. **61**, 237 (1998).

[94] G. Onida, L. Reining, and A. Rubio, Electronic excitations: density-functional versus many-body Green's-function approaches, Rev. Mod. Phys. **74**, 601 (2002).

[95] N. Lang and W. Kohn, Theory of metal surfaces: Induced surface charge and image potential, Phys. Rev. B **7**, 3541 (1973).

[96] J. C. Grossman, M. Rohlfing, L. Mitas, S. G. Louie, and M. L. Cohen, High Accuracy Many-Body Calculational Approaches for Excitations in Molecules, Phys. Rev. Lett. **86**, 472 (2001).

[97] A. Stan, N. E. Dahlen, and R. van Leeuwen, Fully self-consistent GW calculations for atoms and molecules, Europhys. Lett. **76**, 298 (2006).

[98] M. L. Tiago, P. R. C. Kent, R. Q. Hood, and F. A. Reboredo, Neutral and charged excitations in carbon fullerenes from first-principles many-body theories, J. Chem. Phys. **129**, 084311 (2008).

[99] C. D. Spataru, S. Ismail-Beigi, X. L. Benedict, and S. G. Louie, Excitonic Effects and Optical Spectra of Single-Walled Carbon Nanotubes, Phys. Rev. Lett. **92**, 077402 (2004).

[100] P. E. Trevisanutto, C. Giorgetti, L. Reining, M. Ladisa, and V. Olevano, Ab initio GW many-body effects in graphene, Phys. Rev. Lett. **101**, 226405 (2008).

[101] M. L. Tiago and J. R. Chelikowsky, Optical excitations inorganic molecules, clusters, and defects studied by first-principles Green's function methods, Phys. Rev. B **73**, 205334 (2006).

[102] P. H. Hahn, W. G. Schmidt, and F. Bechstedt, Molecular electronic excitations calculated from a solid-state approach: Methodology and numerics, Phys. Rev. B **72**, 245425 (2005).

[103] C. Verdozzi, R. W. Godby, and S. Holloway, Evaluation of GW approximations for the self-energy of a Hubbard cluster, Phys. Rev. Lett. **74**, 2327 (1995).

[104] T. J. Pollehn, A. Schindlmayr, and R. W. Godby, Assessment of the GW approximation using Hubbard chains, J. Phys.: Condens. Matter **10**, 1273 (1998).

[105] A. Schindlmayr, T. T. Pollehn, and R. W. Godby, Spectra and total energies from self-consistent many-body perturbation theory, Phys. Rev. B **58**, 12684 (1998).

[106] M. P. von Friesen, C. Verdozzi, and C.-O. Almbladh, Successes and failures of Kadanoff-Baym dynamics in Hubbard nanoclusters, Phys. Rev. Lett. **103**, 176404 (2009).

[107] J. A. Pople, Electron interaction in unsaturated hydrocarbons, Trans. Faraday Soc. **49**, 1375 (1953).

[108] R. Pariser and R. G. Parr, A semi-empirical theory of the electronic spectra and electronic structure of complex unsaturated molecules .2, J. Chem. Phys. **21**(5), 466 (1953).

[109] R. Pariser and R. G. Parr, A semi-empirical theory of the electronic spectra and electronic structure of complex unsaturated molecules .2, J. Chem. Phys. **21**(5), 767 (1953).

[110] K. Ohno, The present status of the theory of molecular electronic structure - Semiempirical methods, Theor. Chim. Acc. **2**, 219 (1964).

[111] I. R. Ducasse, T. E. Miller, and Z. G. Soos, Correlated states in finite polyenes: Exact PPP results, J. Chem. Phys. **76**, 4094 (1982).

[112] W. Barford and R. J. Bursill, Theory of molecular excitons in the phenyl-based organic semiconductors, Chem. Phys. Lett. **268**, 535 (1997).

[113] R. J. Bursill, C. Castleton, and W. Barford, Optimal parametrisation of the Pariser-Parr-Pople model for benzene and biphenyl, Chem. Phys. Lett. **294**, 305 (1998).

[114] W. Barford, R. J. Bursill, and M. Y. Lavrentiev, Density matrix renormalization group calculations of the low-lying excitations and nonlinear optical properties of poly (*para*-phenylene), J. Phys.: Condens. Matter **10**, 6429 (1998).

[115] M. Y. Lavrentiev, W. Barford, S. J. Martin, and H. Daly, Theoretical investigation of the low-lying electronic structure of poly(*p*-phenylene vinylene), Phys. Rev. B **59**(15), 9987 (1999).

[116] S. Yamada, T. Imamura, and M. Machida, 16.447 TFlops and 159-billion-dimensional exact-diagonalization for trapped fermion-Hubbard model on the Earth Simulator, SC Conference **0**, 44 (2005).

[117] P. Dayal, M. Troyer, and R. Villiger, The Iterative Eigensolver Template Library (IETL), `http://www.comp-phys.org/software/ietl/`.

[118] J. K. Cullum and R. A. Willoughby, *Lanczos Algorithms for Large Symmetric Eigenvalue Computations*, volume 1, SIAM, 2002.

[119] E. Dagotto, Correlated electrons in high-temperature superconductors, Rev. Mod. Phys. **66**(3), 763 (1994).

[120] K. S. Thygesen and A. Rubio, Conserving GW scheme for nonequilibrium quantum transport in molecular contacts, Phys. Rev. B **77**, 115333 (2008).

[121] A. L. Fetter and J. D. Walecka, *Quantum theory of many-particle systems*, McGraw-Hill, New York, 1971.

[122] K. Schönhammer, O. Gunnarsson, and R. M. Noack, Density-functional theory on a lattice: Comparison with exact numerical results for a model with strongly correlated electrons, Phys. Rev. B **52**, 2504 (1995).

[123] K. S. Thygesen and A. Rubio, Nonequilibrium GW approach to quantum transport in nano-scale contacts, J. Chem. Phys. **126**, 091101 (2007).

[124] P. Darancet, A. Ferretti, D. Mayou, and V. Olevano, Ab initio GW electron-electron interaction effects in quantum transport, Phys. Rev. B **75**, 075102 (2007).

[125] P. S. Damle, A. W. Ghosh, and S. Datta, Unified description of molecular conduction: From molecules to metallic wires, Phys. Rev. B **64**, 201403 (2001).

[126] J. Taylor, M. Brandbyge, and K. Stokbro, Theory of rectification in tour wires: The role of electrode coupling, Phys. Rev. Lett. **89**, 138301 (2002).

[127] K. S. Thygesen and K. W. Jacobsen, Conduction mechanism in a molecular hydrogen contact, Phys. Rev. Lett. **94**, 036807 (2005).

[128] M. D. Ventra, S. T. Pantelides, and N. D. Lang, First-principles calculation of transport properties of a molecular device, Phys. Rev. Lett. **84**, 979 (2000).

[129] Y. Xue and M. A. Ratner, Theoretical principles of single-molecule electronics: A chemical and mesoscopic view, Int. J. Quantum Chem. **102**, 911 (2005).

[130] D. J. Mowbray, G. Jones, and K. S. Thygesen, Influence of functional groups on charge transport in molecular junctions, J. Chem. Phys. **128**, 111103 (2008).

[131] S. Y. Quek, L. Venkataraman, H. J. Choi, S. G. Louie, M. S. Hybertsen, and J. B. Neaton, Amine-gold linked single-molecule circuits: Experiment and theory, Nano. Lett. **7**(11), 3477 (2007).

[132] R. Hoffmann, An Extended Hückel theory. I. Hydrocarbons, J. Chem. Phys. **39**, 1397 (1963).

[133] F. Zahid, M. Paulsson, E. Polizzi, A. W. Ghosh, L. Siddiqui, and S. Datta, A self-consistent transport model for molecular conduction based on extended Hückel theory with full three-dimensional electrostatics, J. Chem. Phys. **123**(6), 064707 (2005).

[134] J. A. Pople and G. A. Segal, Approximate Self-Consistent Molecular Orbital Theory. III. CNDO Results for AB_2 and AB_3 Systems, J. Chem. Phys. **44**, 3289 (1966).

[135] J. M. Sichel and M. A. Whitehead, Semi-Empirical All Valence Electrons SCF-LCAO-MO Theory, Theor. Chim. Acc. **11**, 220 (1968).

Paper I

NANO LETTERS

2008
Vol. 8, No. 11
3809-3814

Strong Polarization-Induced Reduction of Addition Energies in Single-Molecule Nanojunctions

Kristen Kaasbjerg* and Karsten Flensberg

Nano-Science Center, Niels Bohr Institute, University of Copenhagen, DK-2100 Copenhagen, Denmark

Received July 18, 2008; Revised Manuscript Received September 22, 2008

ABSTRACT

We address polarization-induced renormalization of molecular levels in solid-state based single-molecule transistors and focus on an organic conjugate molecule where a surprisingly large reduction of the addition energy has been observed. We have developed a scheme that combines a self-consistent solution of a quantum chemical calculation with a realistic description of the screening environment. Our results indeed show a large reduction, and we explain this to be a consequence of both (a) a reduction of the electrostatic molecular charging energy and (b) polarization induced level shifts of the HOMO and LUMO levels. Finally, we calculate the charge stability diagram and explain at a qualitative level general features observed experimentally.

The recent experimental progress in single-molecule electronics has resulted in the realization of the three-terminal molecular single-electron transistor (SET)[1−10] shown schematically in Figure 1a. The experimental realizations have been based on a variety of techniques including junctions made by electromigration, mechanical break junctions, and cryogenic nanogap fabrication. Many indications of the molecule being part of the active transport pathway through the junction has been observed. An example is the observation of the molecular vibrational excitations, which serve as a fingerprint for the molecule.[5,11] However, there remain several unresolved issues in single-molecule transport both in the strong coupling limit, where coherent transport theories seems to strongly overestimate the current level, as well as in the weak coupling regime, where the observed energy gaps are much smaller than expected. Experiments on organic molecules have shown that the so-called addition energy, which is the difference between the molecular ionization potential (IP) and the electron affinity (EA), is heavily reduced compared to its gas phase value in single-molecule SETs.[3,5,8]

Reductions of the excitation gaps are well known from other situations. Theoretical studies of semiconductor/metal interfaces have shown that the band gap of the semiconductor is narrowed near the interface by the screening in the metal.[12,13] Experiments using photoemission techniques and scanning tunneling spectroscopy to study the electronic structure of single molecules, self-assembled monolayers, and organic thin films on dielectric and metal surfaces have shown similar effects.[14−19] The experimental settings of a single-molecule SET is to some degree analogous to the situation in electrochemical measurements where the equivalent of the addition energy, the electrochemical gap, is well known to depend on the dielectric properties of the surrounding media.[20] However, the screening environments are rather different for the electrochemical setup and the single-molecule transistor geometry with one being in ionic solutions or organic solvents and the other in solid state low temperature environment. A direct comparison is therefore not possible in general.

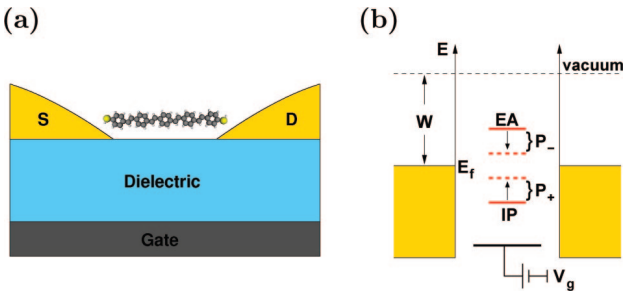

Figure 1. (a) Schematic illustration of a three-terminal single-molecule transistor. (b) Energy level alignment in the molecular junction showing the position of the molecular ionization potential (IP) and electron affinity (EA) levels with respect to the work functions of the metallic leads. Also the gate electrode with voltage V_g which couples to EA and IP is schematically shown. The polarization shifts P_+ and P_- of the levels due to the junction environment are indicated.

It has been suggested that the reduction of the addition energy seen in single-molecule SETs is caused by polariza-

* To whom correspondence should be addressed.

10.1021/nl8021708 CCC: $40.75
Published on Web 10/28/2008

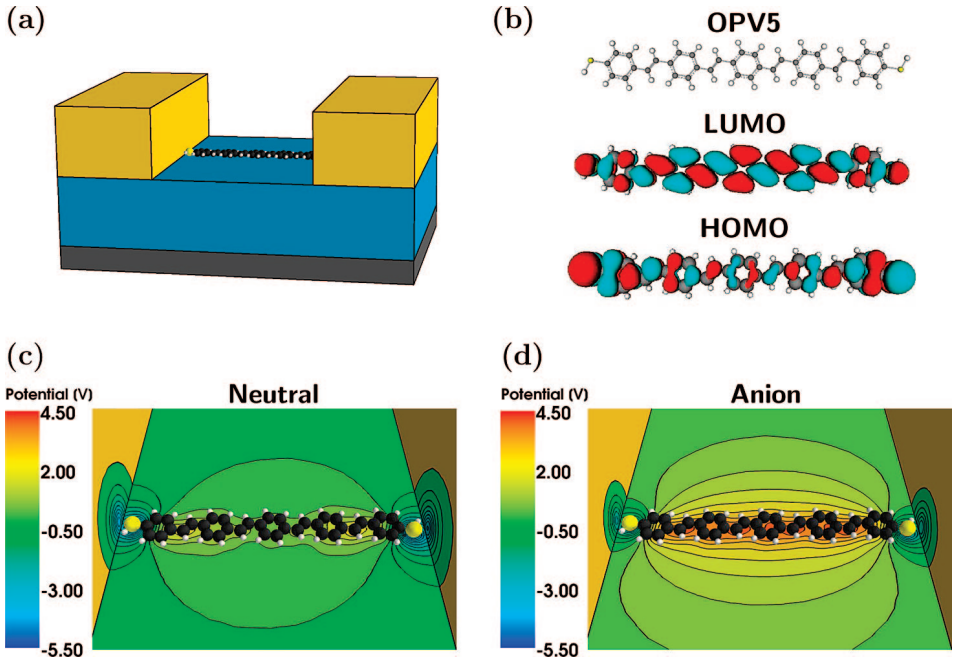

Figure 2. (a) Illustration of the simulated OPV5-SET with the molecule lying flat on the Al_2O_3 gate oxide between the source and drain electrodes. (b) Molecular structure of OPV5 and isosurface plots (blue, negative; red, positive) of the HOMO and LUMO orbitals for the isolated molecule. (c,d) Polarization response of the nanojunction illustrated by contour plots of the induced potential from the polarization charge at the dielectric and electrode interfaces for the neutral molecule (panel c) and for the anion (panel d). Because of its partially positive-charged thiol groups the overall neutral OPV5 molecule induces a negative potential in the nearby electrodes and dielectric that reduces the HOMO−LUMO gap (see text). The additional electron of the anion results in a significant polarization of the gate dielectric which reduces the charging energy of the molecule.

tion/image charges in the metallic electrodes,[3,21] giving rise to a localization of the charges near the metallic electrodes. Theoretically only a few other studies have addressed the polarization-induced renormalization of the molecular levels in solid state environments and its implications for the electron transport in molecular junctions,[22−25] and the situation is still very much debated. Therefore, a more realistic and quantitative theoretical description of the surprisingly large effect is called for. The purpose of the present letter is to fill out this gap and study the influence of the junction environment on the positions of the molecular levels in a realistic single-molecule SET. We have developed a scheme that includes the polarizable environment in a quantum chemical calculation, in which the polarization response of the environment and the molecular charge distribution is determined self-consistently. Our calculations on the conjugated organic molecule used in experiments[3,5] show that a large part of the reduction of the addition energy can be accounted for by polarization of the environment. By using a simplified expression for the addition energy, the reduced addition energy can be understood in terms screening of the charging energy of the molecule and a closing of the HOMO−LUMO gap.

For a single-molecule SET operating in the Coulomb blockade regime, that is, with a weak tunnel coupling between the molecule and the source/drain electrodes, sequential tunneling is the dominating transport mechanism. In this regime, charge transfer through the molecule is possible when either the IP or the EA is positioned within the bias window. If on the other hand no levels are present in the bias window, current is blocked and the molecule remains in a fixed charged state. To reach the regime where transport is possible, one can either shift the IP and EA levels with the gate-voltage or apply a sufficiently large source-drain bias. This results in a so-called charge stability diagram that maps out the molecular charged states as a function of source-drain and gate voltage (see, e.g., Figure 4). The addition energy U can be extracted from this diagram by measuring the height of the central diamond. Since the ionization potential and the electron affinity are given by the difference in total energy between the neutral molecule (with N electrons) and the cation ($N - 1$) and anion ($N + 1$), respectively

$$\mathrm{IP} = E^{N-1} - E^{N} \quad \text{and} \quad \mathrm{EA} = E^{N} - E^{N+1} \tag{1}$$

the addition energy can be expressed as

$$U = \mathrm{IP} - \mathrm{EA} = E^{N+1} + E^{N-1} - 2E^{N} \tag{2}$$

When the molecule is placed in a nanojunction, charging of the molecule induces polarization charge in the junction environment. The formation of the polarization charge is associated with stabilizing polarization energies P_+ (added hole) and P_- (added electron) for the cation and anion, respectively,[15] which shifts the IP and EA relative to their gas phase values as illustrated in Figure 1b. The resulting reduction of the addition energy is given by the sum $P = P_+ + P_-$, i.e., $U = \mathrm{IP(g)} - \mathrm{EA(g)} - P$. Naturally, the polarization energy P depends on the screening properties and response times of the environment. In single-molecule SETs where the typical current level is on the order of $I \sim$ pA − nA, the polarization response of the metallic electrodes and gate dielectric (given by the plasmon frequency $\sim 10^{15}$

s^{-1} and the phonon frequency $\sim 10^{13}$ s^{-1}, respectively) is orders of magnitudes faster than the tunneling rate $\Gamma = I/e \sim 10^7 - 10^{10}$ s^{-1} for electrons, implying that the polarization energy is given by the full static response of the environment.

In the Supporting Information, we have provided a general framework for evaluating total energies of nanoscale systems in the presence of a polarizable environment. The main assumption of our approach is that the polarizable environment responds instantaneously to changes in the charge state of the molecule, which according to the above consideration is a reasonable assumption for single-molecule SETs. An electrostatic treatment of the environment hence suffices and we derive the following effective Hamiltonian for the nanojunction

$$H = H_s + H_{pol} + H_{ext} \tag{3}$$

where H_s is the Hamiltonian of a general nanoscale system (in our case a molecule),

$$H_{pol} = \int dr\, \rho_s(r)\Phi_{ind}(r) - \frac{1}{2}\int dr\, \langle \rho_s(r)\rangle \Phi_{ind}(r) \tag{4}$$

describes the interaction between the molecular charge distribution ρ_s and the polarization charge through the induced potential Φ_{ind}, and

$$H_{ext} = \int dr\, \rho_s(r)\Phi_{ext}(r) \tag{5}$$

accounts for external voltages applied to the gate, source, and drain electrodes. The external potential Φ_{ext} satisfies Laplace equation with boundary conditions given by the applied voltages on the electrodes. The induced potential Φ_{ind} can be obtained via a solution to Poisson's equation

$$-\nabla \cdot [\varepsilon_r(r)\nabla \Phi(r)] = 4\pi\rho_s(r) \tag{6}$$

for the potential $\Phi = \Phi_s + \Phi_{ind}$, where ε_r is the dielectric constant of the environment and Φ_s the potential from the molecular charge distribution. The present approach thus allows for a continuum description of the environment combined with a quantum chemical treatment (e.g., DFT or Hartree−Fock) of the molecule. In order to account for the molecular charge redistribution due to the polarization response of the environment the induced potential must be included in the usual self-consistent cycle of e.g. DFT calculations.

In the present work a semiempirical method has been combined with a finite element treatment of Poisson's equation (see Supporting Information for details). We note that the addition energy we calculate for the isolated OPV5 molecule (see below), is underestimated with 1.2 eV as compared to the DFT value using the B3LYP exchange-correlation functional. Despite this fact, we still expect the polarization energies to be accurate, since the interaction with the polarization charge is treated correctly in our approach. That this is indeed the case has been confirmed by comparison with other methods.[22]

We apply here our method to a single-molecule SET based on the thiol-terminated OPV5 molecule, which is an organic-conjugated molecule consisting of alternating phenylene and vinylene groups (see Figure 2b). In experimental realizations of OPV5-based SETs both heavily reduced addition energies, access to several redox states, molecular vibrational excitations and Kondo effect have been observed.[3,5,6] The simulated OPV5-SET is illustrated in Figure 2a with the molecule lying flat on the gate dielectric between the source and drain electrodes, which are separated by a 3.2 nm gap. To resemble experimental settings[3] the gate electrode is separated from the molecule by a 5 nm thick layer of gate oxide with dielectric constant $\varepsilon_r = 10$, corresponding to the high-κ dielectric Al_2O_3. The relatively high dielectric constant of Al_2O_3 ensures a reasonable capacitive coupling between the molecule and the gate electrode. We model the gold electrodes by infinitely high metal blocks. The molecule is placed at a distance of 1 Å from the surfaces of the source/drain electrode and the gate oxide. Since the electrostatic image plane of atomic surfaces is located outside the atomic surface plane,[26,27] this effectively corresponds to a distance between the molecule and the surface atoms on the order of van der Waals distance (~3 Å). In all calculations presented in the following, the molecule has been considered in its neutral-state geometry. Hence, the formation of polarons, i.e., relaxation of the nuclear configuration due to charging of the molecule, is not accounted for.

Table 1. Calculated addition energies, U, single-particle HOMO-LUMO gaps, Δ_{HL}, and polarization energies, P, (all in eV) for the thiol-terminated OPV5-molecule in the three geometries: gas phase (isolated molecule), SET (geometry as in Figure 2a), and gap (molecule placed in the gap between two infinite parallel metal surfaces)

environment	U	Δ_{HL}	P
gas phase	3.27	1.12	
SET	0.68	0.53	2.59
gap	2.08	0.92	1.19

Table 1 summarizes our findings for the addition energy, the gap between the highest occupied and the lowest unoccupied molecular orbital (HOMO–LUMO gap) and finally the polarization energy in the following three environments: (i) gas phase, (ii) as in Figure 2a, and (iii) molecule placed in the gap between two parallel metal surfaces separated by 3.2 nm. The polarization energies due to the presence of the junction environments results in significant reductions of the addition energies relative to their gas phase values.

For further analysis, we shall use the following simplified interpretation of the addition energy: starting with two neutral molecules then U is the energy cost of transferring an electron from one molecule to other (see eq 2). Since this process involves the promotion of an electron from the HOMO in one of the molecules to the LUMO in the other molecule, it is suggestive to write the addition energy as the HOMO−LUMO gap of the neutral molecule, Δ_{HL}, plus two times the Coulomb energy, E_c, required to charge a molecule

$$U = \Delta_{HL} + 2E_c \tag{7}$$

This is similar to the expression for the addition energy in the constant-interaction model, which has been used successfully for conventional quantum dot SETs.[28]

In a naive first guess, one would expect the reduction of U to be mainly a consequence of screening of the charging energy E_c. However, Table 1 shows that also the HOMO−LUMO gaps are reduced in the polarizable environments. The origin

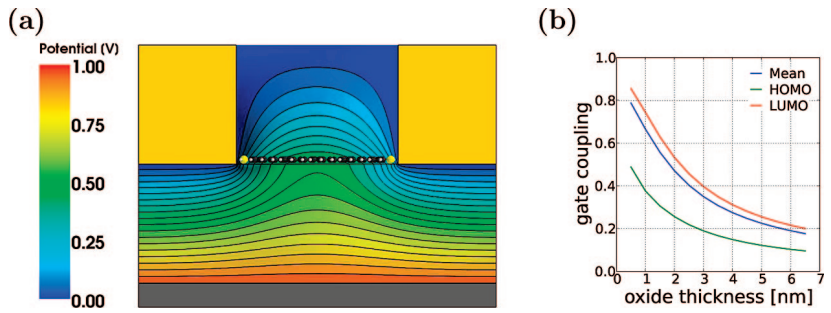

Figure 3. (a) Contour plot of the gate potential for an oxide thickness of 2.5 nm and with 1 V applied to the gate electrode. The metallic electrodes, which are held at 0 V, screen the gate potential significantly which results in a stronger coupling to the central part of the molecule. (b) Gate couplings as a function of oxide thickness. The gate couplings have been calculated as follows: by averaging the potential over the atomic positions of the molecule (Mean); by calculating how much the HOMO and LUMO levels move with 1 V applied to the gate electrode (HOMO and LUMO). The localization of the HOMO on the thiol groups results in a much lower gate coupling compared to the LUMO, which is delocalized over the carbon backbone of the molecule. For an oxide thickness of 5 nm the gate coupling (Mean) of ~0.2 is in good agreement with the value reported experimentally.[3]

of this reduction is illustrated in Figure 2c. Because of the positively charged thiol groups of the overall neutral OPV5, a negative electrostatic potential is induced in the nearby electrodes and dielectric. This, combined with the localization of the HOMO on the thiol groups (see Figure 2b), shifts the HOMO level to higher energy. Similar reasoning for the negatively charged carbon backbone and the LUMO leads to a lowering of the LUMO level and hence a closing of the HOMO−LUMO gap. The charging energy obtained from eq 7 is for OPV5 in gas phase $E_c = 1.08$ eV. The screening response of the nanojunction, which is shown for the OPV5 anion in Figure 2d, reduces this value to $E_c = 75$ meV. To summarize, we can understand the reduction of the addition energy as a consequence of two parallel effects: (i) a reduction of the HOMO−LUMO gap and (ii) screening of the Coulomb repulsion on the molecule which lowers the charging energy. Since the majority of the reduction is due to the latter effect, which is purely electrostatic in nature, the reduction for other molecules of the same size of OPV5 will be comparable. For smaller molecules we have found that the closer proximity of the polarization charge enhances the screening of the charging energy, resulting in larger absolute reductions.

The important role of the gate oxide in the reduction of U is clearly demonstrated by the large difference in the polarization energy between the SET and gap environment in Table 1. More than half of the polarization energy of 2.59 eV in the SET environment is due to the gate oxide. As the molecule is lying flat on the oxide which has almost metallic-like screening properties (the image charge strength of a dielectric surface is $q_{\varepsilon_r} = (\varepsilon_r - 1)/(\varepsilon_r + 1)$), this should come as no surprise. Note that the polarization energy in the SET environment is highly dependent on the dielectric constant of the gate oxide. With a SiO_2 oxide layer ($\varepsilon_r = 3.9$), the polarization energy is reduced to 2.11 eV. We also find that the contribution to the polarization energy from the gate electrode is negligible. The reason for this is its large distance to the molecule together with the fact that the gate electrode only sees the screened charge of the molecule. Even for an oxide thickness of 2−3 nm the gate electrode contributes less than 0.05 eV to the polarization energy.

As mentioned in the introductory part, the molecular levels can be probed by shifting them with the gate voltage or opening the source-drain bias window. Single-molecule SETs therefore provide a useful tool for measuring the energy differences between the molecular levels through the charge stability diagram, albeit in an unnatural environment. We have calculated the charge stability diagram for the OPV5 device (see Figure 4) by evaluating total energies of the neutral, singly charged and doubly charged molecule as a function of gate and source-drain voltage. Our assumption that the molecule remains chemically stable in the considered charge states is in agreement with experimental findings.[3,6] Since we are considering only the ground states of the neutral and charged molecule, the stability diagram contains no lines due to excited states of the molecule. These could be, for example, vibrational excitations which, as mentioned in the introductory part, have been observed experimentally with energies ranging from a few to ~100 meV. Electronic excitations with electrons/holes occupying higher/lower molecular orbitals have energies of hundreds of meV and are therefore harder to observe experimentally. Like the experimentally observed stability diagram,[3] the calculated diagram is characterized by two small diamonds enclosing a big central diamond. The height of the central diamond is seen to be ~0.50 eV instead of 0.68 eV as we found for the zero bias value of the addition energy in Table 1. This is because the HOMO level moves downward with the applied source-drain voltage, and hence decreases the threshold for pulling out an electron from the HOMO. The nonlinear edges on the left side of the central diamond is a result of this effect. The origin of the bias dependent HOMO level can be traced back to a localization of the HOMO near the low energy electrode. The heights of the two smaller diamonds correspond to the addition energies of the anion and cation of the OPV5 molecule, that is

$$U^{N\pm1} = E^N + E^{N\pm2} - 2E^{N\pm1} \tag{8}$$

The small addition energies associated with these states stem from their half-filled frontier orbitals. Therefore, when adding/removing an electron to/from the anion/cation only the charging energy in equation contributes. The resulting

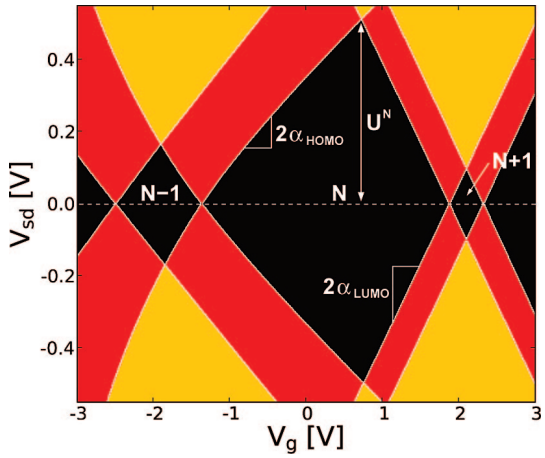

Figure 4. Charge stability diagram for the OPV5-SET. The color indicates the number of levels positioned in the bias window (black, 0; red, 1; yellow, 2) and is hence an indirect measure of the current level for a given gate and source-drain voltage. The Fermi levels of the gold electrodes have been placed in the gap of the molecule as illustrated in Figure 1b. In each of the black diamonds, current is blocked leaving the molecule in the indicated charge states. The addition energies of the charge states of the molecule can be read off from the heights of the respective diamonds.

charging energies are ∼50 and ∼85 meV, respectively, showing that due to the different spatial distributions of the HOMO and LUMO, the charging energy of the cation and anion are not equal, which is implicitly assumed in eq 7.

One important ingredient in understanding the stability diagram is the gate coupling, $\alpha = \partial E_{\mathrm{mol}}/\partial V_{\mathrm{g}}$, that is, how much the energy landscape on the molecule changes when a voltage is applied to the gate electrode. For usual quantum dot devices this is characterized by a single number, which assumes that all states couple equally to the gate. For the OPV5-SET considered here this is not the case. As shown in Figure 3a, the gate potential varies significantly over the extend of the molecule due to screening in the metallic electrodes, which results in a higher gate coupling to the LUMO compared to the HOMO. In the stability diagram this is reflected in the different slopes of the diamond edges, which are given by the gate couplings to the different charged states of the molecule. This has also been observed in a recent experiment.[6] The slopes of the diamond edges agree well with the calculated gate couplings in Figure 3b, where we read off the values $\alpha_{\mathrm{HOMO}} \sim 0.12$ and $\alpha_{\mathrm{LUMO}} \sim 0.25$ for an oxide thickness of 5 nm. The gate coupling of ∼0.2 calculated by averaging the gate potential over the atomic positions of the molecule (denoted Mean in Figure 3b) is in good agreement with the value reported experimentally,[3] indicating that the molecule is positioned directly on the gate oxide as in our simulation. In a situation where the molecule is elevated from the gate oxide, screening of the gate potential due to the source and drain electrodes (see Figure 3a) results in a significantly lower gate coupling.[5,6]

In conclusion, by using a method where a continuum description of the polarizable junction environment is combined with a quantum chemical calculation for the molecule, we have studied the effect of polarization in an OPV5 single-molecule SET. Our results show a significant modification of the addition energy caused by both a closing of the HOMO−LUMO gap and screening of the intramolecular Coulomb interactions. Since the majority of the reduction is due to the latter effect, the reduction obtained here for OPV5, should be general for other molecules of same size. From the calculated charge stability diagram we explain at a qualitative level the origin of alternating diamond sizes, state dependent gate couplings and nonlinear diamond edges, which all have been observed experimentally.

Our calculations explain a large part of the reductions observed experimentally, but certainly not all. Other effects not accounted for in the present work that can reduce the addition energy even further could be (i) a geometry where the molecule is closer the metallic electrodes as compared to our idealized setup, (ii) polaron formation upon charging of the molecule, which is associated with relaxation energies on the order of ∼200−300 meV,[29] and (iii) a correlation-induced localization of the added charge near the metallic electrodes beyond what can be captured by a mean-field approach.

Acknowledgment. We would like to thank T. Bjørnholm for illuminating discussions on the chemical aspects of the problem, K. Stokbro for useful inputs on the numerical calculations, Atomistix A/S for providing numerical routines for electronic structure calculations and people involved in the FEniCS project for providing useful insight in their FEM software. Financial support from the Danish Council for Production and Technology (FTP) under Grant 26-04-0181 "Atomic scale modeling of emerging electronic devices", and the European Community's Seventh Framework Programme (FP7/2007-2013) under Grant "SINGLE" no. 213609 is acknowledged.

Supporting Information Available: Detailed descriptions of (1) our theoretical scheme, (2) semiempirical method, and (3) solution of Poisson's equation. This material is available free of charge via the Internet at http://pubs.acs.org.

References

(1) Liang, W.; Shores, M. P.; Bockrath, M.; Long, J. R.; Park, H. *Nature* **2002**, *417*, 725.
(2) Park, J.; Pasupathy, A. N.; Goldsmith, J. I.; Chang, C.; Yaish, Y.; Petta, J. R.; Rinkoski, M.; Sethna, J. P.; Abruna, H. D.; McEuen, P. L.; Ralph, D. C. *Nature* **2002**, *417*, 722.
(3) Kubatkin, S.; Danilov, A.; Hjort, M.; Cornil, J.; Brédas, J.-L.; Stuhr-Hansen, N.; Hedegård, P.; Bjørnholm, T. *Nature* **2003**, *425*, 698.
(4) Yu, L. H.; Keane, Z. K.; Ciszek, J. W.; Cheng, L.; Tour, J. M.; Baruah, T.; Pederson, M. R.; Natelson, D. *Phys. Rev. Lett.* **2005**, *95*, 256803.
(5) Osorio, E. A.; O'Neill, K.; Stuhr-Hansen, N.; Nielsen, O. F.; Bjørnholm, T.; van der Zant, H. S. J. *Adv. Mater.* **2007**, *19*, 281.
(6) Osorio, E. A.; O'Neill, K.; Wegewijs, M.; Stuhr-Hansen, N.; Paaske, J.; Bjørnholm, T.; van der Zant, H. S. J. *Nano. Lett.* **2007**, *7*, 3336.
(7) Chae, D.-H.; Berry, J. F.; Jung, S.; Cotton, F. A.; Murillo, C. A.; Yao, Z. *Nano. Lett.* **2006**, *6*, 165.
(8) Danilov, A.; Kubatkin, S.; Kafanov, S.; Hedegård, P.; Stuhr-Hansen, N.; Moth-Poulsen, K.; Bjørnholm, T. *Nano. Lett.* **2008**, *8*, 1.
(9) Ahn, C. H.; Bhattacharya, A.; Ventra, M. D.; Eckstein, J. N.; Frisbie, C. D.; Gershenson, M. E.; Goldman, A. M.; Inoue, I. H.; Mannhart, J.; Millis, A. J.; Morpurgo, A. F.; Natelson, D.; Triscone, J.-M. *Rev. Mod. Phys.* **2006**, *78*, 1185.
(10) Thijssen, J. M.; van der Zant, H. S. J. *Phys. Status Solidi B* **2008**, *245*, 1455.
(11) Ward, D. R.; Halas, N. J.; Ciszek, J. W.; Tour, J. M.; Wu, Y.; Nordlander, P.; Natelson, D. *Nano. Lett.* **2008**, *8*, 919.
(12) Inkson, J. C. *J. Phys. C* **1973**, *6*, 1350.

(13) Charlesworth, J. P. A.; Godby, R. W.; Needs, R. J. *Phys. Rev. Lett.* **1993**, *70*, 1685.
(14) Hesper, R.; Tjeng, L. H.; Sawatzky, G. A. *Europhys. Lett.* **1997**, *40*, 177.
(15) Tsiper, E. V.; Soos, Z. G.; Gao, W.; Kahn, A. *Chem. Phys. Lett.* **2002**, *360*, 47.
(16) Veenstra, S. C.; Jonkman, H. T. *J. Polym. Sci., Part B: Polym. Phys.* **2003**, *41*, 2549.
(17) Zhu, X.-Y. *J. Phys. Chem. B* **2004**, *108*, 8778.
(18) Lu, X.; Grobis, M.; Khoo, K. H.; Louie, S. G.; Crommie, M. F. *Phys. Rev. B* **2004**, *70*, 115418.
(19) Repp, J.; Meyer, G.; Stojković, S. M.; Gourdon, A.; Joachim, C. *Phys. Rev. Lett.* **2005**, *94*, 026803.
(20) Marcus, R. A. *J. Chem. Phys.* **1965**, *43*, 679.
(21) Hedegård, P.; Bjørnholm, T. *Chem. Phys.* **2005**, *319*, 350.
(22) Neaton, J. B.; Hybertsen, M. S.; Louie, S. G. *Phys. Rev. Lett.* **2006**, *97*, 216405.
(23) Yeganeh, S.; Galperin, M.; Ratner, M. A. *J. Am. Chem. Soc.* **2007**, *129*, 13313.
(24) Quek, S. Y.; Venkataraman, L.; Choi, H. J.; Louie, S. G.; Hybertsen, M. S.; Neaton, J. B. *Nano. Lett.* **2007**, *7*, 3477.
(25) Mowbray, D. J.; Jones, G.; Thygesen, K. S. *J. Chem. Phys.* **2008**, *128*, 111103.
(26) Lam, S. C.; Needs, R. J. *J. Phys.: Condens. Matter* **1993**, *5*, 2101.
(27) Chulkov, E. V.; Silkin, V. M.; Echenique, P. M. *Surf. Sci.* **1999**, *437*, 330.
(28) Kouwenhoven, L. P.; Austing, D. G.; Tarucha, S. *Rep. Prog. Phys.* **2001**, *64*, 701.
(29) Geskin, V. M.; Cornil, J.; Brédas, J. L. *Chem. Phys. Lett.* **2005**, *403*, 228.

NL8021708

Paper II

Fully selfconsistent GW calculations for semi-empirical models and comparison to exact diagonalization

K. Kaasbjerg[1] and K. S. Thygesen[2]
[1] *Nano-Science Center, Niels Bohr Institute, University of Copenhagen Universitetsparken 5, DK-2100 Copenhagen, Denmark*
[2] *Center for Atomic-scale Materials Design (CAMD), Department of Physics, Technical University of Denmark, DK - 2800 Kgs. Lyngby, Denmark*
(Dated: October 9, 2009)

We calculate groundstate and single-particle excitation energies of seven pi conjugated molecules described with the semi-empirical Pariser-Parr-Pople (PPP) model using fully self-consistent many-body perturbation theory at the GW level and exact diagonalization. For the total energies, GW captures around 65% of the groundstate correlation energy while the lowest lying excitations, i.e. the electron affinity and ionization potentials, are slightly underestimated with a mean absolute error of 0.15 eV corresponding to 2.5%. We find that the effect of the GW self-energy on the molecular excitation energies is similar to inclusion of orbital relaxations that follows by changing the number of electrons in Hartree-Fock theory. Finally, we discuss the break down of the GW approximation in systems with short range interactions (Hubbard models) where correlation effects domainate over screening/relaxation effects.

PACS numbers: 31.15.bu,33.15.Ry,31.15.V-

I. INTRODUCTION

For more than two decades the many-body GW approximation of Hedin[1] has been the state of the art for calculating band structures of metals, semiconductors, and insulators[2–5]. With the entry of nanoscience the use of the GW method has been extended to low-dimensional systems such as molecules, carbon nanotubes, graphene and molecule-surface interfaces[6–12]. In these systems the interplay between quantum confinement (in one or more dimensions) and electronic correlation effects leads to novel phenomena like the renormalization of molecular electronic levels at surfaces by dynamical polarization in the substrate[11–14]. Very recently, the non-equilibrium version of the GW approximation has been applied to quantum transport and dynamics in molecular junctions[15–22] where dynamic correlations seems to be particularly important.

As the range of systems to which the GW approximation is being applied continues to expand, critical investigations of the performance of GW for other systems than the crystalline solids become important. Here we report on benchmark GW calculations for π-conjugated molecules based on the semi-empirical Pariser-Parr-Pople (PPP) model[23–25]. By comparing with exact results we obtain a direct and unbiased estimate of the quality of the GW approximation in molecular systems.

Previous benchmark model studies of the GW approximation have all focused on Hubbard models with local interactions[21,26–28] with the conclusion that GW works well for small interaction strengths but fails for larger interactions strength. The use of GW in systems with local interactions is in fact unfortunate because the importance of electronic screening, which is the main effect described by GW, is weak in comparison to correlation effects. In contrast to Hubbard models, the PPP description includes long range interactions and its parameters have been fitted to yield realistic excitation energies of conjugated molecules. It therefore provides a better and more natural starting point for a study addressing the accuracy of GW for real molecules and nanostructures. We mention that in a related work we have performed first-principles GW calculations for a series of 33 molecules arriving at very similar conclusions regarding the performance of GW as those reported here.[29]

Ab-initio GW calculations typically involve a number of "technical" approximations such as the plasmon pole approximation, the neglect of off-diagonal matrix elements in the GW self-energy, or analytic continuations. Moreover they are usually performed non-selfconsistently and are subject to basis set errors. In the present work the GW calculations are carried out fully self-consistently without any further approximations apart from the GW approximation itself.

We shall be interested in the total energies and excitation spectra of the seven conjugated molecules listed in Tab. I. The excitation spectrum of a system can be obtained from the spectral function

$$A_i(\varepsilon) = 2\pi \sum_n \Big[|\langle \Psi_n(N+1)|c_i^\dagger|\Psi_0(N)\rangle|^2 \delta(\varepsilon-\varepsilon_n) + |\langle \Psi_n(N-1)|c_i|\Psi_0(N)\rangle|^2 \delta(\varepsilon-\varepsilon_n)\Big], \quad (1)$$

which has peaks at the quasiparticle (QP) energies $\varepsilon_n = E_n(N+1) - E_0(N)$ and $\varepsilon_n = E_0(N) - E_n(N-1)$ corresponding to electronic addition and removal energies, respectively. Here $E_n(N)$ denotes the energy of the nth excited N-electron state, $|\Psi_n(N)\rangle$, with N referring to the neutral state of the system. For molecules the first addition and the first removal energy, i.e. $n = 0$, cor-

responds to the electron affinity and the ionization potential. In Hartree-Fock theory Koopman's theorem[30] states that the eigenvalues of the Hartree-Fock Hamiltonian equal the addition/removal energies calculated without orbital relaxations in the charged states, i.e. $\varepsilon_n^{\rm HF} = \langle c_n^\dagger \Psi_0^{\rm HF}(N)|H|c_n^\dagger \Psi_0^{\rm HF}(N)\rangle - E_0^{\rm HF}(N)$ for a virtual orbital n. In particular, the highest occupied molecular orbital (HOMO) and the lowest unoccupied orbital (LUMO) represent well defined approximations to the ionization potential and electron affinities, respectively[42]. This approximation neglects two important effects. One is the relaxation of the single-particle HF orbitals when an electron is removed from or added to the molecule. The other is the correlation energy which by definition is omitted in HF theory. It is instructive to write the exact QP energies as the sum of the three contributions

$$\varepsilon_n = \varepsilon_n^{\rm HF} + \Delta_{\rm relax} + \Delta_{\rm corr}, \tag{2}$$

The relaxation contribution is the correction that follows by calculating the QP energy from self-consistently determined HF energies of the neutral *and* the charged states $N \pm 1$. The last term $\Delta_{\rm corr}$ is the remaining contribution from the correlation energy. For the addition of an electron, i.e. an unoccupied orbital, the relaxation and correlation contributions are given by

$$\Delta_{\rm relax} = E_n^{\rm HF}(N+1) - E_0^{\rm HF}(N) - \varepsilon_n^{\rm HF} \tag{3}$$

and

$$\Delta_{\rm corr} = [E_n(N+1) - E_n^{\rm HF}(N+1)] - [E_0(N) - E_0^{\rm HF}(N)]. \tag{4}$$

In extended systems the potential due to a single delocalized electron/hole decreases with the size of the system. Hence, in such systems there will be no or little relaxation of the states due to the addition/removal of an electron, and the majority of the correction to the QP energy will come from the correlation part $\Delta_{\rm corr}$. In molecules, nanostructures, molecules at surfaces, and disordered systems with finite localization lengths, this is not the case. Here, the introduction of an additional electron or hole will lead to a relaxation of the single-particle orbitals corresponding to a screening of the additional charge. As a consequence, the relaxation correction $\Delta_{\rm relax}$ to the QP energy cannot be neglected in such systems. In fact, we find that $\Delta_{\rm relax}$ is larger than $\Delta_{\rm corr}$ for all the molecules studied here, and that the GW excitation energies correspond roughly to including only $\Delta_{\rm relax}$ in Eq. (2).

The paper is outlined as follows. In Sec. II the PPP model Hamiltonian for conjugated molecules is introduced. In Secs. III A and III B we provide an overview of the theory and numerical implementation of the GW and exact calculations, and in Sec. III C we discuss the use of the von Neumann entropy as a measure of correlation. The results for total energies and spectral properties of the PPP model are presented in Secs. IV A and IV B, and a comparison is made to short ranged Hubbard models in Sec. IV C. The conclusions are given in Sec. V.

II. PARISER-PARR-POPLE HAMILTONIAN

The Pariser-Parr-Pople model is an effective π-electron description of conjugated molecules that includes electron-electron interactions explicitly. The PPP Hamiltonian is given by

$$H = \sum_i \varepsilon_i \hat{n}_i - \sum_{\langle ij\rangle\sigma} t_{ij} c_{i\sigma}^\dagger c_{j\sigma} + \frac{1}{2}\sum_{i\neq j} V_{ij}(\hat{n}_i - Z_i)(\hat{n}_j - Z_j) + \sum_i U_i \hat{n}_{i\uparrow}\hat{n}_{i\downarrow}, \tag{5}$$

where $c_i^\dagger$ (c_i) creates (annihilates) an electron in the p_z orbital on atom i of the molecule, $\hat{n}_i = \hat{n}_{i\uparrow} + \hat{n}_{i\downarrow}$ is the number operator, $\hat{n}_{i\sigma} = c_{i\sigma}^\dagger c_{i\sigma}$, Z_i is the valence (i.e. the number of π electrons) of atom i, and $\langle ij\rangle$ denotes nearest neighbour hopping. The Ohno parametrization[31] is used for the long range interactions

$$V_{ij} = \frac{14.397}{\sqrt{(28.794/(U_i+U_j))^2 + R_{ij}^2}}\,, \tag{6}$$

where R_{ij} is the inter-atomic distance (in Å) and U_i is the onsite Coulomb interaction (in eV). For large distances the Ohno parametrization recovers the $1/r$ behavior of the Coulomb interaction while it for small distances represents a screened interaction that interpolates to onsite Coulomb interaction U_i for $R_{ij} = 0$. The onsite energy ε_i, the hopping element t_{ij} and the onsite Coulomb interaction U_i are treated as fitting parameters. In the present work values for these parameters have been taken from the literature[32–36]. Since existing parameters have been optimized to optical excitation spectra, an exact agreement with experimental values for the molecular gaps is not to be expected.

III. METHODS

A. GW approximation

Hedin's equations[1] provides a formally exact framework for the determination of the single-particle Green function in a self-consistent manner. In the GW approximation, which follows by neglecting the so called vertex corrections, the electronic self-energy Σ is given by the product of the Green function G and the screened interaction W, and can be written symbolically as

$$\Sigma = iGW, \tag{7}$$

where the Green function obeys the usual Dyson equation $G = G_0 + G_0\Sigma G$. The screened interaction W is given by the bare Coulomb interaction V and the polarization in the random-phase approximation (RPA) $P = -iGG$ through the Dyson-like equation

$$W = V + VPW. \tag{8}$$

In fully self-consistent GW the set of coupled equations for Σ, G, P, and W are solved iteratively until the Green function has converged. Due to the computational requirement of a fully self-consistent GW scheme, *ab-initio* GW calculations are usually carried out non-selfconsistently. This approach, which is referred to as G_0W_0, starts from an approximate G_0, typically the non-interacting Kohn-Sham Green function, from which a single self-energy iteration is carried out to obtain the final Green function.

1. Numerical details

The GW calculations have been performed following the method described in detail in Ref. 37. Here we give a brief overview of the method for completeness.

The retarded and advanced single-particle Green functions are given by

$$G^{r/a}(\varepsilon) = (\varepsilon \pm i\eta - H_0 - V_{\rm H} - \Sigma_{GW}(\varepsilon))^{-1} \quad (9)$$

where η is a small positive infinitesimal, H_0 contains the first two terms in Eq. (5), and $V_{\rm H}$ is the Hartree potential. We represent the Green functions and all other energy-dependent quantities on a uniform grid, $-E_m, -E_m + d\varepsilon, \ldots, E_m$. The Fast Fourier Transform is used to switch between the energy and time representations. Since η determines the minimum width of features in the Green function's energy dependence, the energy grid spacing should obey $d\varepsilon \ll \eta$. All results presented here have been converged with respect to $\eta, d\varepsilon, E_m$. Typical converged values are (in eV) $\eta = 0.02, d\varepsilon = 0.005, E_m = 50$.

The lesser/greater Green functions are given by

$$G^{<}(\varepsilon) = -f(\varepsilon-\mu)[G^r - G^a] \quad (10)$$
$$G^{>}(\varepsilon) = (1-f(\varepsilon-\mu))[G^r - G^a] \quad (11)$$

where $f(\varepsilon-\mu)$ is the Fermi-Dirac function. The chemical potential μ is adjusted to yield the desired number of electrons in the system. The formulation in terms of a fixed chemical potential rather than a fixed particle number is reminiscent of the fact that the method has been developed for quantum transport. The one-body density matrix is given by

$$\rho_{ij} = -i\int G^{<}_{ij}(\varepsilon)d\varepsilon. \quad (12)$$

From ρ the Hartree and exchange potentials follow

$$V_{{\rm H},ij} = 2\sum_k V_{ik}\rho_{kk}) \quad (13)$$
$$V_{x,ij} = -V_{ij}\rho_{ij}, \quad (14)$$

where we have defined $V_{ii} = U_i$, see Eq. (5).

The retarded/advanced and lesser/greater components of the quantities needed to construct the GW self-energy read[37]

$$\Sigma^{</>}_{{\rm GW},ij}(t) = iG^{</>}_{ij}(t)W^{</>}_{ij}(t) \quad (15)$$
$$W^{</>}_{ij}(\varepsilon) = \sum_{kl} W^r_{ik}(\varepsilon)P^{</>}_{kl}(\varepsilon)W^a_{lj}(\varepsilon) \quad (16)$$
$$W^{r/a}_{ij}(\varepsilon) = \sum_k P^{r/a}_{ik}[1 - VP^{r/a}(\varepsilon)]^{-1}_{kj} \quad (17)$$
$$P^{</>}_{ij}(t) = G^{</>}_{ij}(t)G^{>/<}_{ji}(-t) \quad (18)$$

The GW equations have been expressed in the time or energy domain according to where they are simplest. This also reflects the practical implementation.

The retarded components of $\Sigma_{\rm GW}$ and P are obtained using the fundamental relation

$$F^r(t) = -i\theta(t)[F^{>}(t) - F^{<}(t)] \quad (19)$$

which is the Kramers-Kronig relation in the time domain relating the imaginary and real parts of F^r.

Since the GW self-energy depends on the Green function and vice versa, the equations must be iterated until self-consistency. To speed up converence we use the Pulay mixing scheme[38] as described in Ref. 37.

2. Total energy

The total energy can be split into kinetic (and external), Hartree, and exchange-correlation energy $E = E_0 + E_{\rm H} + E_{\rm xc}$. In terms of the Green function we have

$$E_0 + E_{\rm H} = {\rm Tr}[H_0\rho] + \frac{1}{2}{\rm Tr}[V_{\rm H}\rho] \quad (20)$$

For the exchange-correlation energy we have

$$E_{\rm xc} = \frac{1}{2i}\int {\rm Tr}[\Sigma^r(\varepsilon)G^{<}(\varepsilon) + \Sigma^{<}(\varepsilon)G^a(\varepsilon)]d\varepsilon, \quad (21)$$

where Σ is the exchange-correlation self-energy. In this work Σ is either the bare exchange, Σ_x, yielding the HF approximation, or the GW self-energy, $\Sigma_{\rm GW}$. The expression (21) follows by expressing $\langle\hat{V}\rangle$ in terms of the two-particle Green function, G_2, and then using the defining equation for the self-energy in terms of G_2[39].

B. Exact diagonalization

The most direct way to the spectral properties of a system is via the Lehmann representation of the Green function in Eq. (1). However, since this requires the full set of eigenstates and eigenvalues of the Hamiltonian, it is of limited practical use and other routes must be taken. The following section gives a brief overview of the Lanczos method for iterative diagonalization of large matrices.

1. Calculating the ground state - Lanczos algorithm

In exact diagonalization the given many-body Hamiltonian is diagonalized directly in the Fock space which is spanned by many-particle states (Slater determinants). Since the dimensionality of the Fock space grows exponentially with the number of basis orbitals, symmetries of the Hamiltonian can help to reduce the dimensionality considerably. For the Pariser-Parr-Pople Hamiltonian in Eq. (5) the number of up and down electrons, $N_\uparrow$ and $N_\downarrow$, are good quantum numbers since their corresponding operators commute with the Hamiltonian. This implies that the exact diagonalization can be carried out in each of the $(N_\uparrow, N_\downarrow)$-subblocks of the Fock space independently. The dimensionality of each $(N_\uparrow, N_\downarrow)$-subblock is given by the number of ways $N_\uparrow$ spin up electrons and $N_\downarrow$ spin down electrons can be distributed over L basis orbitals,

$$d(N_\uparrow, N_\downarrow) = \frac{L!}{N_\uparrow!(L-N_\uparrow)!} \times \frac{L!}{N_\downarrow!(L-N_\downarrow)!}. \qquad (22)$$

Very often the ground state is located in the half-filled subblock, i.e. $N_\uparrow = N_\downarrow = L/2$ where L is the number of basis orbitals. For $L = 16$ the dimensionality of this subblock is $d = 165636900$, implying that storing a vector in double floating point precision requires ~ 1 Gb of memory. With such memory requirements a full diagonalization of the Hamiltonian is of course out of reach. If only the ground state is needed, iterative methods can be employed. The basic idea of iterative methods is to project the Hamiltonian onto the Krylov subspace $\mathcal{K}$ generated by repeated applications of H on an arbitrary initial state $|\phi_0\rangle$, i.e.

$$\mathcal{K} = \mathrm{span}\{|\phi_0\rangle, H|\phi_0\rangle, H^2|\phi_0\rangle, \cdots, H^N|\phi_0\rangle\}. \qquad (23)$$

In the Krylov subspace the extreme eigenvalues of the Hamiltonian converge fast with respect to the size N of the subspace, thus reducing the full diagonalization to a manageable diagonalization of a $N \times N$ matrix, with $N \ll d$.

In the Lanczos algorithm[43] the Hamiltonian is projected onto a specially constructed orthogonalised Krylov basis in which the Hamiltonian has a tridiagonal representation. The basis vectors are generated recursively as

$$|\phi_{n+1}\rangle = H|\phi_n\rangle - a_n|\phi_n\rangle - b_n^2|\phi_{n-1}\rangle, \qquad (24)$$

where the coefficient are given by

$$a_n = \frac{\langle\phi_n|H|\phi_n\rangle}{\langle\phi_n|\phi_n\rangle} \quad \text{and} \quad b_n^2 = \frac{\langle\phi_n|\phi_n\rangle}{\langle\phi_{n-1}|\phi_{n-1}\rangle} \qquad (25)$$

with initial conditions $b_0 = 0$ and $|\phi_{-1}\rangle = 0$. At any point during the Lanczos iterations only three Lanczos vectors needs to be kept in memory, which makes the algorithm memory efficient. In the basis of the normalized vectors (the basis vectors above are not normalized) the Hamiltonian has the following tridiagonal representation

$$H = \begin{pmatrix} a_0 & b_1 & 0 & \cdots & 0 \\ b_1 & a_1 & b_2 & & \vdots \\ 0 & b_2 & a_2 & \ddots & 0 \\ \vdots & & \ddots & \ddots & b_N \\ 0 & \cdots & 0 & b_N & a_N \end{pmatrix} \qquad (26)$$

which can be readily diagonalized with methods for tridiagonal matrices. In practice the Lanczos iterations are continued until the desired eigenvalues have converged to a given tolerance. For the ground state energy E_0, typical values for N range from a few to ~ 200 depending on the system size.

The ground state resulting from a diagonalization of the tridiagonal Hamiltonian in Eq. (26) is provided in the Lanczos basis, i.e. $|\Psi_0\rangle = \sum_n c_n|\phi_n\rangle$. In order to be able to calculate the Green function, its representation in the original many-body basis is required. Since the Lanczos vectors are not stored, the Lanczos iterations must be repeated (starting from the same initial vector) to obtain the expansion coefficients $\alpha_i = \sum_n c_n\langle\Phi_i|\phi_n\rangle$ in the original many-body basis $\{|\Phi_i\rangle\}_{i=1}^d$.

The most time consuming part of the Lanczos algorithm is the matrix-vector multiplication $H|\phi_n\rangle$. An efficient implementation of this part is hence crucial. For this purpose it is convenient to use the bit representation of an unsigned integer to code the basis states. Denoting the integers with bit representations corresponding to the spin up and spin down occupations of a given basis state with $I_\uparrow$ and $I_\downarrow$, respectively, the integer representation of the basis state is $I = I_\uparrow + 2^L I_\downarrow$. With the binary representation of the basis states, the multiplication of the Hamiltonian can be done efficiently using bitwise operations.

2. Calculating the Green function

Having obtained the ground state, the Green function can now be calculated. From the Lehmann representation it follows that it can be written as

$$G_{ij}^r(\varepsilon) = G_{ij}^e(\varepsilon) + G_{ij}^h(\varepsilon) \qquad (27)$$

with the electron and hole Green functions defined by

$$G_{ij}^e(\varepsilon) = \langle\Psi_0^N|c_i \frac{1}{\varepsilon - H + E_0^N + i\eta} c_j^\dagger|\Psi_0^N\rangle \qquad (28)$$

and

$$G_{ij}^h(\varepsilon) = \langle\Psi_0^N|c_j^\dagger \frac{1}{\varepsilon + H - E_0^N + i\eta} c_i|\Psi_0^N\rangle, \qquad (29)$$

respectively. In the following we focus on the electron Green function which is the matrix representation of the

resolvent operator $(z-H)^{-1}$ in the basis spanned by the $|i\rangle = c_i^\dagger|\Psi_0^N\rangle$ vectors. To obtain the i'th diagonal element,

$$G^e_{ii}(\varepsilon) = \langle i|(z-H)^{-1}|i\rangle, \tag{30}$$

where $z = \varepsilon + E_0^N + i\eta$, again the Lanczos algorithm is used to put H on a tridiagonal form, but this time the Lanczos iterations are started from the normalized initial state $|\phi_0\rangle = |i\rangle/b_0$ where $b_0^2 = \langle i|i\rangle$. Hence, in the generated Krylov subspace the diagonal element in Eq. (30) corresponds to the matrix element $b_0^2[(\varepsilon - H + E_0^N + i\eta)^{-1}]_{11}$ of a tridiagonal matrix, which can be obtained as the continued fraction[40]

$$G^e_{ii}(\varepsilon) = \cfrac{b_0^2}{\varepsilon - a_0 - \cfrac{b_1^2}{\varepsilon - a_1 - \cfrac{b_2^2}{\varepsilon - a_2 - \cdots}}}. \tag{31}$$

Again the Lanczos iterations are continued until the frequency dependent Green function element has converged.

C. Von Neumann entropy

The following section demonstrates how a quantitative measure of the degree of correlations in a system can be obtained by considering the von Neumann entropy of the reduced single-particle density matrix ρ. The entropy is defined by

$$S[\rho] = -\mathrm{Tr}[\rho\log\rho] = -\sum_n \rho_n \log\rho_n, \tag{32}$$

where in the last equality ρ has been expressed in its diagonal representation, $\rho = \sum_n \rho_n |n\rangle\langle n|$.

In the basis of the atomic p_z orbitals the matrix elements of the reduced density matrix are given by (with the spin index suppressed)

$$\rho_{ij} = \langle\Psi_0|c_j^\dagger c_i|\Psi_0\rangle, \tag{33}$$

with the diagonal elements equal to the site occupations. In the diagonal representation ρ_n thus represents the occupation of the eigenstate $|n\rangle$ of the density matrix.

We note that $0 \le S \le L\log 2$, where $2L$ is the dimension of the single-particle Hilbert space including spin. The expression for $S_{\max}$ follows because the number of electrons equal L in all the systems, i.e. half filled "band". When $|\Psi_0\rangle$ is a single Slater determinant (corresponding to zero correlation) we have $S = 0$, and when $|\Psi_0\rangle$ has equal weight on a complete set of orthogonal Slater determiants (corresponding to maximal correlation) we have $\rho_n = 1/2$ for all n and thus $S = L\log 2$. Thus the number $0 \le S/S_{\max} \le 1$ represents a natural measure of the degree of correlation in $|\Psi_0\rangle$.

IV. RESULTS

A. Total energies

We first address the degree of correlation in the exact ground states by considering the von Neumann entropies of the corresponding density matrices. The calculated entropies are listed in Tab. I. Except for the Hubbard description of benzene (see Sec. IV C) which clearly presents strong correlations, the entropies of the ground states are $\sim 10\%$ of their maximum value $S_{\max}$ corresponding to weakly correlated systems. The finite values of the entropies reveal that none of the ground states are single Slater determinants implying that the Hartree-Fock ground state energies will be larger than the exact ones.

We here follow the usual convention and define the correlation energy as the part of the total energy not included in Hartree-Fock, i.e.

$$E_{\mathrm{corr}} = E_{\mathrm{exact}} - E_{\mathrm{HF}}. \tag{34}$$

Fig. 1 shows the exact correlation energies of the neutral molecules together with those obtained by evaluating the total energy from Eqs. (20) and (21) with the self-consistently determined Green function and GW self-energy.

For the series of molecules considered here the correlation energy constitute less than 0.5% of the total energies. Furthermore, as expected it decreases (in absolute size) with the number of atoms in the molecule. Clearly, the GW approximation performs reasonably well for all the molecules capturing on average 66% of the correlation energy.

B. Spectral properties

For isolated systems such as molecules, true quasiparticles resembling single-particle excitations are char-

	Formula	L	$S/S_{\max}$	E_{gap} (eV)
thiophene	C_4H_4S	5	0.07	11.19
pyridine	C_5H_5N	6	0.11	10.61
benzene	C_6H_6	6	0.10	11.39
benzene (Hubbard)	-	-	0.50	-
biphenyl	$C_{12}H_{10}$	12	0.10	9.24
naphthalene	$C_{10}H_8$	10	0.11	8.65
anthracene	$C_{14}H_{10}$	14	0.12	7.06
OPV2	$C_{14}H_{12}$	14	0.10	8.30

TABLE I: Chemical formula, number of p_z orbitals (L) included in the PPP model and exact ground state entropies (S) for the listed molecules.

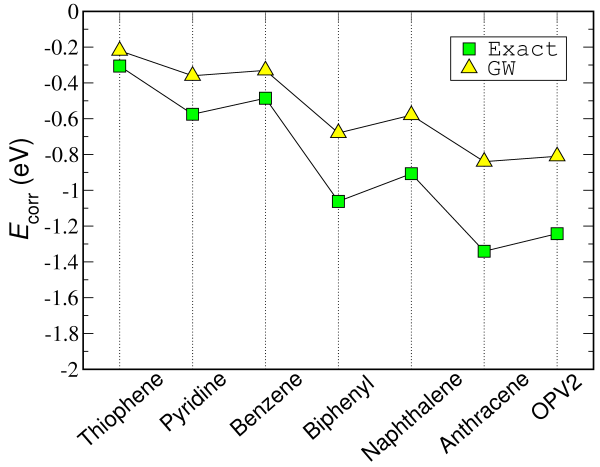

FIG. 1: (Color online) Exact and GW correlation energies of the neutral groundstate of the seven molecules.

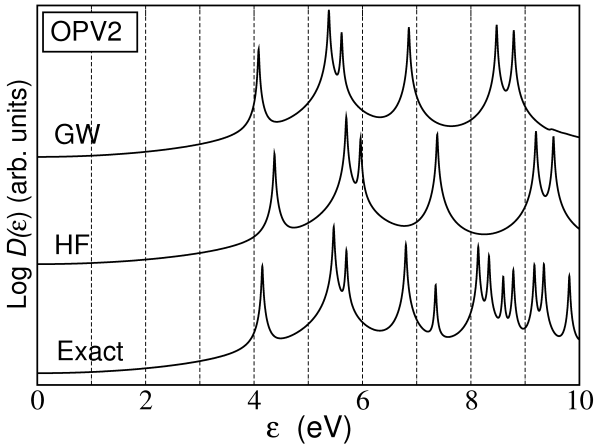

FIG. 2: (Color online) Single-particle DOS of the OPV2 molecule. Note the logarithmic axis.

acterized by having a weight close to unity (for non-degenerate levels) in the spectral function, i.e.

$$Z_n = \sum_i |\langle \Psi_n^{N+1} | c_i^\dagger | \Psi_0^N \rangle|^2 \sim 1. \tag{35}$$

This is equivalent to saying that there exists an orbital $|\nu\rangle$ so that the excited state $\langle \Psi_n^{N+1}|$ can be written as the single-particle excitation $c_\nu^\dagger |\Psi_0^N\rangle$. In Fig. 2 we show the single-particle density of states (DOS),

$$D(\varepsilon) = \sum_i A_i(\varepsilon) \tag{36}$$

for the OPV2 molecule on a logarithmic scale. The height of the peaks reflects the value of Z_n (modulo degeneracies). The HF and, in particular, the GW approximation reproduce the lowest lying excitations quite well while higher excitations are poorly described. All the peaks in the HF spectrum have $Z_n = 1$ while GW does shift some spectral weight from the main peaks to tiny satelite structures (at higher energies than shown on the plot). However, the GW satelites do not correspond to features in the exact spectrum. This shows that excitations with $Z_n \ll 1$, i.e. excitations which do not have single-particle character, are not well described by GW whose main effect is to improve the position of the HF single-particle peaks.

In the following we consider the lowest lying single-particle excitations of the molecules as obtained with Hartree-Fock, G_0W_0 and self-consistent GW. In the G_0W_0 calculations the starting Green function G_0 is taken to be the self-consistently determined Hartree-Fock Green function. Fig. 4 gives an overview of the calculated excitation energies relative to the exact ones. Energies corresponding to electron removal and electron addition are located on the negative and positive half of the x-axis, respectively. From this plot clear trends in the calculated excitation energies emerge.

Starting with HF, the occupied (unoccupied) levels are systematically overestimated (underestimated). The deviation from the exact values worsens for the higher lying excitations.

A close inspection of the figure reveals a few HF energies at $\sim \pm 5.0$ eV and $\sim \pm 5.7$ eV that more or less coincide with the exact energies. These are the HOMO and LUMO levels of the small single-ring molecules thiophene, pyridine and benzene. The good agreement with the exact levels for these systems is not a result of HF giving a correct description of the many-body states and their energies – this was already clear from the analysis above which showed that the eigenstates are not single Slater determinants and hence the excitation energies in Eq. (2) have contributions from both $\Delta_{\rm relax}$ and $\Delta_{\rm corr}$. The good agreement must therefore be ascribed to cancellations between the relaxation and correlation contribution to the exact energies (this is discussed further in connection with Fig. 4).

Both the G_0W_0 and the GW give consistently better energies than HF – in particular for the higher lying excitations where the absolute errors are reduced to less than $\sim$0.4 eV as compared to $\sim$1 eV for HF. For the low-lying excitations GW slightly overestimates (underestimates) the occupied (unoccupied) levels corresponding to an overcorrection of the HF energies.

In order to address the relative contributions from $\Delta_{\rm relax}$ and $\Delta_{\rm corr}$ to the excitation energies in Eq. (2), we plot in Fig. 4 the difference between the exact gaps and the gaps obtained from the (i) Hartree-Fock eigenvalues, (ii) Hartree-Fock total energy differences *with* self-consistent relaxations in the $N \pm 1$ Slater determinants taken into account, and (iii) the distance between the highest occupied and lowest unoccupied peaks in the GW spectral function. By using the expression for the quasi-particle energies in Eq. (2), the exact gap

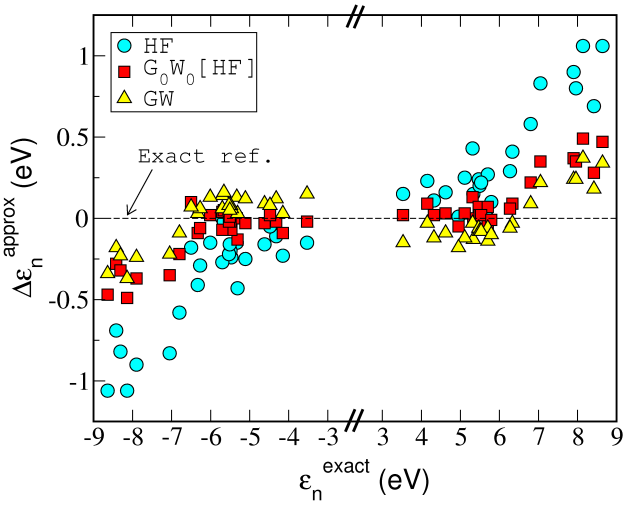

FIG. 3: (Color online) Energy of the 3 highest occupied and 3 lowest unoccupied molecular orbitals relative to the exact values. While Hartree-Fock underestimates the occupied and overestimates the unoccupied levels, self-consistent GW shows the opposite trends but deviates on average less from the exact result.

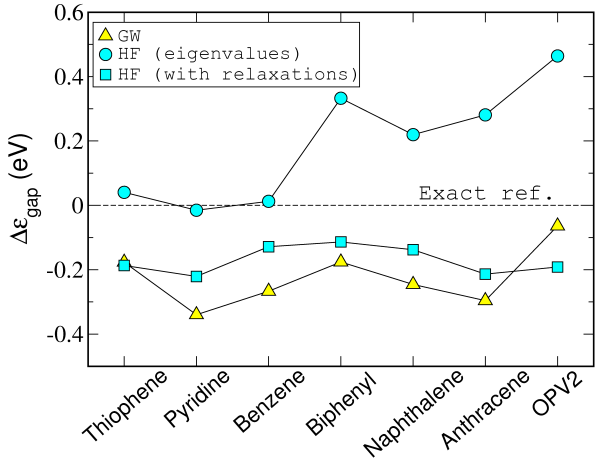

FIG. 4: (Color online) The HOMO-LUMO gap relative to the exact values. In addition to the HF and GW single-particle energies, the relaxed Hartree-Fock total energy differences, $E_0^{\rm HF}(N+1)+E_0^{\rm HF}(N-1)-2E_0^{\rm HF}(N)$ are also shown. The excellent results of HF for the three smallest molecules is a result of error cancellation between relaxation and correlation contributions.

$E_{\rm gap}=\varepsilon_{\rm LUMO}-\varepsilon_{\rm HOMO}$ can be expressed as

$$E_{\rm gap}=\varepsilon^{\rm HF}_{\rm LUMO}-\varepsilon^{\rm HF}_{\rm HOMO}+\Delta^{\rm gap}_{\rm relax}+\Delta^{\rm gap}_{\rm corr} \qquad (37)$$

where $\Delta^{\rm gap}_{\rm relax}$ and $\Delta^{\rm gap}_{\rm corr}$ are the gap equivalents of the corresponding quantities in Eq. (2) and $\varepsilon^{\rm HF}_{\rm HOMO/LUMO}$ are the Hartree-Fock HOMO/LUMO eigenvalues. By definition $\Delta^{\rm gap}_{\rm relax}$ is difference between the gaps obtained from the HF eigenvalues and relaxed HF total energy differences. In Fig. 4 this is given by the vertical distance between the (blue) squares and circles. The correlation contribution $\Delta^{\rm gap}_{\rm corr}$ can be read off as the difference between the exact gap (dashed horizontal line) and the relaxed HF total energy gap (blue squares). Inclusion of relaxation effects clearly reduces the HF gaps considerably implying that $\Delta^{\rm gap}_{\rm relax}<0$. This reduction is due to the screening from the orbital relaxation which reduces the Coulomb interaction with the added hole or electron and hence also the gap.

We note that the HF eigenvalues give excellent gaps for the small single-ring molecules thiophene, pyridine and benzene. The good agreement with the exact levels for these systems is not a result of HF giving a correct description of the many-body states and their energies – this was already clear from the analysis above which showed that the eigenstates are not single Slater determinants and hence the excitation energies in Eq. (2) have contributions from both $\Delta_{\rm relax}$ and $\Delta_{\rm corr}$. The good agreement must therefore be ascribed to cancellations between the relaxation and correlation contribution to the exact energies

In contrast to the HF (eigenvalue) gaps for which the agreement with the exact gap worsens as a function of the size of the molecules, the GW gaps follow more consistently the same trend and underestimates the exact gaps with $0.05-0.35$ eV for all the molecules. The close resemblance between GW and the relaxed HF result indicates that the effect of GW is mainly to account for the screening effects included in HF via orbital relaxations, $\Delta_{\rm relax}$.

C. Long- versus short-range interactions

To demonstrate the shortcomings of the GW approximation for strongly correlated systems, we consider a Hubbard model description of the benzene molecule. It should be noted that this Hubbard description of benzene is not intended as a realistic description of the benzene molecule, rather it serves to illustrate the limitations of the GW approximation. The Hamiltonian is identical to the PPP-Hamiltonian in Eq. (5), except that the long range Coulomb interactions in the third term have been omitted. The values for the hopping elements and the onsite Coulomb interaction are $t=2.539$ and $U=10.06$, respectively. With a U/t-ratio of $\sim$4 this obviously represent a strongly correlated system. The latter is reflected in the ground state entropy in Tab. I which is 50% of its maximum value.

From the calculated total energies we find that the correlation energy (not included in Fig. 1) constitutes 10% of the ground state energy which is a considerably higher fraction as for the PPP descriptions of the molecules. The GW total energy captures 88% of the correlation energy compared to 66% on the average for the PPP descriptions. However, from an absolute point of view, the

GW approximation misses the exact ground state energy by 0.48 eV. This should be compared to 0.16 eV which is the difference between the exact and the GW ground state energy for the PPP description of benzene.

The poor performance of both Hartree-Fock and GW for the spectral properties of the Hubbard benzene is illustrated in Fig. 5 which shows the spectral function as calculated with the two methods together with the exact one. Both Hartree-Fock and GW severely underestimates the position of the LUMO level and completely misses the details of the spectrum at higher energies.

This clearly demonstrates that GW is of limited relevance when considering systems where correlation effects ($\Delta_{\rm corr}$) dominates over screening, or relaxation, effects ($\Delta_{\rm relax}$).

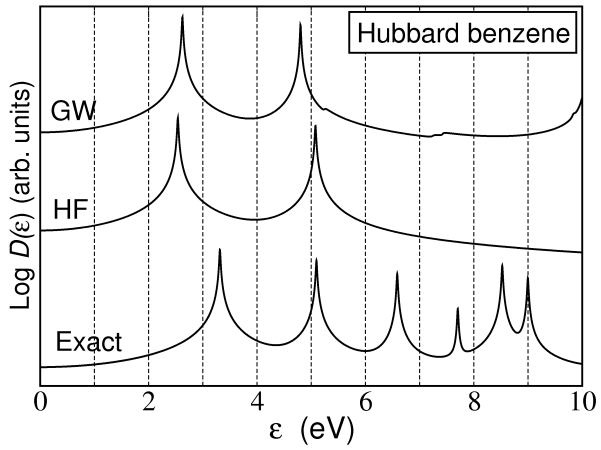

FIG. 5: (Color online) Single-particle DOS for the Hubbard description of the benzene molecule (only on-site interactions from the PPP model are kept). Note the logarithmic axis.

V. CONCLUSION

We have presented calculations for the total energy and charged single-paticle excitations in seven conjugated molecules described by the semi-empirical PPP model within fully self-consistent GW and exact diagonalization. The results show that the GW approximation gives a consistently good description of both total energies and electronic excitations with a slight tendency to overestimate (underestimate) the position of the latter for occupied (unoccupied) levels. We have found that the effect of the GW self-energy is similar to the inclusion of orbital relaxations in the $N \pm 1$ final states in Hartree-Fock theory. On the other hand the contribution to the excitation energies coming from correlations in the ground- and excited states is less well described by GW. This explains why GW tend to reduce electron addition/removal energies relative to the HF eigenvalues. Finally, we showed that GW does not perform well for systems with short range interactions (Hubbard models) where correlation effects are dominating over screening/relaxation effects.

VI. ACKNOWLEDGEMENTS

Financial support from the Danish Council for Production and Technology (FTP) under Grant 26-04-0181 "Atomic scale modeling of emerging electronic devices" is acknowledged. KST acknowledges support from the Danish Center for Scientific Computing. The Center for Atomic-scale Materials Design (CAMD) is sponsored by the Lundbeck Foundation.

[1] L. Hedin, Phys. Rev. **139**, A796 (1965).
[2] M. S. Hybertsen and S. G. Louie, Phys. Rev. B **34**, 5390 (1986).
[3] W. G. Aulbur, L. Jonsson, and J. W. Wilkins, in *Solid State Physics*, edited by H. Ehrenreich and F. Saepen (Academic Press, New York, 2000), vol. 54, p. 1.
[4] F. Aryasetiawan and O. Gunnarsson, Rep. Prog. Phys. **61**, 237 (1998).
[5] G. Onida, L. Reining, and A. Rubio, Rev. Mod. Phys. **74**, 601 (2002).
[6] J. C. Grossman, M. Rohlfing, L. Mitas, S. G. Louie, and M. L. Cohen, Phys. Rev. Lett. **86**, 472 (2001).
[7] A. Stan, N. E. Dahlen, and R. van Leeuwen, Europhys. Lett. **76**, 298 (2006).
[8] C. D. Spataru, S. Ismail-Beigi, X. L. Benedict, and S. G. Louie, Phys. Rev. Lett. **92**, 077402 (2004).
[9] P. E. Trevisanutto, C. Giorgetti, L. Reining, M. Ladisa, and V. Olevano, Phys. Rev. Lett. **101**, 226405 (2008).
[10] M. L. Tiago and J. R. Chelikowsky, Phys. Rev. B **73**, 205334 (2006).
[11] J. B. Neaton, M. S. Hybertsen, and S. G. Louie, Phys. Rev. Lett. **97**, 216405 (2006).
[12] C. Freysoldt, P. Rinke, and M. Scheffler, Phys. Rev. Lett. **103**, 056803 (2009).
[13] K. Kaasbjerg and K. Flensberg, Nano. Lett. **8**, 3809 (2008).
[14] K. S. Thygesen and A. Rubio, Phys. Rev. Lett. **102**, 046802 (2009).
[15] C. D. Spataru, L. X. Benedict, and S. G. Louie, Phys. Rev. B **69**, 205204 (2004).
[16] K. S. Thygesen and A. Rubio, J. Chem. Phys. **126**, 091101 (2007).
[17] P. Darancet, A. Ferretti, D. Mayou, and V. Olevano, Phys. Rev. B **75**, 075102 (2007).
[18] K. S. Thygesen, Phys. Rev. Lett. **100**, 166804 (2008).
[19] P. Myöhanen, A. Stan, G. Stefanucci, and R. van Leeuwen, Europhys. Lett. **84**, 67001 (2008).
[20] C. D. Spataru, M. S. Hybertsen, S. G. Louie, and A. J. Millis, Phys. Rev. B **79**, 155110 (2009).
[21] M. P. von Friesen, C. Verdozzi, and C.-O. Almbladh, arXiv:0905.2061 (2009).
[22] N. E. Dahlen and R. van Leeuwen, Phys. Rev. Lett. **98**,

153004 (2007).
[23] J. A. Pople, Trans. Faraday Soc. **49**, 1375 (1953).
[24] R. Pariser and R. G. Parr, J. Chem. Phys. **21**, 466 (1953).
[25] R. Pariser and R. G. Parr, J. Chem. Phys. **21**, 767 (1953).
[26] A. Schindlmayr, T. J. Pollehn, and R. W. Godby, Phys. Rev. B **58**, 12684 (1998).
[27] T. J. Pollehn, A. Schindlmayr, and R. W. Godby, J. Phys.: Condens. Matter **10**, 1273 (1998).
[28] C. Verdozzi, R. W. Godby, and S. Holloway, Phys. Rev. Lett. **74**, 2327 (1995).
[29] C. Rostgaard, K. W. Jacobsen, and K. S. Thygesen, submitted
[30] P. Fulde, *Electron Correlations in Molecules and Solids*, no. 100 in Springer Series in Solid-State Sciences (Springer, Berlin, 1995), 3rd ed.
[31] K. Ohno, Theor. Chim. Acc. **2**, 219 (1964).
[32] I. R. Ducasse, T. E. Miller, and Z. G. Soos, J. Chem. Phys. **76**, 4094 (1982).
[33] W. Barford and R. J. Bursill, Chem. Phys. Lett. **268**, 535 (1997).
[34] R. J. Bursill, C. Castleton, and W. Barford, Chem. Phys. Lett. **294**, 305 (1998).
[35] W. Barford, R. J. Bursill, and M. Y. Lavrentiev, J. Phys.: Condens. Matter **10**, 6429 (1998).
[36] M. Y. Lavrentiev, W. Barford, S. J. Martin, and H. Daly, Phys. Rev. B **59**, 9987 (1999).
[37] K. S. Thygesen and A. Rubio, Phys. Rev. B **77**, 115333 (2008).
[38] P. Pulay, Chem. Phys. Lett. **73**, 393 (1980).
[39] A. L. Fetter and J. D. Walecka, *Quantum theory of many-particle systems* (McGraw-Hill, New York, 1971).
[40] E. Dagotto, Rev. Mod. Phys. **66**, 763 (1994).
[41] P. Dayal, M. Troyer, and R. Villiger, *The Iterative Eigensolver Template Library (IETL)*, `http://www.comp-phys.org/software/ietl/`.
[42] In the remaining of the paper HOMO and LUMO abbreviations will be used to refer to the ionization potential and electron affinity also outside Hartree-Fock theory.
[43] The present work has used the implementation from the IETL project[41].